ABSTRACT

LIM, JIHYE. Creation of Woven Structures Impacting Self-cleaning Superoleophobicity. (Under the direction of Prof. Nancy Powell and Dr. Stephen Michielsen).

For protection of human life from harmful or toxic liquids in working areas, solid surface resistance to liquid with low surface tension (e.g. oil) should be achieved in the outermost layer of protective clothing. Based on the literature review, multiscale structures were emphasized because they can increase roughness on a solid surface and create more void spaces of different sizes. The roughness and void spaces contribute to creating a liquid-vapor interface and reducing the liquid contact area to the solid surface. Woven fabric inherently consists of multiscale structures by its construction: microscale in a yarn structure and macroscale in a fabric structure. When the solid surface tension is low relative to oil, creating an appropriate structural geometry will become a critical way to obtain a superoleophobic surface for oil-resistance.

Theoretical modeling and experiments with actual fabric samples were utilized to predict and prove the highest performing structural geometry in woven fabric, respectively. The theoretical geometric modeling accounted for the different weave structures, the yarn compression by the yarn flattening factor, e, and the void space by the void space ratio to the fiber or yarn diameter, T, impacting the liquid apparent contact angle on a fabric surface. The Cassie-Baxter equations were developed using Young's contact angle, θ_e, θ_e and e, or θ_e, e, and T, to predict the liquid apparent contact angle for different geometries. In addition, to prevent a liquid's penetration into a solid structure, the ranges of the protuberance height ($>> h_2$) and distance ($< 4\ell^2_{cap}$) were predicted by the definition of the Laplace pressure, the capillary

pressure, and the sagging phenomenon. Those predictions were in strong agreement with the results from the empirical experiment using the actual woven fabric samples. This study identified the impact of the geometries in yarn and woven fabric structures on the fabric resistance against oil through theoretical modeling and experiments. The results suggest particular weave structures, the range of the void space (or the protuberance distance) and the protuberance height in the yarn and fabric structures for the highest performing self-cleaning superoleophobic woven fabric surface.

Creation of Woven Structures Impacting Self-cleaning Superoleophobicity

by
Jihye Lim

A dissertation submitted to the Graduate Faculty of
North Carolina State University
in partial fulfillment of the
requirements for the degree of
Doctor of Philosophy

Fiber and Polymer Science

Raleigh, North Carolina

2014

APPROVED BY:

Prof. Nancy Powell (Co-Chair)	Dr. Stephen Michielsen (Co-Chair)
Dr. Martin King	Dr. Peter Bloomfield

BIOGRAPHY

Jihye Lim received her B.S. degree in Clothing and Textiles at Gyeongsang National University in South Korea, February 2004. She pursued her M.S. degree in the Textile science from the College of Clothing and Textiles at Yonsei University in South Korea from 2007 to 2009. She joined the FPS (Fiber and Polymer Science) Ph.D. program in the College of Textiles at North Carolina State University in 2011.

ACKNOWLEDGMENTS

First and foremost, I want to give thanks to God for his love and grace.

I would like to express my sincerest gratitude to my co-advisors: Prof. Nancy Powell and Dr. Stephen Michielsen. Their endless encouragement and support led me go through difficult times during pursuing my Ph.D. degree. Special thanks to Dr. Hoon Joo Lee who was my first supervisor and academic mentor, without her thoughtful guidance I would not have been able to walk on the proper path in my academic life. They always showed their trust and patience with me through my Ph.D. academic years.

I also want to thank to my committee members: Dr. Martin King and Dr. Peter Bloomfield for their valuable advising on my work. Dr. Tushar Ghosh helped me to obtain the right direction in the writing of my dissertation. I express thanks to Dr. Melissa Pasquinelli who encouraged me while working in a research group.

I extend my gratitude to all colleagues in my group. Their support helped me to move forward my research to successful completion. Thanks to my friends who stayed on my side over my research years in encouraging me and praying for me all the time.

Last, but not least, I greatly thank my beloved family for their immeasurable support and encouragement over the years when I was pursuing my Ph.D. degree. The support and encouragement on my studying were never stopped even during the harsh time with my family. My father and mother always respected my decisions and trusted me on every paths in studying and working. Their great trust empowered me to go through all difficult times for completing my Ph.D. degree. With the endless love I received from my family, I am here as who I am.

As a second part, I would like to acknowledge the sponsorship continued over my research years. This research was sponsored by the Defense Threat Reduction Agency – Joint Science and Technology Office for Chemical and Biological Defense Program (DTRA – JSTO, contract number HDTRA1-12-C-0048). The U.S. Government is authorized to reproduce and distribute reprints for Governmental purposes notwithstanding any copyright notation thereon.

"Distribution Statement A: Approved for Public Release; Distribution is Unlimited."

TABLE OF CONTENTS

LIST OF TABLES

LIST OF FIGURES

Chapter 1 Introduction

The outermost layer of clothing plays an important role to protect people when they are exposed to an extreme or harsh external environment. People can be threatened by harmful or toxic liquids in their working area, which may be fatal for human life. One of the critical functions of protective clothing is to provide resistance to harmful liquids, and the degree of this resistance is determined by the wetting behavior of the textile's surface. The wetting resistance of the fabric surface is determined by two characteristics: the liquid repellency and the resistance to penetration by a liquid under pressure.

A liquid-repellent surface resists the penetration of liquid into the surface structure. A hydrophobic or oleophobic surface is described as the condition where the contact angle between a solid and a liquid drop is over 90° for water or oil, respectively; superhydrophobic or superoleophobic surface is defined by the much higher contact angle, over 150° of a liquid droplet on a solid surface and the liquid rolls off a tilted surface.[1-3, 4-7] There are precedents of this characteristic found in the natural world. The lotus leaf is an example of a biomaterial that is water repellent and is characterized by superhydrophobicity, low adhesion, easy roll-off, self-cleaning, drag reduction, and low contact angle hysteresis.[6-11] For this reason, the Lotus effect has inspired researchers to mimic the surface of biomaterials to create liquid-repellent surfaces through surface modification to lower the surface energy of the solid substrate and reduce the contact area of a liquid droplet with the solid surface. This results in the decrease of adhesiveness affecting the roll-off of liquid.[12-19] Roll-off is also affected by the contact angle

hysteresis (CAH), which is the difference between the advancing contact angle and the receding angle when a liquid droplet rolls off a tilted solid surface; the difference depends on liquid properties and local geometrical structure of the surface. A low CAH leads to lower adhesion. If a substrate is superhydrophobic and has a low CAH, it will exhibit self-cleaning also known as the Lotus effect. On the surface, the liquid removes the debris or dirt as it rolls off and leaves no residue on the surface.[2, 6, 8, 19-22] Water repellent surfaces have been achieved in many research studies through chemical or morphological modification, however, it is still challenging to achieve oil repellency due to the low surface tension of oil.

In studying the surface of biomaterials, it was found that water repellent surfaces found in nature have a wax coating and multiscale roughness. The wax coating increases hydrophobicity by lowering the surface energy while the roughness reduces the contact area of liquid with the surface.[16, 20, 21, 23-27, 27-36] In research on superhydrophobic surfaces, many approaches have been used to create liquid repellent surfaces. These include applying surfactants to lower surface tension and, in other work, multiscale roughness was created through the development of fiber morphology.[10, 12, 13, 15, 29, 37, 37, 38, 38-41] Especially, structural roughness has been emphasized to produce void spaces between protuberances, which provide the creation of composite interfacial region between air and liquid. A liquid droplet is supported on the protuberances and the interface prevents the penetration of liquid inside the structures.[9, 11, 29, 37, 38, 42-45] The composite interface has a proportionate influence on superoleophobic surfaces due to the low surface tension of an oily liquid compared to water, which results in the oil's

penetrating the surface more easily.[21, 33, 46, 47] For this reason, the stability of the composite interface has arisen as a critical factor to enhance the resistance of penetration.

To determine the stability of a composite interface, Marmur[44] examined the local minimum energy state for the composite interface. Tuteja[10, 37, 38] and Quere[9, 43] studied the energy barrier for the composite interface to keep a liquid droplet in a local minimum equilibrium state. A high energy barrier prevents the transition from composite interface to homogeneous interface, in which the liquid fills the grooves between protuberances, and penetrates through to the bottom of the grooves. The two different interface regions of a liquid droplet on a rough surface have been given in early studies: the homogeneous interface by Wenzel[48] and the composite interface, also known as the heterogeneous interface, by Cassie and Baxter.[49] In the Wenzel state, the liquid fills the spaces between protuberances, while in the Cassie-Baxter state, liquid stays on top of the protuberances. In addition, the metastable Cassie-Baxter state was introduced to describe the situation where the Wenzel state is the equilibrium state but the system is in the Cassie-Baxter state. Application of external pressure or impact of the liquid in the metastable Cassie-Baxter state causes the system to transition from the Cassie-Baxter state to the Wenzel state: in other words, from the composite interface to the homogeneous interface.[11, 20, 26, 44, 46] Increasing the energy barrier between these two states enhances the prevention of the transition as pointed out in other studies. Tuteja et al.[10, 11, 38] described the high energy barrier as leading to higher breakthrough pressure, which is the force required for the liquid to penetrate into fabric structures. Higher breakthrough pressure results in larger

resistance against liquid penetration. Multiscale structures can play a critical role in generating the multi-steps of a composite interface region that a liquid droplet could pass through to touch and completely wet the surface.

For this reason, altering the geometrical structures of fibers, yarns, and fabrics is considered important as a potential method to magnify the energy barrier; thus, many researchers are focusing on the morphology on fiber surfaces. The geometrical structures of woven fabrics can also assist the creation of multiscale structures especially at the macroscale, which results in the reduction of the contact area of the droplet and creates multiple energy barriers.

Several studies have been conducted on the contact angle and the roll-off angle of liquid on different woven structures.[50-52] Influencing factors were the float length and interlacing points. Further improvement of woven structures to achieve liquid repellent surfaces can be extended from the understanding of the basic geometrical structures of woven fabric. Peirce modeled the circular cross-section geometry of yarn without the consideration of pressure.[53] Kemp[54] and Hearle et al.[55] extended the Peirce model to the race-track cross-section geometry of yarn and the lenticular cross-section geometry of yarn, respectively, to take into consideration the tension which occurs while interlacing warp and weft yarns.[56-60] The types of fibers and yarns also play an important role for determination of the performance of woven fabrics.[61-66] Moreover, the geometry of fibers and yarns should also consider the cross-section shape of fibers, fiber packing in a yarn, yarn twist, etc.[62, 67] To maximize the geometrical structure of

woven fabric for a liquid repellent surface, an understanding of the relationships among fibers, yarns, and fabrics is required.

This study will approach the geometrical design of woven fabrics to enhance the wetting behavior of low surface tension liquids. For that, an understanding of the liquid properties should be established to identify the most influential factors on wetting behavior. Then, a powerful weave structure and its geometry will be determined through theoretical models capable of predicting liquid wetting behavior accompanied by testing actual woven fabrics.

Several limitations have been found in recent studies that have attempted to predict the liquid wetting behavior of woven fabrics. Liquid deposition is not completely understood on woven fabric surfaces, and the fabric structures that have been modeled are quite limited in their impact on the wetting behavior. The models that exist do not take into consideration fabric density or the varying void spaces within a woven fabric, and the models do not consider the yarn compression occurring where the warp and weft yarns interlace, which could be modeled using a lenticular cross-section for the yarn.[33] Finally, the studies have not considered the effect of a yarn's geometry which is influenced by the characteristic of the fibers used. In this work, efforts will be made to reduce these limitations in modeling the wetting of the woven structures. The improved models will be evaluated by experimental testing of the predicted liquid wetting behavior of woven fabrics. This work will contribute to developing safer outermost garments that prevent any penetration of harmful liquids.

The overreaching goal of this research is to create a woven fabric that is super-repellent and liquid penetration resistant. Therefore, the specific objectives of this study are:

1. Develop geometrical models using circular and lenticular cross-section yarns for the prediction of liquid wetting behavior in selected woven structures.
2. Create woven fabrics with the modeled weave structural geometries, varying the fabric surface roughness and the void spaces containing air.
3. Evaluate wetting behavior of the actual woven fabrics using the woven fabric's contact angle (CA) and verify the developed geometrical models of yarn and woven fabric by comparing the predicted CA with the actual CA.

Figure 1.1 presents the schematic diagram of research from the geometrical model of woven fabrics to evaluation. Before developing the geometrical model, three fundamental weave structures were selected through conducting a market review in outdoor wear, sportswear, protective wear, and military uniforms. Three basic weave structures were modeled using a circular yarn and lenticular yarn, then the loosely packed yarn structure model was incorporated into the weave structure model. The theoretical models of the weave structures were utilized to predict the liquid's contact angle (e.g. dodecane). The incorporated model of the loosely packed yarn structure reflected the effect of micro-scale void spaces between fibers on the fabric's resistance against oil. Based on the predicted high performing weave structure, the commercial woven fabrics were randomly collected from the available retail market offering, and the NCSU manufactured woven fabrics were prepared using the facilities in the

College of Textiles, NCSU. The collected commercial woven fabrics and the NCSU manufactured fabrics were tested as the first series of experiments. Through evaluating the wetting behavior of oil, a high performing structural geometry (e.g. weave structure, cover factor of warp and weft yarn in woven fabric) was determined to create woven fabrics using smooth surface yarn (SY) and rough surface yarn (RY). The hand-woven fabrics with SY and RY defined the impact of the micro-scale and macro-scale void spaces on oil resistance. The result of the liquid wetting behavior from the hand-woven fabrics was compared with the predicted behavior to verify the developed geometrical models. The experimental results were also statistically analyzed to explain correlation of the measured contact angle with the geometrical parameter. The theoretical model and the empirical observation identified the high performing structural geometry in a yarn and in a woven fabric to improve oil resistance.

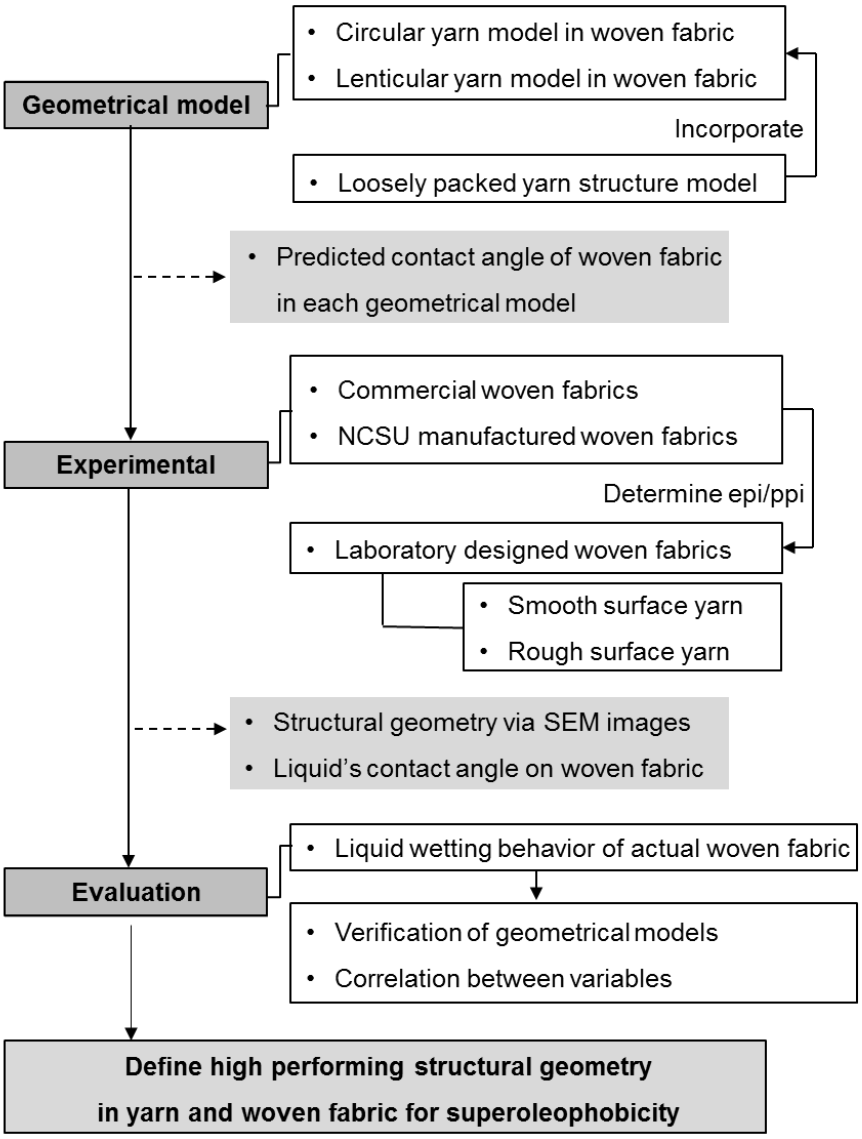

Figure 1. 1 Schematic diagram of research

Chapter 2 Literature review

In this review, we will study liquid wetting behavior, cross-sectional and axial shapes of fibers, fiber packing in a yarn, and woven structure geometries. These will provide fundamental geometries in fibers, yarns, and woven structures which impact roughness and openness of woven fabrics, including air inside the fabric structure.

2.1. Constructional components of woven fabric impacting superoleophobicity

The construction of woven fabric includes formations of fibers and yarns, and interlacements of warp and weft yarns, which result from weave patterns leading to specific woven structures.[61-63, 68] Fibers are obtained from plants, hairs, or synthetic polymers with different cross-sectional shapes, and the types of fibers strongly influence the determination of fabric properties.[69-71] The yarns are formed by packing fibers into a yarn, which allows the increase or decrease of the fabric property: physical or mechanical properties.[72] Enhancing the geometry of the woven structures plays a critical role in maximizing the performance for specific end uses.[51, 57, 64, 73-75] The different woven structures such as plain, twill, or satin (or sateen) can be utilized and the parameters of the geometric structure can be varied to find the condition optimizing the fabric properties. Therefore, fibers, yarns, and weave structures should be considered together to reach the maximum performance of fabrics for particular end uses.

For the proposed research on superoleophobic fabrics, fiber shape and surface properties, yarn structures, and fabric geometries combine to give the final properties. This review is begun with a discussion of the factors that result in oleophobicity and superoleophobicity. Then we provide a brief review of fiber surface treatments and fiber shape as it affects yarn packing factors.

2.1.1. Superoleophobicity

Liquid repellent surface

On a smooth or a rough surface, if the contact angle between a liquid and the surface is < 90°, the surface is hydrophilic or oleophilic, and if > 90°, it is a hydrophobic or oleophobic surface as shown in Fig. 2.1.[1-3, 4-7] Hydrophobic or oleophobic surfaces have a resistance to liquid penetration inside the structure, while hydrophilic or oleophilic surfaces absorb liquid and become wet quickly. However, the hydrophobic or oleophobic surface property is not sufficient to completely repel a liquid droplet of water or oil since small amounts of residual liquid can remain on the solid surface. To achieve a much higher liquid-repellency, a superhydrophobic or superoleophobic surface is desired where the contact angle is over 150°,[1, 3, 11, 13, 38] which can minimize the contact area between the liquid droplet and the solid surface. It allows the liquid droplet to roll off the surface at a low tilt angle. The contact area will be minimized the most when the contact angle reaches nearly 180°. For years, many studies have attempted to achieve high contact angles between the liquid and the solid by using chemical

treatments and morphology modification to reduce surface energy and increase surface roughness.[1, 3, 8, 12, 14, 17, 20, 37, 50, 104-109]

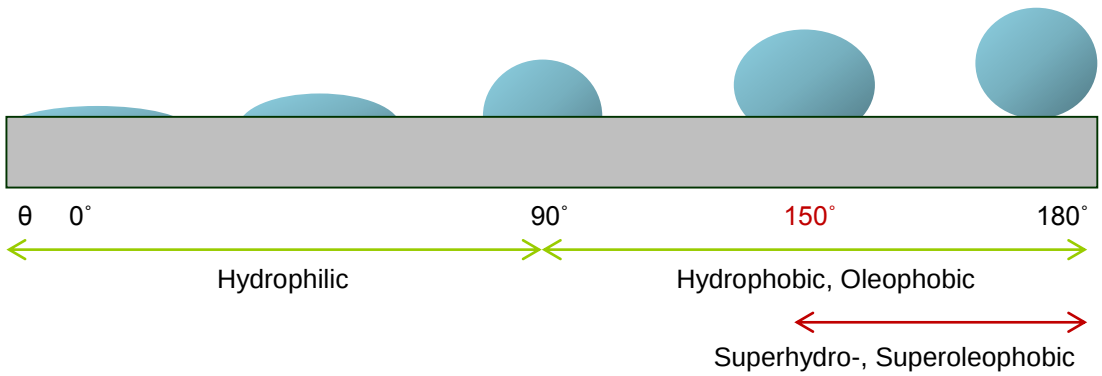

Figure 2. 1. Contact angles of a droplet on a solid surface.

The lotus leaf is a representative water-repellent surface found in nature; it exhibits superhydrophobicity and low contact angle hysteresis (CAH). Contact angle hysteresis (CAH) is the difference between the advancing contact angle and the receding contact angle when a liquid droplet rolls off a tilted solid surface (Fig. 2.3).[1, 21, 22, 25, 31] This is minimized when the receding angle approaches 180°. A liquid with low contact hysteresis can remove surface debris or dirt as it rolls off a tilted solid surface.[8, 30, 108, 110, 111] The features of the superhydrophobic and self-cleaning effect of the lotus leaf are attributed to its hierarchical structure and hydrophobic wax coating on the surface; the leaf surface is composed of microscale and nanoscale protuberances, which create void spaces to construct a liquid-vapor

interface. The interface plays a critical role to resist water penetration into the grooves by reducing the contact area and the adhesiveness of a liquid. In addition, the wax coating reduces the surface energy of the lotus leaf.[21, 23, 24, 28] The combined effect of hierarchical structures and decrease of surface energy leads to the water repellent surface of a lotus leaf. The deposition of a liquid droplet on a hierarchical structure is shown in Fig. 2.2. Repellency of water is now well established, however, the roll-off of an oil droplet is still difficult to obtain due to its much lower surface tension compared to water. For an oil repellent surface, the hierarchical structure is much more critical and is benefitted by having small protuberances on the solid surface. Since oils have a low surface tension, the chemical treatment of the surface should also be selected to reduce the surface energy; the combined effect of roughness and low surface energy will lead to the low adhesiveness of oil on the solid surface.

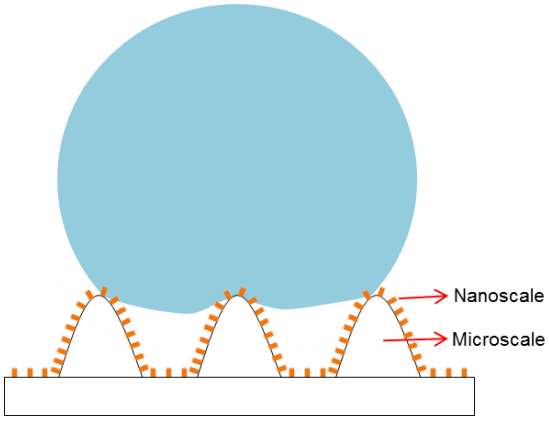

Figure 2. 2. Deposition of a liquid droplet on a hierarchical structure composed of micro- and nanoscale protuberances (lotus leaf).

Roll-off angle of a liquid droplet

A liquid droplet rolling off a tilted solid surface is shown in Fig. 2.3. When roll-off begins, the advancing contact angle becomes closer to 180°. The receding contact angle varies with the surface tension of liquid and the local structure of the surface. The roll-off angles are influenced by a droplet's volume as shown in Eq. 2.1.[1, 8, 20, 22]

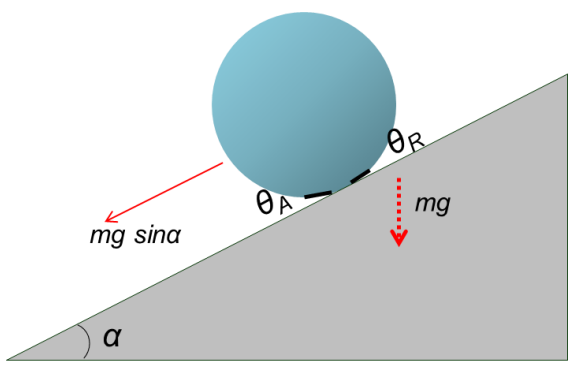

Figure 2. 3. Roll-off of a droplet on a tilted solid surface.

$$mg\sin\alpha = -D\gamma_L(\cos\theta_A - \cos\theta_R) \tag{2. 1}$$

where, θ_A is an advancing contact angle, θ_R is a receding contact angle, mg is the mass of a liquid, D is the diameter of the wetted area, and α is the roll-off angle. If the droplet is large enough even for large contact angle hysteresis, roll-off can occur on an inclined surface with an inclination angle less than 5°. On the other hand, if the droplet is smaller than the underlying structure of a rough surface, it cannot roll off unless the contact angle hysteresis is very small.

2.1.2. Fiber

Both the fiber cross-sectional shape and the axial shape of fibers affect how closely they can be packed in the yarn, i.e. it affects the open space in the yarns.

Cross sections of natural fibers and man-made fibers

The shape of the cross-section of a filament is critical to characterize fiber properties such as physical or mechanical properties, wetting behavior, reflectance of light, and their packing into a yarn. Hsieh et al.[85] also pointed out that the wetting behavior of fibrous assemblies is affected by the fiber cross-sectional shape. It plays a critical role in achieving a superhydrophobic or superoleophobic liquid repellent surface. Examples of cross-sectional shapes include circular, lobed cross-sections such as a dog-bone, and triangular cross-section shapes, which affect hydrophobicity by reducing the liquid-solid contact areas or hydrophilicity by increasing the liquid wetting areas compared to round cross-sections.[51, 53, 70, 84] The cross-sectional shapes of natural fibers or man-made fibers can also be distinguished; for man-made fibers, the cross-section shapes are manufactured for the required end-use properties and controlled by spinneret design, while natural fibers are genetically developed with their own cross-section for each type of fiber as given in Table 2.1.[62, 66, 70, 71]

Table 2. 1. Types of natural fiber cross-sections

Cross-sections of natural fibers		
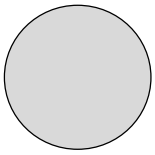	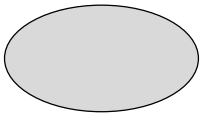	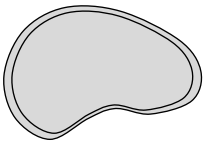
Round	Oval	Tubular
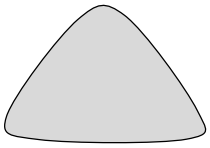	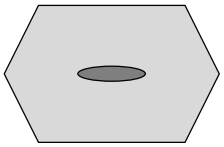	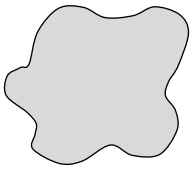
Triangular	Polygonal (central lumen)	Irregular

Table 2.2 shows types of cross-sections of man-made fibers. Man-made fibers can be homogenous or heterogeneous, depending on the number of constituent polymers. A single polymer is used to make homogenous fibers while two or more polymers are used to make heterogeneous fibers. Heterogeneous fibers are categorized as side-by-side, sheath-core, and matrix or islands-in-the-sea. These are usually referred to as bi-component or bi-constituent fibers. In the case of side-by-side fibers, different thermal expansion of the two polymers leads to self-crimping and thus, reduce fiber packing within a yarn.[62, 66, 71]

Table 2. 2. Types of cross-sections of man-made fibers

Cross-sections of man-made fibers		
Homogeneous		
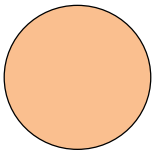	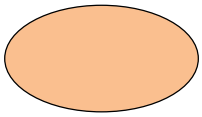	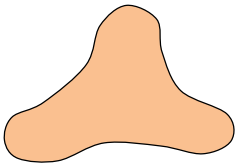
Round	Oval	Trilobal (penta-, etc.)
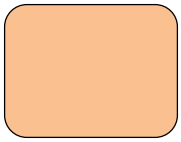	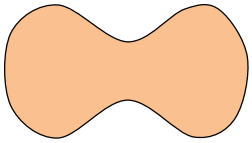	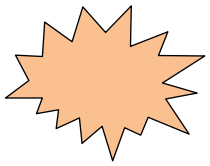
Rectangular	Dog bone	Irregular, serrated
Heterogeneous		
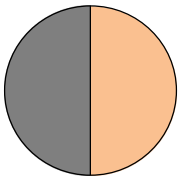	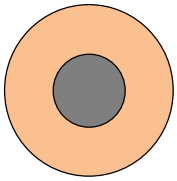	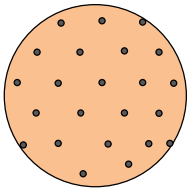
Side-by-side (mushroom like)	Sheath-core	Matrix (or Islands-in-the-sea)

Lengthwise structure variation

Modification of lengthwise structures of fibers or yarns can improve roughness and openness in fiber structures or yarn structures. The cross-section shapes of fibers discussed in the previous section affect the lengthwise structures. Also, texturing filament yarns or changing morphology of fiber surfaces can be considered to create the lengthwise structures in fibers

and yarns. The texturing of filament yarns makes yarn structures bulky, increasing the roughness and openness of the yarn structure. For thermoplastic materials such as nylon, the texturing process includes real twist or false twist, heat-set through heating and cooling by the glass transition temperature (T_g), separation, and relaxation. On the other hand, non-thermoplastic materials such as rayon utilize air-jet texturing, passing the filament yarns through highly turbulent airflow.[72]

Another method to alter the fiber cross-section in a study by Lou has been inspired by duck feathers, which consist of hierarchical branched structures leading to more open structures. Lou developed a continuous fluid coating process creating separated drops on a monofilament surface. The coating process includes passing a fiber through a liquid bath, UV curing, surface drying, and filament winding. The drop formation contains cylindrical initial coating and fluid coating separation. The separated drop shape has been distributed on the fiber surface and the height of the drop shape reached 2.28 times of filament radius.[149] The roughness and openness produced in the lengthwise direction of fibers create distances between neighboring fibers when the fibers are packed into a yarn formation. In other words, the roughness and openness in the fiber structures enhanced the roughness and the openness in the fibers-packed yarn structures.

2.1.3. Yarn

Yarns are classified into filament yarn and spun yarn; filament yarn is long and continuous, and spun yarn is made of relatively short staple fibers. Filament yarn has a very simple structure and can be modified by texturing, crimping, or twisting to change or improve the properties of the yarn, such as bulkiness, texture, stretchiness, or strength. On the other hand, spun yarn is produced with natural or synthetic staple fibers through several processes: blending, cleaning, opening, drawing, and spinning to arrange the fibers for the construction of a yarn. Twisting level is a variable for the change of yarn properties; twisting affects the hairiness of the yarn surface, fiber packing coefficient, yarn strength, etc.[62, 67, 72, 77] In addition, filament fibers can be cut into short lengths to produce staple fibers, which are processed as described above.

Packing fibers for yarn construction

Monofilament and multifilament yarns display different yarn properties (Fig. 2.4): a multifilament yarn is much more flexible than a monofilament yarn and contains more void spaces for the same linear density. For multifilament yarns, the number of filaments in a yarn influences yarn properties; a larger number of filaments in a yarn leads to denseness and compactness of multifilament yarns, which results in smoothness and uniformity of the yarn. The filaments in a yarn can be rearranged under applied forces during twisting, bending, or pulling. Tightly packed filaments rarely move while loosely packed filaments easily move under specific pressure. Thus, the packing density of filaments in a yarn is important for the re-arrangement of filaments as well as the yarn's properties.[62, 67]

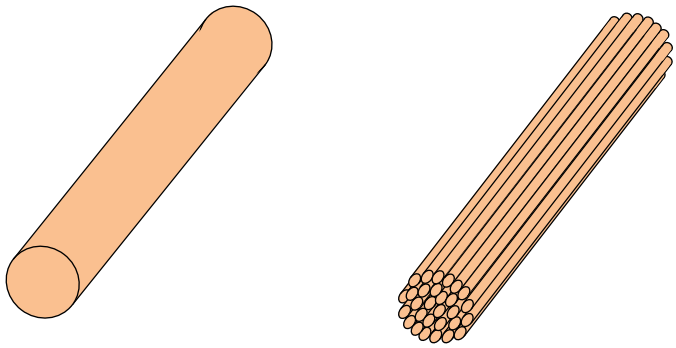

(a) (b)

Figure 2.4. Manmade (a) monofilament and (b) multifilament yarns.

The filaments or fibers assembled into a yarn may pack in a circular shape with open-packing or in a hexagonal shape with close-packing as shown in Fig. 2.5. [55, 62, 67]

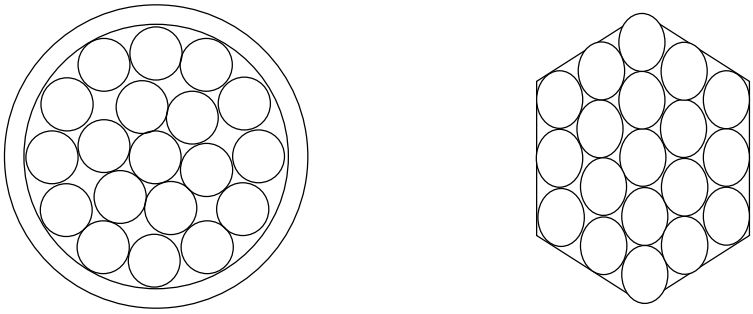

(a) (b)

Figure 2. 5. (a) Circularly open-packing and (b) hexagonally close-packing with three layers

(Image from Ref. 55, 62, 67)

For open packing, the equation to calculate yarn diameter and the number of fibers for round fibers is:[55, 62, 67]

$$2R_y = (2N-1)2R_f \tag{2. 2}$$

where $2R_y$ is the yarn diameter circumscribing the fibers in the Nth layer, and $2R_f$ is the fiber diameter. The number of fibers in the Nth layer is expressed as follows: [55, 62, 67]

$$n = 2\pi(N-1) \tag{2. 3}$$

For close packing, the yarn diameter circumscribing the Nth layer and the number of fibers in the Nth layer are:[55, 62, 67]

$$2R_y = 2(N-1)2R_f \tag{2. 4}$$

$$n = 6(N-1) \tag{2. 5}$$

where, the subscripts, *f* and *y*, refer to fiber and yarn, respectively. The total number of fibers from 1st layer to N^{th} layer can be calculated by:[67]

$$S = \sum_{i=1}^{n} n_i = 1 - 3N + 3N^2 \tag{2. 6}$$

Another way to define the yarn diameter is to use the fiber properties such as the fiber density, ρ_f (g/cm^3), the fiber packing coefficient, ϕ, and the linear density of yarn in a unit length (g/cm), N_d, as given by:[5]

$$2R_y = \frac{1}{280.2}\sqrt{\frac{N_d}{9\phi\rho_f}} \text{ (cm)} \tag{2. 7}$$

Fiber packing coefficient

The packing coefficient, ϕ, is a useful parameter to define how tightly the filaments are packed, which is expressed by the ratio of the density of the yarn to the density of the fibers:[55, 62, 67]

$$\phi = \frac{\rho_y}{\rho_f} \tag{2. 8}$$

The packing coefficient is also equal to the cross-sectional area for the fibers divided by the cross-sectional area of the yarn:

$$\phi = \frac{n\pi R_f^{\ 2}}{\pi R_y^{\ 2}} = n\left(\frac{R_f}{R_y}\right)^2 \tag{2. 9}$$

where, n is a number of fibers in a yarn.

Influence of cross-section shapes on packing fibers in a yarn

The shape of the cross-section of filament fiber plays a critical role to determine spaces between filaments in a fiber assembly; filaments with a circular cross-section will pack more closely in a yarn than other cross-sections such as multilobal, dog bone, rectangular, etc. Multilobal fibers will create larger void spaces than circular, dog bone, or rectangular cross-sections. The large void space allows improvement of the air permeability, moisture absorption, and quick drying properties of fabrics. Also it is a critical component for the development of superoleophobicity and superhydrophobicity due to the strong influence of void space on the wetting behavior.[62, 67, 71] According to the Cassie-Baxter equation, the void spaces reduce wetting if the filaments are oleophobic or hydrophobic.

The representative packing coefficient of different yarns was given by Scardino[86] for monofilament, multifilament, and staple fibers (Table 2.3); for staple yarns, a different method of yarn spinning shows a different packing coefficient and yarn twisting tends to increase the packing coefficient by decreasing the relative volume of yarn to the volume of fibers.[62, 86]

Table 2. 3. Representative packing coefficient of different types of yarns

Types of yarns	Packing coefficient (ϕ)
Monofilament	1.00
Multifilament	
Untwisted	0.25
Regularly twisted	0.60
Hard twisted	0.90
Staple yarn	
Soft twisted	0.33
Hard twisted	0.60
Yarn spinning	
Ring spun	0.50-0.60
Rotor spun	0.35-0.55
Friction spun	0.30-0.55
Wrap spun	0.40-0.70

(Ref. 62 and 86)

2.1.4. Woven fabric

Woven fabrics are classified by the formation method, such as dobby, jacquard, leno, and pile fabrics as shown in Table 2.4. Fabrics are constructed of fibers and yarns, which are critical components that determine the performance characteristics. Thus, the properties of woven fabric strongly depend on the types of fiber and yarn used for fabric construction. The structure of woven fabric also influences the fabric properties.[55, 63, 77, 88, 89] The constituent fiber, yarn and woven structures play important roles in the features of the fabric. Therefore, they must be combined properly to obtain the desired performance of a fabric, such as waterproof, windproof, breathability, and high physical or mechanical strength. Wetting behavior is also influenced by different geometries: fiber cross-section, protuberances on fiber surfaces, and different weave structures, e.g. plain, twill, satin, etc. According to the study by Hasan et al.,[51] plain weaves showed a higher contact angle for a water droplet than a twill structure, which they attributed by the compactness of the plain structure; a twill having longer float lengths than plain. The larger space caused by the longer float length can allow liquid to penetrate easily into the structure. By manipulating the geometric structure, superhydrophobicity or superoleophobicity can be obtained. As discussed in section 2.1.1, superoleophobicity is determined by the air in the fabric structure. The void space minimizes surface energy and supports the liquid to float on the fabric surface. For this reason, the void space should be maximized by appropriately designing the fabric formation components such as fiber, yarn, and weave structure.

However, prior studies of the effect of woven structures on superoleophobicity are not sufficient. Nearly all repellency studies of woven fabrics are of surfaces with chemical treatments and through the development of rough fibers.[7, 60, 65, 84, 86, 88, 90, 91] Therefore, further study is required on woven fabrics with different weave structures to identify the better performing structural geometry of woven fabric for superoleophobicity. Woven fabrics are made of warp and weft yarns that are interlaced perpendicularly to each other; warp yarn is the vertical or machine direction yarn while the weft yarn is the cross-machine direction yarn or pick. The pattern refers to the order of the interlacing of warp and weft yarns.[22, 61] Various weaving patterns can be created through the arrangement of interlacing, which results in different structures with different properties.

Table 2. 4. Classification of woven fabrics

Woven fabrics	
Dobby	A patterning mechanism to weave fabric by controlling the lifting shaft of warp yarn, which creates a small repeat pattern: 12, 16, or 24 shafts
Jacquard	Another patterning mechanism to weave larger and intricate patterns by lifting individual ends by hooks in a Jacquard harness
Leno	Special pattern created by twisting warp yarns in pairs; light openness in fabric structures and special heddles and looms required
Pile	Two main methods for pile fabrics; cut pile created by cutting threads between cloth layers or on the face of fabric and loop pile produced by cutting threads that form the loops

(Ref. 64 and 77)

Categorization of weave structures

Woven structures can be categorized by basic structures and advanced structures (Table 2.5). The basic structures are elementary bases for more advanced woven structures,[45, 92] which include simple plain, twill, and satin which have floats in a repeat unit of the structure. Float refers to a weft yarn as it passes over or under warp yarns, or a warp yarn as it passes over a weft yarn. Advanced structures can be obtained by extending the simple basic structures into complex structures, or by combining the basic structures into a complex structure.[77, 84, 86, 93]

Basic plain structure

The plain weave is the most commonly used woven structure and is also referred to as tabby, linen, or taffeta weave, and is shown in Fig. 2.6. It is the structure where the warp and weft yarns alternate in the same manner. Plain woven fabrics are firm, stable, lightweight, and have low absorbency. Thus, it is widely used for high performance textile applications such as sportswear, outdoor gear, protective wear, and military wear. Ripstop fabrics, usually nylon, are also plain structures; however, the resistance to tearing has been enhanced by interweaving thicker yarns at regular intervals within a thinner woven fabric. Therefore, small tears are prevented from spreading easily by the thicker yarns.[63, 77, 92, 94]

Table 2. 5. Basic and extended weave structures

Weave structures	
Plain	The most basic and simplest structure with the largest number of interlacing points which is woven by lifting a warp yarn alternately to pass over and under a weft yarn: firm and strong: 1/1 ➔ Fabrics: canvas, chiffon
Basket	Two or more warp and weft yarns passing over and under the same number of weft or warp yarns; creating less interlacing than plain: 2/2, 3/3
Warp rib	The extended warp float over several weft yarns; making warp rib: 2/2, 3/3, 2/1, 3/2
Weft rib	The extended weft float over several warp yarn; making weft rib: 2/2, 3/3, 2/1, 3/2
Twill	Unique diagonal lines in S or Z direction by floating a weft yarn over at least two warp yarns: strong and durable: 2/1,3/1,1/2,1/3 ➔ Fabrics: denim, chino, tweed
Balanced	The same number of warp and weft yarns displayed: 2/2, 3/3
Unbalanced	The different number of warp and weft yarns displayed: 1/4, 2/3
Warp faced	The diagonal lines created by weft floats: 1/3
Weft faced	The diagonal lines created by warp floats: 3/1
Satin (or sateen)	The longest float length of weft or warp yarns floating over several warp or weft yarns without any adjacent binding point: non-directional, non-diagonal line, smooth, lustrous, unstable, likely to snag: 5 ends, 7 ends ➔ Fabrics: cire satin, bridal satin, antique satin
Warp	The longest float length of weft yarns over warp yarns
Weft (sateen)	The longest float length warp yarns over weft yarns

(Ref. 64, 65, and 77)

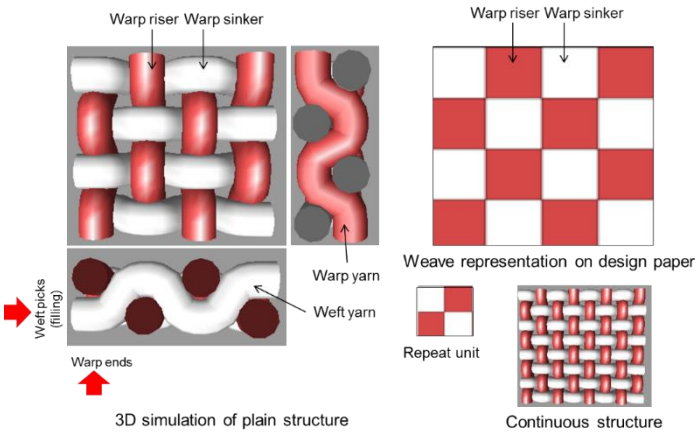

Figure 2. 6. Unit structure, continuous structure, and EAT 3D image of the basic plain woven structure. (Created by EAT DesignScope Victor software)

Extension of plain woven structure

The plain woven structure can be modified by extending the interlacing of yarn in the warp or weft directions. A warp rib structure is formed by extending the interlacing in the warp direction (Fig. 2.7), which is repeated on two ends, and weft rib structure by extending the interlacing in the weft direction (Fig. 2.8), and basket structure by extending warp and weft both directions (Fig. 2.9).[63, 77, 95]

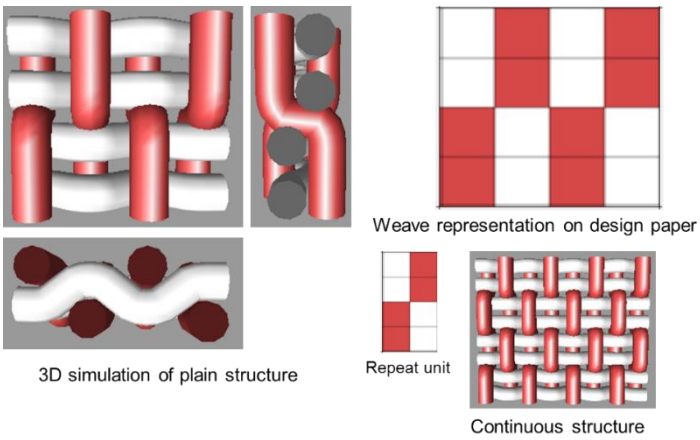

Figure 2. 7. A warp rib weave structure is shown where the interlacing is extended in the warp direction. (Created by EAT DesignScope Victor software)

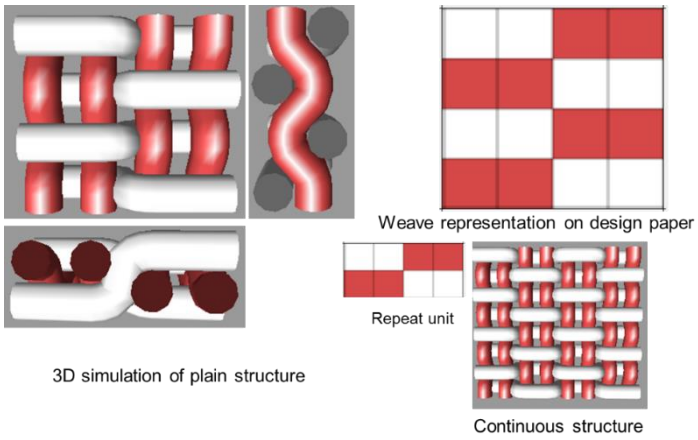

Figure 2. 8. A weft rib weave structure is shown where the interlacing is extended in the weft direction. (Created by EAT DesignScope Victor software)

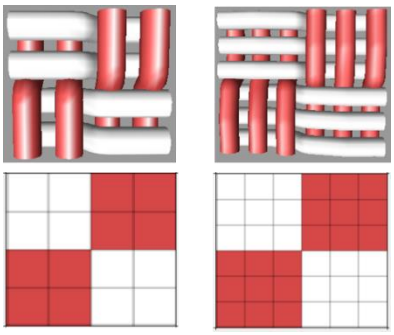

(a) (b)

Figure 2. 9. Basket weave structures are shown where the interlacing is extended in both the warp and the weft directions: (a) 2/2 (b) 3/3. (Created by EAT DesignScope Victor software)

Basic Twill structure

Twill is a basic structure perhaps best known in traditional denim, in which the twill weave has distinctive diagonal lines (Fig. 2.10). The twill line can be designed by a number of warp yarns floated over and under warp yarns by a weft yarn; for 2/1 twill, the weft yarn will cross under two and over one warp yarn. The number of warp yarns under a weft yarn changes the float length of the weft yarn; more warp yarns under a weft yarn leads to a longer float length, which results in an unstable structure.[91] Twill also has two different pattern directions in right hand (Z-direction) and left hand (S-direction), which can be combined together to create a modified twill weave pattern (Fig 2.11).[63, 65, 77]

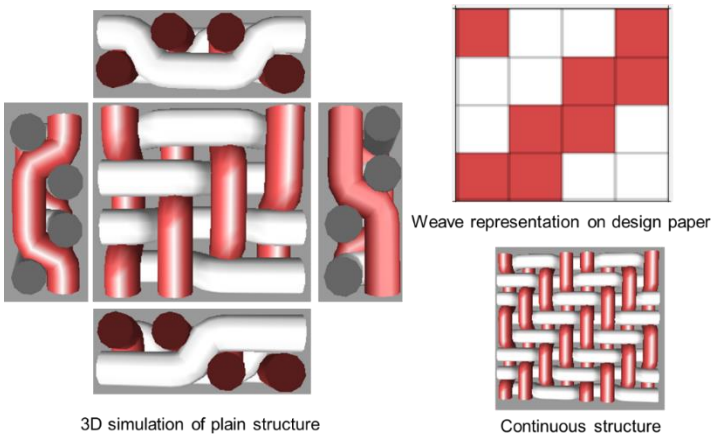

Figure 2. 10. Unit pattern, continuous pattern, and EAT 3D image of a 2/2 twill woven structure. (Created by EAT DesignScope Victor software)

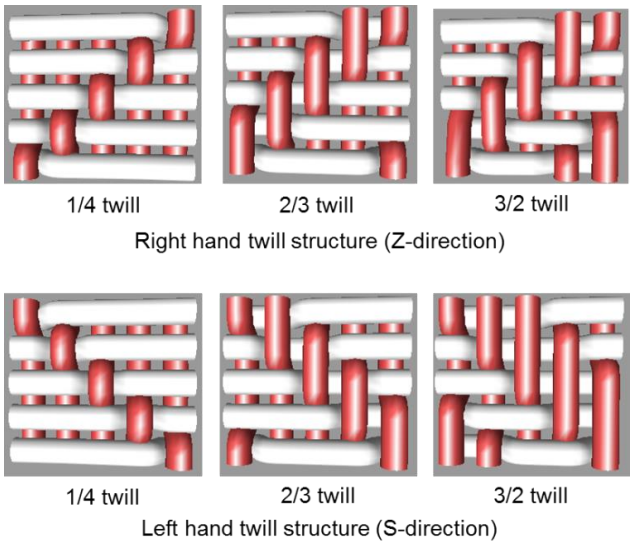

Figure 2. 11. Right hand (Z-direction) and left hand (S-direction) twill structures. (Created by EAT DesignScope Victor software)

Extension of twill structure

If the warp and weft yarns are shown with the same numbers such as 2/2 or 3/3, it is a balanced twill structure; however, if the numbers of warp and weft yarns are indicated differently, it is an unbalanced twill structure as shown in Fig. 2.12. The float length of a weft yarn, Z- or S-line direction, and balanced or unbalanced structures are important variables to create advanced twill structures. A twill structure has fewer intersection points than a plain weave structure, so it requires more ends or picks of yarns per inch, which contribute to the higher density of warp and weft yarns in its structures. Thus, a twill structure is durable, strong, and stable. Furthermore, it shows good abrasion, and snag resistance. [63, 65, 77]

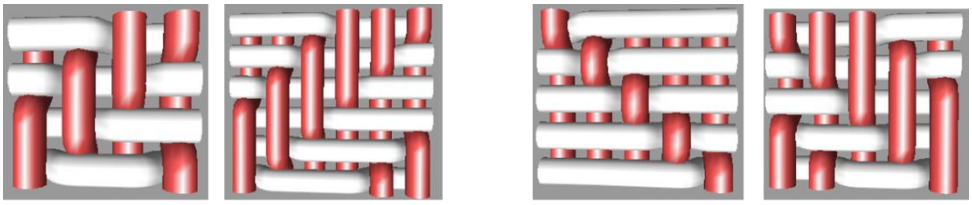

(a) (b)

Figure 2. 12. (a) Balanced and (b) unbalaced twill weave structures: 2/2, 3/3 for balanced twills, 1/4, 3/2 for unbalanced twills. (Created by EAT DesignScope Victor software)

The basic and extended weave structures determine the geometrical morphology of woven fabric, which influence the physical or mechanical properties, such as tensile or tear strength.

Many studies have been performed to understand the relationships between the weave structures and the physical or mechanical structures via testing fabrics physically and modeling of two-dimensional geometrical structures.[53, 59, 60, 88, 96-101] Peirce[53] modeled the geometrical structures of the woven fabric, and his model has been used to predict the physical or mechanical properties of woven fabrics. According to his studies, the physical properties of woven fabrics are strongly influenced by the yarn types, twisting, fabric density (picks/ends per inch), and woven structures: plain, twill, rib, or basket. Among the woven structures, plain structures have higher tensile strength than the other woven structures due to the large number of intersection points and short float lengths.[60, 102]

Although the importance of weave structures has been extensively studied for their influences on mechanical properties, few studies of their influences on superhydrophobicity or superoleophobicity have been performed. Therefore, further studies are needed to define the relationship between the geometric parameters and the wetting behavior.

2.2. Liquid wetting behavior

2.2.1. Determination of liquid wetting

Influence of surface tension

Wetting behavior of a surface is controlled by the interfacial energy among the solid, liquid, and vapor components; it is expressed as surface tension, γ_{SL} between the solid substrate and liquid, γ_{LV} between the liquid and vapor, and γ_{SV} between the solid and vapor in Eq. 2.10.[1, 7, 112] The contact angle of a liquid droplet is measured from the balanced state of surface tensions.[9] The contact angle is derived from Young's relation, which is the balance of surface tension forces on the drop. The Young contact angle is valid only on a smooth surface without any roughness (Fig. 2.13).[92, 113]

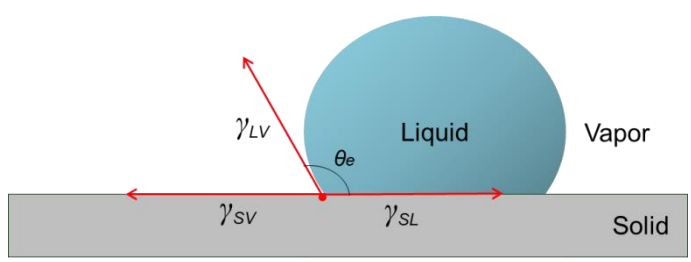

Figure 2. 13. Liquid droplet on a smooth surface.

(Image from Ref. 92)

Equation 2.10 shows Young's relation:[92]

$$\cos\theta_e = \frac{\gamma_{SV} - \gamma_{SL}}{\gamma_{LV}} \tag{2. 10}$$

On a fluorosilane, FS ($C_{13}H_{13}O_3F_{17}Si$), treated nylon 6,6 smooth film surface, the Young contact angle is 93° for water which has a surface tension of 72.8 dyne/cm, and for dodecane is 65° for a surface tension of 25.4 dyne/cm. Nylon 6,6 film shows hydrophobicity for water due to the high molecular attraction inside water, while being oleophobic for dodecane. The Young contact angle would increase on a rough solid surface when a liquid remains in the Cassie-Baxter state.

The surface tension can be characterized from intermolecular forces such as London dispersion forces, hydrogen bonds, permanent dipoles, induced dipoles, and metallic interactions, etc. Among these, three forces are dominant for surface tensions of the solid and liquid: London dispersion forces, hydrogen bonds, and permanent dipoles.[93, 94] Equation 2.11 and equation 2.12 give the surface tension of a solid and liquid which is determined by three major intermolecular forces.[112]

$$\gamma_S = \gamma_S^d + \gamma_S^p + \gamma_S^H \tag{2. 11}$$

$$\gamma_L = \gamma_S^d + \gamma_S^p + \gamma_S^H \tag{2. 12}$$

The description of the surface tension between liquid and solid originated from the thermodynamic work of adhesion, and given as the Lifshitz-van der Waals (LW) interaction energy at the liquid-solid interfacial area as shown in the Dupre equation (Eq. 2.13). The

thermodynamic work can also be expressed as the negative of the free energy for adhesion (Eq. 2.14). Equation 2.13 can also be combined with Young's equation (Eq. 2.10), and then following Eq. 2.15. Lifshitz-van der Waals (LW)'s interaction energy between a liquid and solid causes the adhesion for the thermodynamic work as given by Eq. 2.16:[109, 112, 114, 115]

$$W_{SL}^{a} = \gamma_{S}^{a} + \gamma_{L}^{a} - \gamma_{SL}^{a} \tag{2. 13}$$

$$\Delta G_{SL}^{a} = \gamma_{SL}^{a} - \gamma_{S}^{a} - \gamma_{L}^{a} \tag{2. 14}$$

$$W_{SL}^{a} = \gamma_{S}^{a} + \gamma_{L}^{a} - \gamma_{SL}^{a} = \gamma_{L}^{a}(1+\cos\theta_{e}) \tag{2. 15}$$

$$W_{SL}^{LW} = (\gamma_{S}^{LW} - \gamma_{L}^{LW}) + \gamma_{L}^{a} = -\Delta G_{SL}^{LW} = \gamma_{L}^{LW}(1+\cos\theta_{e}) \tag{2. 16}$$

Fowkes et al.[116] defined Eq. 2.17 giving the liquid - solid surface tension, in which a dispersion interaction is only considered. Equation 2.18 can combine with Eq. 2.17 and simplify with Eq. 2.19. Equation 2.16 expresses the thermodynamic work of Lifshitz-van der Waals (LW) interaction energy developed by Ostrovskaya et al.[117]

$$S_{SL}^{LW} = \left(\sqrt{\gamma_{S}^{LW}} - \sqrt{\gamma_{L}^{LW}}\right)^{2} \tag{2. 17}$$

$$W_{SL}^{LW} = 2\sqrt{\gamma_{L}^{LW}\gamma_{S}^{LW}} \tag{2. 18}$$

$$\gamma_{SL}^{LW} = \gamma_{L}^{LW} + \gamma_{S}^{LW} - 2\sqrt{\gamma_{L}^{LW}\gamma_{S}^{LW}} = \gamma_{L}^{LW} + \gamma_{S}^{LW} + \Delta G_{SL}^{LW} \tag{2. 19}$$

Lee et al.[112] studied the interfacial energy between a liquid and solid and the intermolecular forces at the interfaces, and also derived Eq. 2.20 by combining Eq. 2.11, Eq. 2.12, and Eq. 2.18.

$$\begin{aligned}
\gamma_L(1+\cos\theta_e) &= \gamma_L^d(1+\cos\theta_e)+\gamma_L^p(1+\cos\theta_e)+\gamma_L^H(1+\cos\theta_e) \\
&= 2\left(\sqrt{\gamma_S^d\gamma_L^d}+\sqrt{\gamma_S^p\gamma_L^p}+\sqrt{\gamma_S^H\gamma_L^H}\right) \\
\gamma_L^d(1+\cos\theta_e) &= \gamma_S^d+\gamma_L^d-\gamma_{SL}^d = 2\sqrt{\gamma_S^d\gamma_L^d} \\
\gamma_L^p(1+\cos\theta_e) &= \gamma_S^p+\gamma_L^p-\gamma_{SL}^p = 2\sqrt{\gamma_S^p\gamma_L^p} \\
\gamma_L^H(1+\cos\theta_e) &= \gamma_S^H+\gamma_L^H-\gamma_{SL}^H = 2\sqrt{\gamma_S^H\gamma_L^H}
\end{aligned} \tag{2. 20}$$

Based on Eq. 2.20, we can predict the Young contact angle for a droplet on a smooth surface, and this angle is used to calculate the apparent contact angle of the droplet in the Wenzel and Cassie-Baxter states.[48, 49] The contact angle is obtained when the total surface energy of the system is minimized.[115]

Liquid deposition on solid surfaces

A droplet which sits on a surface is divided into three states (Fig. 2.14); one is the fully wetted Wenzel state, another is the Cassie-Baxter state,[11, 32, 118] and the meta-stable state which lies between the Wenzel state and Cassie-Baxter state.[118, 119] Therefore, the transition between the Wenzel and Cassie-Baxter states occurs by lowering the energy barrier of the Cassie-Baxter state, which is affected by the external pressure or multiscale structure of surfaces.[120-124]

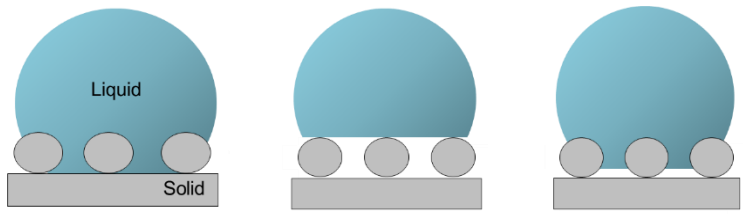

(a) (b) (c)

Figure 2. 14. (a) Wenzel, (b) Cassie-Baxter, and (c) Meta-stable states of a liquid droplet.

In the Wenzel state, a rough surface allows a water droplet to penetrate into grooves of the rough surface, and maintains a large contact area between a solid and a droplet, which leads to a completely wet surface. The Wenzel state expresses the apparent contact angle by a roughness factor, *r*, as follows:[48]

$$\cos\theta_r^W = r \cdot \cos\theta_e \tag{2. 21}$$

Equation 2.21 is used for the homogeneous interface when a liquid fills the rough structures;[125] in this state, a hydrophilic surface changes to the higher hydrophilic one as the roughness increases, but a hydrophobic surface will reach higher hydrophobicity at a higher roughness.

On the other hand, in a Cassie Baxter state, a water droplet stays on top of a rough surface without penetrating inside the rough structure if it has a certain roughness factor, *r*. The roughness creates void spaces in the structure containing air, which generates a liquid-vapor interface.[11, 37, 38] When the solid-liquid interface reaches a minimum and the liquid-vapor

interface increases, the liquid gains very little absorption energy. Finally, it will lead to a small contact area of the liquid droplet in contact with the rough surface, in which a contact angle is expressed in the following as: [49]

$$\cos\theta_r^{CB} = f_1 \cos\theta_e - f_2 \tag{2. 22}$$

f_1 is a ratio of an area in contact with a liquid to a projected area and f_2 is a ratio of an area in contact with air to a projected area.[30, 126] Equation 2.22 could be expressed by f and r_f with Eq. 2.23 as follows:[112]

$$\cos\theta_r^{CB} = r_f f \cos\theta_e + f - 1 \tag{2. 23}$$

f is a fraction of the projected area of the rough surface wetted by a liquid and r_f is a roughness ratio of the wet area.

In the Cassie-Baxter state, the liquid has a lower contact angle hysteresis than the Wenzel state due to void spaces beneath a droplet. The contact angle becomes higher as the roughness of a surface increases. In case of a perfectly flat surface, the Cassie-Baxter contact angle is equal to the Young contact angle (θ_e). Thus a micro-rough surface has higher hydrophobicity than that of a hydrophobic smooth surface. It also indicates that superhydrophobicity or superoleophobicity is more easily achieved on the micro-rough surface than on a flat surface because the micro-roughness decreases the interfacial energy by minimizing the contact area between the liquid and solid. Furthermore, if a liquid on the micro-rough surface has a low CAH when it rolls off a tilted surface, it will exhibit the Lotus effect for self-cleaning.

The difference between the Wenzel state and the Cassie Baxter state is the consideration of the void spaces containing the air beneath a water droplet on a rough surface for the composite interface. In the Wenzel state, the solid surface should be hydrophobic to obtain higher hydrophobicity by only adding roughness. However, the Cassie-Baxter state includes an explanation of the air generating a liquid-vapor interface that supports a droplet to float on the rough surface. Therefore, a water droplet on the surface of rough, hydrophobic biomaterials results in the Cassie-Baxter state.[9, 11] The contact angle is the most stable one that occurs between the receding contact angle and advancing contact angle.[44, 127, 128] The angle provided by Wenzel and Cassie-Baxter equations is the apparent contact angle which is observed as a macroscale parameter.

The Cassie-Baxter state has the stable energy of a liquid droplet on a rough surface. Also, the metastable Cassie-Baxter state appears to be an almost stable energy state (Fig. 2.14), however, it can switch into an unstable one by even a small impact or force applied to the liquid droplet. The impact or force can cause the liquid droplet to travel downward between the grooves, and drive the interfacial line of liquid and solid closer to the bottom of the rough surface. Thus, the liquid in the metastable Cassie-Baxter state can transfer either to the Wenzel or Cassie-Baxter state based on a local extreme energy. There is an energy barrier dividing the Wenzel and Cassie-Baxter states from the metastable Cassie-Baxter state that can be overcome by external forces.[121, 123, 124] If the force is larger than the energy barrier of a liquid droplet in the metastable Cassie-Baxter state, the droplet reaches the Wenzel state.

Surface energy in Wenzel state and Cassie-Baxter state

When a liquid droplet is placed on a solid surface, the Wenzel state and the Cassie-Baxter state have different surface energy gains, which is expressed as shown in Eq. 2.24:[9]

$$\Delta E = 4\pi\gamma R_0^2\left(1-\frac{R_0}{R}\right) \tag{2. 24}$$

ΔE indicates the difference of surface energies before and after the liquid droplet is deposited on the solid surface. R_0 is the droplet size before contacting the surface, and R is the radius of the spherical cap of the droplet placed on the surface. If the energy difference is small, it means that the surface energy is low enough to repel the liquid. Low surface energy can be achieved by reducing the solid surface energy by using special surfactants with low surface tension or by improving the surface morphology to reach zero-wetting, in which R is close to R_o, and then ΔE is also almost zero.[9] The Wenzel and Cassie-Baxter equations indicate the reason a higher roughness is required to achieve a higher hydrophobic surface, which can reach superhydrophobicity. Thus, to mimic the rough surface of biomaterials, multiple surface modifications are used to develop a much higher roughness on fiber surfaces using chemical and mechanical technologies.

Energy barrier transferring liquid states

The energy barrier expressed as robustness is the minimum pressure to cause sagging of a liquid into the solid structure. The force to overcome the energy barrier is the breakthrough pressure.[9, 38] The robustness of fabric to a liquid can be increased when the liquid is placed on a surface with a lower surface energy.

2.2.2. Creation of liquid-vapor interface

Laplace pressure and Capillary pressure

A solid surface composed of numerous protuberances contains multiple void spaces in the surface structure. A liquid droplet on the surface forms a liquid-vapor interfacial region that results in a pressure difference between the inside and outside of the droplet. This pressure difference is the Laplace pressure, which determines the curvature of the liquid-vapor interface as shown in Fig. 2.15.[5,32,125]

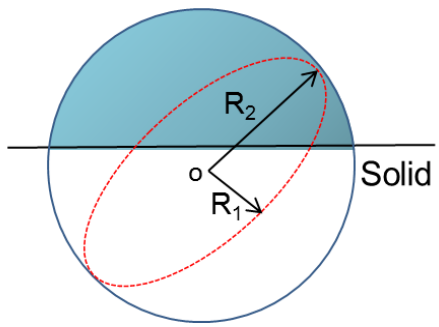

Figure 2.15 Curvature of liquid drop by Laplace pressure.

The relationship is:[5, 32, 125]

$$\Delta P \equiv P_{inside} - P_{outside} = \gamma_{LV}\left(\frac{1}{R_1} + \frac{1}{R_2}\right) \tag{2. 25}$$

where the subscript ‘inside’ means the pressure inside the drop while “outside” is the pressure outside of a liquid droplet, γ_{LV} is the liquid-vapor surface tension, and R_1 and R_2 are the two principle radii of the liquid. If the Laplace pressure is constant on the liquid-vapor interface, the liquid reaches an equilibrium state. Then, the two radii are the same if the droplet is spherical and Equation 4.37 becomes Equation 4.38 following as: [125,130]

$$\Delta P = \frac{2\gamma}{R} \quad (R_1 = R_2) \tag{2. 26}$$

The capillary pressure is another way to measure γ_{LV} through a liquid rising inside a narrow tube. The capillary pressure will reach an equilibrium state making a balance between the inside and outside pressures of the liquid in the tube as shown in Fig. 2.16.[130]

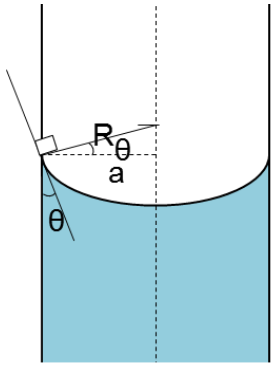

Figure 2.16. Motion of capillary pressure of liquid in a narrow cylindrical tube.

(Image from ref. 130)

In Fig. 2.16, a is the radius of a circular cross-sesction of the tube, R is the radius of a sphere generated by the capillary pressure which is determined by the contact angle θ. The relationship among a, R,and θ is following in Eq. 2.27: [130]

$$R = \frac{a}{\cos\theta} \tag{2. 27}$$

The contact angle θ is controlled by the liquid and solid energies, thus the same liquid and solid will lead to the same contact angle. Using Eq. 2.26 and Eq. 2.27 above, the pressure difference can be re-written by: [125, 130]

$$\Delta P = \frac{2\gamma_{LV}\cos\theta}{a} \tag{2. 28}$$

Because the capillary pressure reaches the equilibrium state at capillary height, h, the pressure difference is expressed as: [125, 130]

$$\Delta P = \rho g h \tag{2. 29}$$

The equilibrium state can be expressed as the hydrostatic equilibrium balanced by the gravitational force, g. In Eq. 2.29, ρ is the liquid density, and g is the acceleration due to gravity. This equation shows that the pressure difference can be measured by the capillary height, h for the same liquid and the solid surface.[125, 130]

Liquid sagging

When a liquid droplet is supported by two protuberances, the liquid-vapor interface sags below the contact points. The sagging phenomenon was studied by Tuteja et al.[10, 11, 38] to define the relationship of the sagging height with liquid and geometrical properties: capillary length and

curvature for the liquid properties, and the height and distance of protuberances for the geometrical properties. The capillary length of a liquid is defined by the relation of surface tension, liquid density, and gravity as given in Eq. 2.30;[38] l_{cap} is constant for a given liquid.[125, 130]

$$\ell_{cap} = \sqrt{\frac{\gamma_{LV}}{\rho g}} \tag{2. 30}$$

where, l_{cap} is the capillary length of the liquid.

The curvature is another way to describe the distorted liquid-vapor interfacial line, which is inversely proportional to the radius of circle as given in Eq. 2.31.[10, 11, 38]

$$\kappa = \frac{1}{R_{sag}} \tag{2. 31}$$

where, κ is the curvature, and R_{sag} is the radius of the circle created by the distortion of liquid-vapor interface. The κ is a function of l_{cap}, and can be expressed as:[10, 11, 38]

$$\kappa = \frac{2}{\ell_{cap}} \tag{2. 32}$$

The droplet curvature is determined by the Laplace pressure and the relationship between R_{sag} and l_{cap} is: [10, 11, 38]

$$\ell_{cap} = 2R_{sag} \tag{2. 33}$$

If the sagging is large enough, it may be large enough to overcome the energy barrier to transfer from a meta-stable to a global equilibrium state. Thus, the effect of geometrical

parameters on the sagging height has to be verified to enhance the geometrical model of protuberances on the fiber surface.

Geometry of liquid sagging at local surface structures

Tuteja et al. stated that the failure to sustain the liquid-vapor interface allows the liquid to touch down to the bottom of a solid surface, leading to liquid penetration into the rough structure.[10, 11, 38, 122] The liquid-vapor interface line importantly affects the liquid penetration due to the liquid sagging. The sagging phenomenon is caused by a distortion of the liquid-vapor interface line, which occurs due to the pressure difference between the inside and outside of the liquid. The liquid sagging defines the sagging height, h_1, and the sagging angle, $\delta\theta$, as shown in Fig. 2.17.

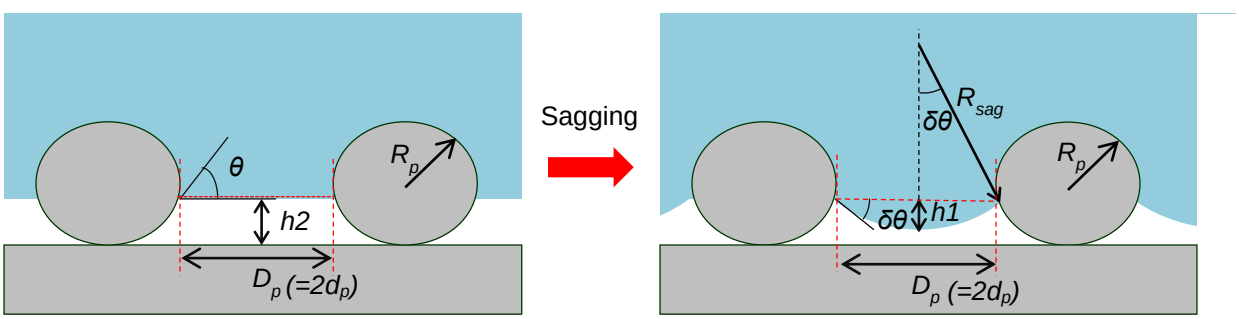

(a) (b)

Figure 2. 17. Liquid-vapor interface line (a) without sagging and (b) with sagging.

(Image from Ref. 38)

The distortion of the liquid-vapor interface line determines the sagging height and the sagging angle. Both of the geometrical numbers, h_1, and $\delta\theta$, are dependent on the liquid property. In Fig. 2.17, h_2 is the height from the flat line to bottom of the groove, D (=$2d_p$) is the width of the groove, and R_{sag} is the radius of the liquid curvature created by sagging. The groove depth will be the same with the height of the protuberance (=$2R_p$). The subscripts, p, refers to the protuberance.

Figure 2.17 shows the change of the liquid-vapor interfacial region from (a) the flat line to (b) the distorted curvature. The liquid stays in the meta-stable state, which can transit to the Wenzel-state or the Cassie-Baxter state. The transition depends on the property of solid surface for a given liquid. If the sagging height, h_1, reaches the maximum pore depth, h_2, the liquid-vapor interface line will touch the bottom of the solid surface. Then, the liquid will fill in the groove completely, changing to the Wenzel-state.[10,11,38,122] Without an applied external pressure on the liquid, gravity will be the dominant force causing the sagging. It means that the sagging height, h_1, will be equal for the same liquid. It points out that at least, h_2 should be higher than h_1 to prevent the easy penetration of the liquid into the solid structure. For the given liquid, the sagging height, h_1, will become higher as the protuberance distance increases. The relation between the sagging height and the structural geometry of roughness emphasize the creation of the optimum distance, D_p (=$2d_p$), and the height, h_p, of the protuberance to improve the liquid resistance against a fabric surface.

Tuteja et al. defined the sagging height, h_1, and the pore depth, h_2, using the geometrical parameters introduced in Fig. 2.17. The sagging height, h_1, is expressed in terms of R_{sag} and d_p as shown in Eq. 2.34:[10,11,42]

$$\begin{aligned} h_1 &= R_{sag}\left(1-\cos\delta\theta\right) \\ &= R_{sag}\left(\frac{1}{2}\sin^2\delta\theta\right) \\ &= \frac{d_p^{\,2}}{2R_{sag}} \end{aligned} \tag{2. 34}$$

It explains that the sagging height, h_1, is strongly influenced by the square of d_p, which is the distance between two protuberances generating the groove. As the distance increases, the sagging height will become greatly higher.

If the liquid droplet is too large relative to the surface structure of the solid, gravity will have a stronger impact on the sagging height, h_1.[1,2,3] The sagging height in the large droplet will become much larger than the smaller droplet as follows in Eq. 2.35:[10,11,42]

$$h_1 \approx \frac{2d_p^{\,2}}{R_{sag}} \tag{2. 35}$$

Utilizing Eq. 2.59 and Eq. 2.61, the following equation is derived to define the range of protuberance height when h_2 is a maximum pore depth of protuberances as given by:[38]

$$h_2 >> \frac{2d_p^{\,2}}{R_{sag}} \tag{2. 36}$$

The relationship in Eq. 2.35 and Eq. 2.36 shows that the height of the protuberance needs to be greater as the distance between protuberances increases in order to prevent the touch-down

of a liquid droplet. For the large droplet, the height should be much higher than that of the small droplet because the sagging height would be strongly affected by the increase of the distance, d_p. Most of all, the sagging height should be much smaller than the protuberance height. Jung et al. also found the transition from the Cassie-Baxter to the Wenzel state:[131-134] the larger distance between the protuberances will maintain the droplet in the Cassie-Baxter state. However, the range of the protuberance distance is still required to prevent the liquid penetration.

Breakthrough pressure

Breakthrough pressure, $P_{breaktrough}$, is deterimined by a robustness factor, A^*, which is defined by other robustness factors, H^* and T^*; dimensionless measures characterized by the sagging height, h, and sagging angle, $\delta\theta$ as shown in Eq.2.37:[38]

$$\frac{1}{A^*} = \frac{1}{H^*} + \frac{1}{T^*}$$
$$P_{breakthrough} = A^* \cdot P_{ref} \tag{2. 37}$$

From the definition for h_1 and h_2, H^* is derived as follows: [10, 38]

$$H^* = \frac{P_H}{P_{ref}} = \frac{h_2}{h_1} = \frac{R(1-\cos\theta)\ell_{cap}}{D_p{}^2} = \frac{h_2 \ell_{cap}}{D_p{}^2} \tag{2. 38}$$

Another factor, T^*, is the dimensionless robustness angle characterized by P_θ; a required pressure for the sagging angle, $\delta\theta$, causing advancing distortion of the interfacial region to move downward and reach the minimum angle, $\alpha_{\min}$ ($\alpha = \alpha_{\min}$, $\alpha = \theta - \delta\theta$). From the force

balance between the surface tension and the break through pressure of the sagging angle in the liquid-vapor composite interface, the robustness pressure of P_θ is defined as: [10, 38]

$$P_\theta = \frac{\gamma_{LV} \sin \delta\theta}{D_p} \tag{2. 39}$$

And, the dimensionless robustness angle is expressed by the definition of P_θ as shown:[10, 38]

$$T^* = \frac{P_\theta}{P_{ref}} = \frac{l_{cap} \sin \delta\theta}{2D_p} \quad (2.\ 40)$$

If the robustness pressures to overcome the sagging height and angle are high enough, the breakthrough pressure will be enhanced; it allows a liqud droplet to float on the solid surface, which can lead to roll-off of the liquid. The robust pressure acts as the energy barrier. If the robustness factor is larger than 1, the energy barrier is high enough "between the meta-stable composite interface and a globally equilibrated wetted interface."[44] On the other hand, if it is less than 1, the energy barrier cannot bear even a small pressure applied to the liquid-vapor interface.

Drop size impacting sagging

The droplet size is also important in determining superhydrophobicity. Roll-off of a liquid droplet can be affected by the relationship of the sticking force, γR, and the weight of the droplet, pgR^3.[9, 43] If the sticking force is lower than the droplet weight, the liquid rolls off a hydrophobic surface. Thus, the droplet size should be larger than the capillary length. When enough liquid sits on top of the protuberances in a rough surface, it will be in the Cassie-Baxter

state first; however, it will sag into the grooves between protuberances, in which the interfacial line between liquid and vapor moves down from the top line of protuberances. The interfacial lines stay at an equilibrium energy state below the droplet from the sharp edges on the protuberances as shown in Fig. 2.18.

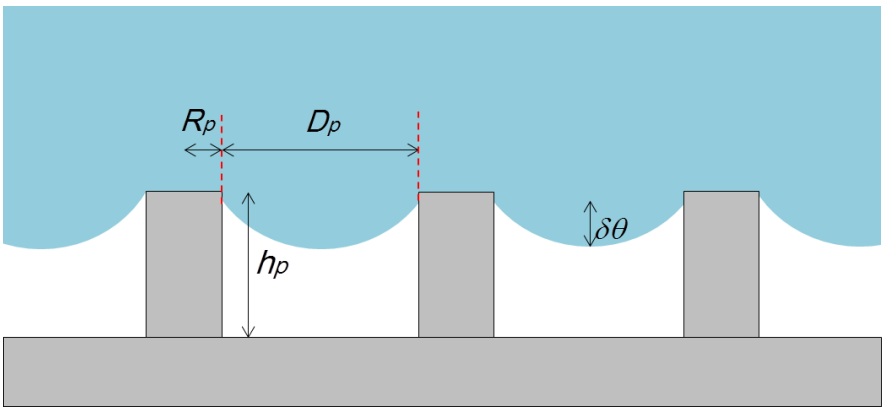

Figure 2. 18. Lowered liquid-vapor interface below a liquid droplet derived by pressure to the liquid.

(Image from Ref. 43)

In Fig. 2.18, h_p is the height of protuberances, D_p is the distance between each protuberance, and $\delta\theta$ is the length of lowered liquid-vapor interfaces below the liquid droplet, which is caused by the changed curvature of the droplet by pressure. Quere et al.[9, 43] point out that the interface curvature is governed by the radius of the droplet, R; it can increase the liquid-vapor interface length, $\delta\theta$. The length $\delta\theta$ becomes higher as the distance D_p becomes longer. The relationship

between the interface length $\delta\theta$, radius of a liquid droplet, R, and distance between protuberances, D_p, can be defined as:[9, 124, 135]

$$\delta\theta \approx \frac{D_p^{\ 2}}{R} \tag{2. 41}$$

If the value of $\delta\theta$ reaches the protuberance height, h_p, a critical radius of the droplet follows Eq. 2.41,[9, 43, 135] which indicates that the critical radius is much larger than the distance, D_p, if $D_p > h_p$. In this case, the much larger radius of a liquid droplet is required to prevent the liquid-vapor interfacial line from touching down to the bottom of a solid surface, which leads to complete wetting.[9, 43]

$$R \approx \frac{D_p^{\ 2}}{h_p} \tag{2. 42}$$

Other researchers also examined the importance of sagging caused by the deformation of a liquid droplet after sitting on the rough surface (Fig. 2.18); the deformation and lowering of interfacial line are strongly dominated by the local surface structure specified by the geometrical structure of the protuberances. Several studies pointed out that the droplet will touch the bottom surface between two protuberances if the sagging height is larger than the height of a protuberance. [131-134, 136, 137]

The equilibrium Cassie-Baxter state for such a small droplet can be obtained through reducing the distance, D_p, or increasing the protuberance height, h_p. [9, 43] The higher height of the protuberance will lead to a sufficient energy barrier to prevent the transition of the Cassie-

Baxter state to the Wenzel state. The surface energy barrier between the Cassie-Baxter and Wenzel states can be expressed as Eq. 2.43, [9, 43, 135] in which ΔE was substituted for the protuberance height, h_p, protuberacne radius, R_p, and distance between two protuberances, D_p. It shows that the energy barrier, ΔE , is proportional to the protuberance height. This energy barrier can be overcome by external pressure to the droplet or an impact. [114, 138-140]

$$\Delta E = {2\pi R_p h_p}\Big/{D_p{}^2 \gamma \left|\cos\theta_e\right|} \tag{2. 43}$$

To keep the droplet at the equilibrium energy state, a higher energy barrier is required in the liquid-vapor interface, which can be achieved via chemically or mechanically modifying the surface to increase the height of protuberances,[11] multi-scale roughness, and micro- or nano-scale fibers in the surface structure.[25, 29, 30, 32, 104, 141] These kinds of surfaces can increase the interfacial resistance between liquid and air corresponding to the interface energy barrier.[31, 108] It explains how the superhydrophobic materials work with various scales in nature to repel a water droplet. This is why the multiscale structure is highlighted to improve the wetting behavior of liquid.

Based on the study above, it is confirmed that the development of a high energy barrier is strongly recommended to prevent the breaking of the composite interface. The height of a protuberance must be higher than the sagging height of the liquid, and the distance between protuberances has to be appropriate to avoid significant sagging to reach the bottom of the grooves. As described in the previous studies, the multiscale roughness and void spaces are the

most important factors to improve fabric surface structures decreasing slippage of the interfacial line, which can be obtained from the enhanced friction between the liquid and solid structure.[11, 30, 31, 46, 108, 122]

2.2.3. Methods enhancing liquid-vapor interface energy barrier

Chemical approaches lowering surface energy

Chemical treatments on fabric surfaces have been used to achieve low surface tension and rougher surfaces, which affect the apparent contact angle determining the hydrophobicity of the surfaces. Lee et al.[1] examined the effectiveness of fluoro groups on developing superhydrophobicity by grafting 1H,1H-perfluorooctylamine and 1H,1H,2H,2H-fluorooctyl triethoxysilane on the surfaces of nylon and cotton.[1, 2, 18, 112] The experiments showed that chemical agents with fluoro groups such as fluoroamine and fluorosilane lead to lower surface energy, which results in a higher contact angle between the solid and water or oils.[2, 18, 112] Larger amounts of fluoro groups increased the contact angle. A nylon-flock fabric was grafted with PAA and $C_8H_4F_{15}N$; the grafting mechanism is drawn in Fig. 2.19. First (Fig. 2.19.a) PAA is grafted onto nylon 6,6 surfaces to attach poly(acrylic acid) chains, which increases side groups of carboxylic acid on the nylon surface. Next, these are reacted with 1H,1H-perfluorooctylamine ($C_8H_4F_{15}N$) as in Fig. 2.19.b. The $C_8H_4F_{15}N$ grafting onto poly(acrylic acid) chains of the nylon surface lowers the surface energy.[1]

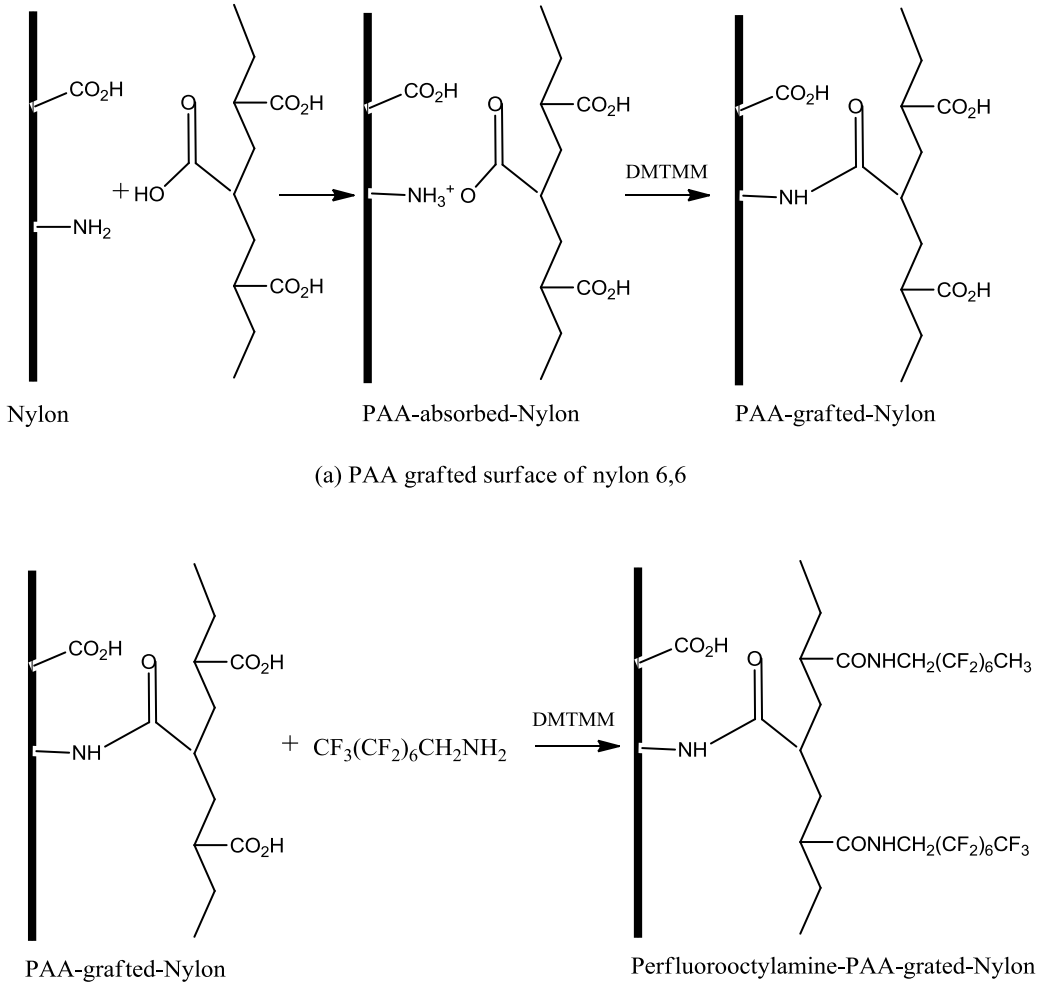

Figure 2. 19. 1H,1H-perfluorooctylamine grafting on PAA grated nylon 6,6.

(Image from Ref. 37)

The PAA-grafted surface and PAA-$C_8H_4F_{15}N$-grafted surfaces support the Wenzel state and Cassie-Baxter state. The PAA-grafted surface remains in the Wenzel state and becomes more

hydrophilic as the surface roughness is increased, while the PAA-$C_8H_4F_{15}N$ grafted nylon surface switches to the Cassie-Baxter state surface and exhibited superhydrophobicity with a contact angle up to 178°.[1, 9, 11]

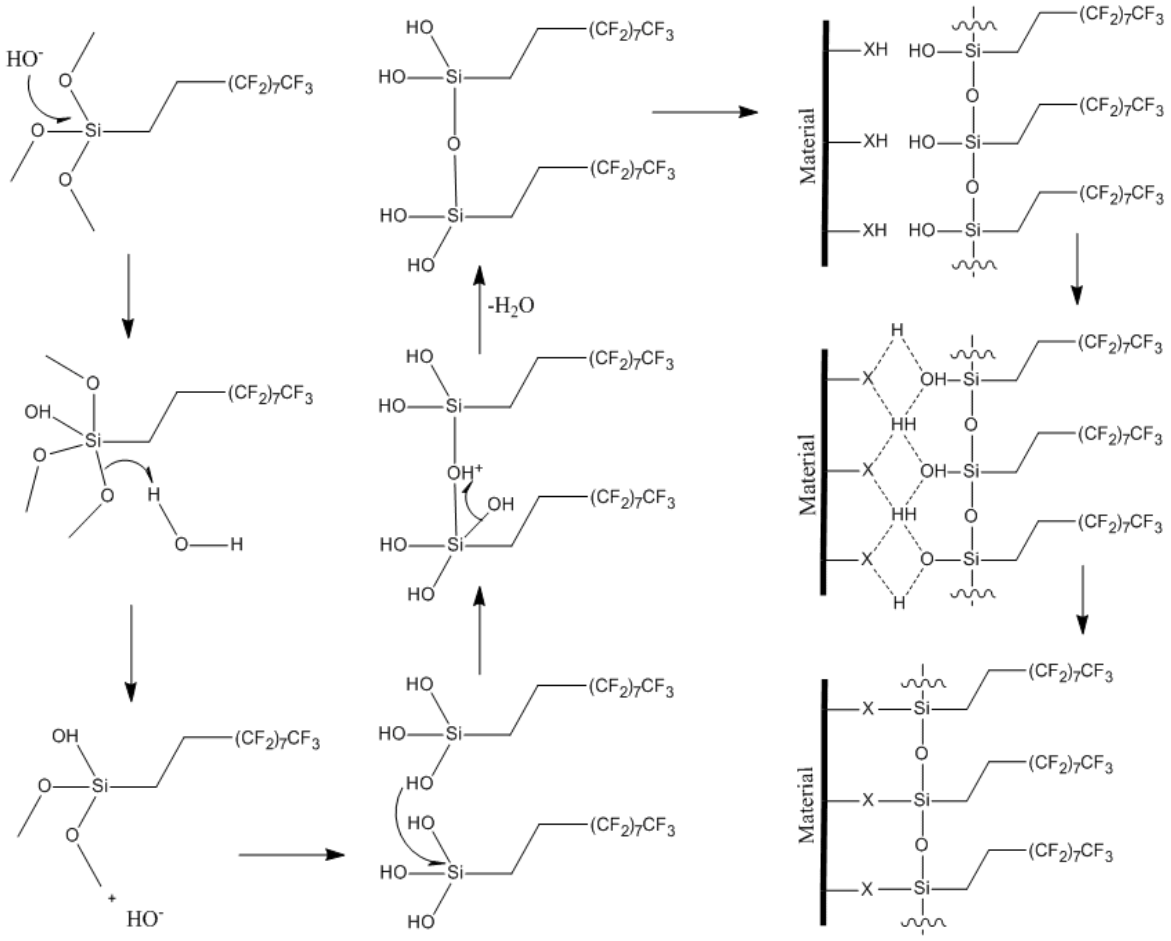

Figure 2.20. Reaction mechanism of fluorosilane condensation onto a surface.

(Image from Ref. 50)

Furthermore, Lee et al.[50] grafted NyCo (50:50 nylon 6,6/cotton blend) surface with 1,1,2,2,-tetrahydrodecyltrimethoxysilane (fluorosilane, $C_{13}H_{13}F_{17}O_3Si$) to obtain a metastable Cassie-Baxter superoleophobic surface, which is accompanied with development of surface morphology. The fluorosilane lowered the surface energy and increased the roughness, leading to superhydrophobicity for water and superoleophobicity for dodecane, achieving the high contact angles of 175° for water and 155° for dodecane.[50] The reaction mechanism of grafting fluorosilane on a surface is shown in Fig. 2.20.

Morphological approaches in fibers (nano- or micro scale protuberance)

Another way to develop hydrophobicity is to change the surface morphology to achieve a rough surface with micro-texture to mimic the surface of biomaterials with protuberances or hairiness. The concept of increasing roughness has been derived from biomaterials with superhydrophobic surfaces, such as the lotus leaf in nature. For more hydrophobic surfaces, studies have mimicked the surface of biomaterials in polymers, fibers, and engineered materials by constructing and simulating various protuberances: from single scale to multiscale geometric surfaces.

Quere et al.[9] and Tuteja et al.[11] found that biomaterials with superhydrophobicity have micro-textures such as protuberances on a leaf and hairiness around the legs of certain insects, which trap air beneath the water droplet on the surface. The air leads to a composite liquid-vapor interface in a thermodynamic equilibrium state; it allows the water droplet to stay on top of the

surface, thus not be absorbed into the surface. The composite interface between air and liquid remains in the metastable Cassie-Baxter state; which transits from the Cassie-Baxter state to the Wenzel state under external force or pressure: in other words, from a high energy state to a low energy state.[9, 11, 44, 49] For this transition to occur, it has to overcome an energy barrier which depends on liquid and surface properties; a liquid with low surface tension creates a much lower energy barrier than water, therefore, it is easily transformed to the Wenzel state. To increase the energy barrier of liquid with low surface tension, reduction of adhesiveness and drag of the liquid should be minimized on a solid surface.

Using modern technologies: flocking,[1] irradiating,[14] plasma treatment,[5] applying micro or nanoparticles,[15] and assembling carbon nanotubes have been used to increase the roughness of a surface.[13] Lee et al.[1] examined the effectiveness of creating roughness on a surface to increase hydrophobicity using a nylon-flocked surface. They showed that more roughness leads to a higher contact angle. Hydrophobicity of a rough surface could be predicted from a contact angle of a water droplet on a simulated geometry surface that followed the Cassie-Baxter equation.[9] The contact angles on a surface explain the relationship among the roughness, contact area of droplet, and contact angle in the Wenzel and Cassie-Baxter states.[1, 48, 49]

The protuberances developed by nylon-flocking were simulated as a cylindrical shape in Fig. 2.21; the parameter of R is the radius of a protuberance, h is its height, and D is the distance between two protuberances. The subscript, p, refers to the protuberance. The top of the

protuberances was considered to be flat, and the unit contact area on top of the protuberance was calculated using a square unit cell.

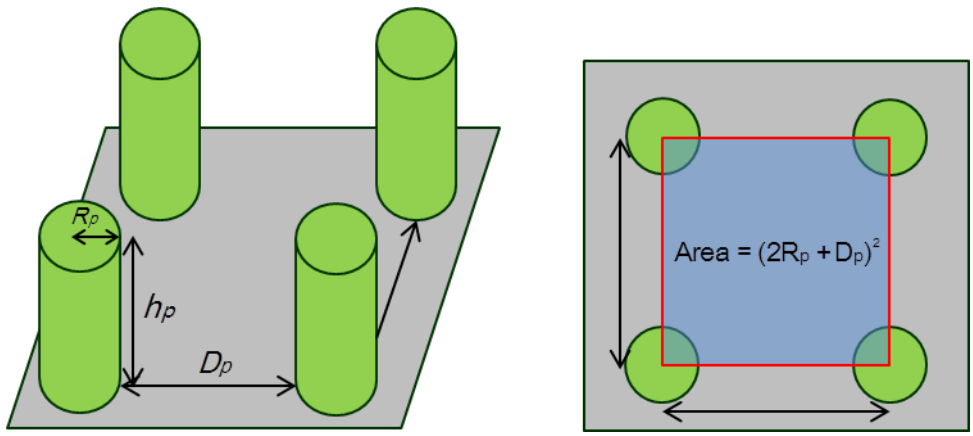

Figure 2.21. Side and top views of protuberances on a rough surface.

(Image from Ref. 1)

The roughness and wetted fraction was calculated by: [1]

$$r_p = \frac{2\pi R_p h_p}{\left(2R_p + D_p\right)^2} + 1 \tag{2. 44}$$

$$\Phi_S = \frac{\pi R_p^{\,2}}{\left(2R_p + D_p\right)^2} \tag{2. 45}$$

where, r_p is the roughness and is the wetted surface area fraction. The roughness and wetting fraction are utilized to obtain the contact angles of water in the Wenzel and Cassie-Baxter

states. The relationship between two parameters of roughness and contact angles or wetting fraction and contact angles is shown in Fig. 2.22;[1] it shows the changes of contact angles of liquid in the Wenzel and Cassie-Baxter states. The solid surface in the Cassie-Baxter state belongs to the range of superhydrophobicity if the wetted area is less than 26 % of the total top area of protuberances on the solid surface. In the Wenzel state, the wetted area lies within the range of superhydrophobicity if the roughness is increased 79 % over a smooth surface.

In this study[1], the radius and height of the protuberances for the nylon-flocked surface influenced the resulting contact angles; the smaller radius and the higher height showed a higher contact angle. On the other hand, in the case of the same radius, a higher height had a higher contact angle. Especially, the difference of the contact angle was bigger when the radius is large compared with the small one. Good agreement with the prediction of the contact angle, as shown in Fig. 2.22, was obtained when the value was calculated using Eq. 2.44 and Eq. 2.45.

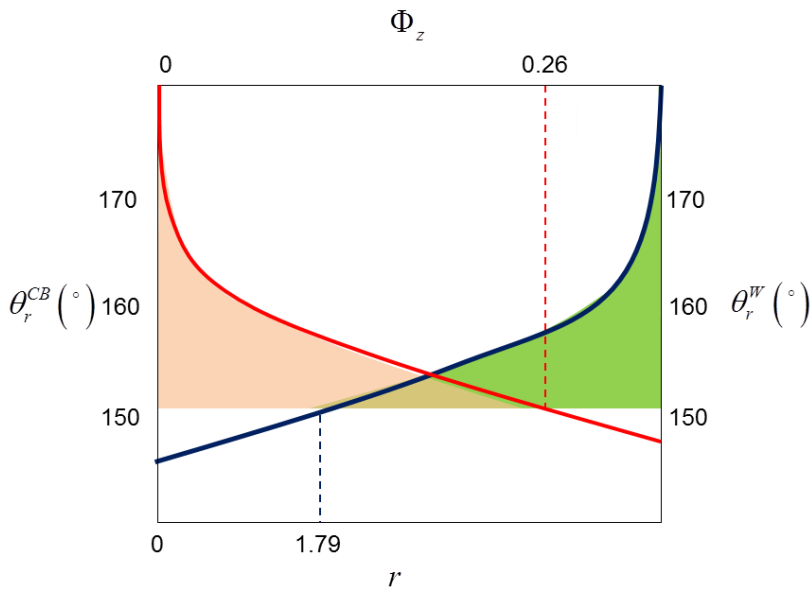

Figure 2.22. Plots of apparent water contact angles on a fluoroamine-covered rough surface in (Green) the Wenzel model and (Red) the Cassie–Baxter model (r is roughness, Φ_z is contact area of a water droplet on surface). The colored areas indicate the superhydrophobic regions.

(Image from Ref. 1)

Liu et al.[13] tried to create artificial lotus leaf structures via assembling of carbon nanotubes onto the surface of cotton substrates in which two kinds of carbon nanotubes were used as building blocks: pristine carbon nanotubes (CNTs), and surface modified carbon nanotubes (PBA-g-CNTs).[13] In this process, pristine carbon nanotubes were fabricated by deposition onto the surface of cotton fibers in water with an ultrasonic treatment. The adsorption of pristine nanotubes to cotton fiber surfaces developed nano-scale roughness on its surface. However, it had a weak affinity between the nanotubes and the cotton substrate. Thus, the wall surface of

the carbon nanotubes was treated with poly (butylacrylate) (PBA) to improve the affinity of the carbon nanotubes. The grafting of PBA on carbon nanotubes changed the surface properties of cotton fibers into a superhydrophobic surface where the contact angle is greater than 150˚.

Figure 2.23 shows the nanotube coated surface properties before and after PBA grafting to carbon nanotubes. The droplet on untreated CNTs coated cotton fabric had a hydrophobic state at first, however it absorbed into the surface after 5 minutes. On the other hand, PBA-g-CNT coated cotton fabric kept the hydrophobic state of the droplet for 30 minutes. In other words, the PBA grafting produced an improved superhydrophobic surface via fabrication of nanotubes onto fibers because it provided a stronger affinity between nanotubes and fibers. The carbon nanotube-coated cotton fibers can provide advantages such as the novel mechanical and electrical properties of carbon nanotubes which result in the potential application in various areas including sensing, conducting, self-cleaning and smart textiles. Although more costly, this assembly method is effective in modifying the fiber surface using nano-scale materials as well as carbon nanotubes.

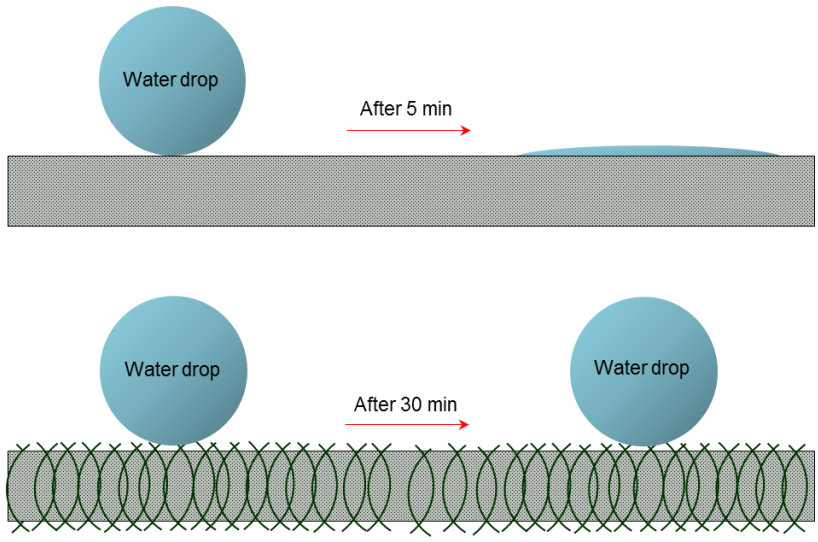

Figure 2. 23. Schematic showing the mechanism for the super-hydrophobic properties of the PBA-g-CNTs coated cotton fabrics: (a) water droplet on untreated cotton fabrics and (b) water droplet on PBA-g-CNTs coated cotton fabrics.

(Image from Ref. 141)

Geometrical approaches of woven fabric (Macroscale)

Protuberances on fiber surfaces are nano- or microscale and can be created by chemical or mechanical methods. In case of a woven fabric, the geometry of a weave structure also enhances roughness on a macroscale. Many studies have shown the effectiveness of enhancing the geometry of a weave structure on fabric properties, such as surface properties, physical properties, and mechanical properties.[53, 59, 60, 143, 144] According to Taylor, weaving itself increases the physical and mechanical strength of woven fabric by creating intersection points of warp and weft yarns, which hold the yarns stable in the stretching directions and allows two

yarns to share the applied load. Fibers have a stronger binding effect because of the inter-fiber pressure which is derived by interlacing warp and weft yarns; it becomes stronger if the float length is short: i.e. plain weave structure. Yarn twist also plays a role into increasing the fabric strength via binding the fibers.[60]

However, compared to the number of studies of the effectiveness of geometric structure on the physical or mechanical strength, research verifying the relationship between the geometry of woven structure and wetting behavior has not been adequately explored, especially for superhydrophobicity, superoleophobicity, or liquid repellent surfaces. Hasan[51] used plain and twill structures of polyester fabrics woven with microfilaments to determine the influence of geometrical structures on wetting behavior by observing the penetration of water. According to the study, yarn density, fineness, and weave patterns are important construction parameters to determine waviness of the fabric surface. In a plain structure, the waviness and porosity are decreased as the yarn density is increased, which results in longer absorption time of water into the structure. Twill structures show a different wetting behavior because their porosity is increased at a high yarn density, which is attributed to the high waviness of twill structures. The yarn density affects the water penetration for plain and twill structures differently. Plain is a more effective structure to prevent water absorption at high density, while the twill surface allows water to penetrate more easily due to the larger porosity.

The spreading rate of a water droplet on the surface of plain woven fabric is also decreased at the low fabric density. This was attributed to the increase of waviness in a plain weave structure.[51] Air in the weave structure can maximize the liquid penetration time by developing an interfacial line between the air and liquid where the air leads to a high contact angle for liquid. This indicates that the fabric density increases or decreases the void space, which affects the penetration and spreading rate of liquid on woven fabric surfaces. Further study is required to define the most effective fabric density to minimize the penetration and spreading of liquid on the face of a woven fabric surface.

Hassan's study contributed the explanation of the impact of woven structures and cross-sectional shapes of fibers, however, it still has a limitation in explaining the geometrical influence of weave structures on enhancing liquid wetting behavior. For that, a consideration of the geometry of woven structures should be followed in a further study to define the most effective woven structure and its geometry to obtain the well-performing liquid repellent surface of woven fabric.

2.3. Geometrical models of woven structures

2.3.1. Fundamental geometrical models of woven fabric from a cylindrical yarn to a distorted yarn

Geometrical structures of woven fabrics have been studied by several researchers to define the relationship between the woven structures and physical or mechanical properties.[53, 54, 56, 143, 145] The studies show that the fabric properties are strongly dependent on the construction of a fabric as well as the properties of fiber and yarn.

Geometrical models of fabrics are composed of geometrical parameters to ascribe geometrical values, such as distance between yarns, diameter of yarn, and crimp.[53] The geometrical models allow prediction of the performance of woven structures, and provide guidance to enhance the properties of real fabrics, especially to achieve a liquid repellent surface for oil. The geometrical models of woven structures were first developed by Peirce (1937).[53] The Peirce[53] geometry incorporated several assumptions to simplify the model: the yarns are cylindrical shapes, inextensible, and completely flexible. Also, pressure was not taken into account in the Peirce model, however, later studies showed that pressure can strongly influence the fabric geometry. The pressure occurring between warp and weft yarns during weaving a fabric leads to a change of the cross-section profile of warp and weft yarns by flattening them. [53, 54, 56, 143, 145] Figure 2.24 shows the geometrical model of plain structure which is characterized by eleven parameters:

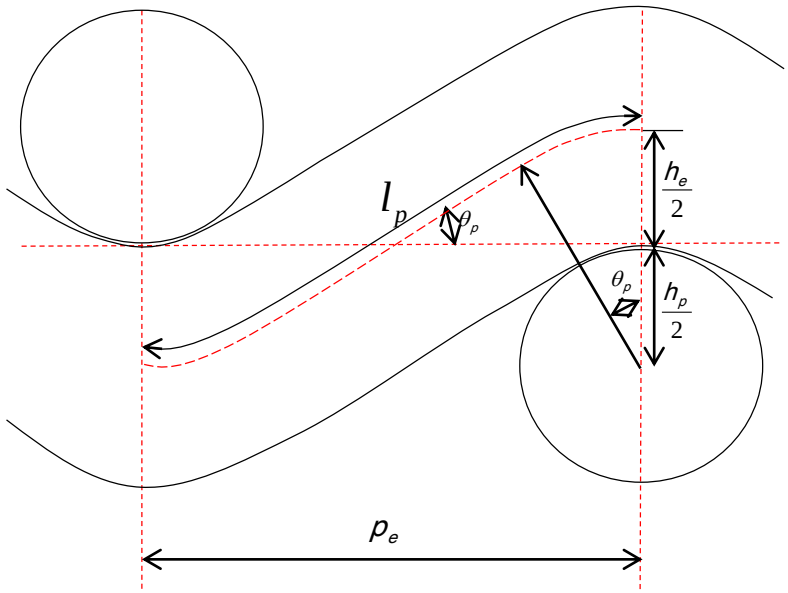

Figure 2. 24. Peirce's geometrical model of a plain woven fabric.

(Image from Ref. 53)

Crimp ratio, *c*, yarn diameter of the warp or weft yarns, 2*R*, heights of the warp or weft yarns, *h*, thread spacing between adjacent warp or weft yarns, *p*, the modular length of the warp or weft yarns, *l*, and the weaving angle of warp or weft yarns, θ. For the model of a plain structure by Peirce, the eight basic equations are derived in the following equations, where subscripts '*e*' and '*p*' in the variables refer to warp (ends) and weft (picks) yarn, respectively. In Eq. 2.46,[53] *D* is the sum of diameters of warp and weft yarns.

$$D = 2\left(R_e + R_p\right) \tag{2. 46}$$

where, $2R_e$ and $2R_p$ is the diameter of warp and weft yarns. D, is equal to the total thickness of the fabric, h_e and h_p as shown in Eq. 2.47: [53]

$$D = h_e + h_p \tag{2. 47}$$

The crimp ratio of the warp yarn is expressed as a fraction of the modular length of warp yarn, l_e, over the thread spacing between adjacent weft yarns, p_p (Eq. 2.52) and similarly for the weft yarn;[53] the fraction shows how much warp yarn is crimped to the projected line between two weft yarns.

$$c_e = \frac{l_e}{p_p} - 1 \tag{2. 48}$$

In Eq. 2.49,[53] p_p is the threading spacing ratio between adjacent weft yarn, which is characterized by the weaving angle, θ_e, and modular length of warp yarn, l_e, and the sum of the diameter of adjacent warp and weft yarns, D, and similarly for P_e.

$$p_p = \left(l_e - D\theta_e\right)\cos\theta_e + D\sin\theta_e \tag{2. 49}$$

where $D\theta_e$ means the partial circumference of a circle with a radius, R, which is proportional to the weaving angle, θ_e. The calculation follows from the law of cosines and sines.

The height of weft yarn, h_p and warp yarn, h_e, are determined from the crimp ratio of interlacing weft (warp) yarn; it is calculated by using the law of cosines and sines as follows:[53]

$$h_p = \left(l_p - D\theta_p\right)\sin\theta_p + D\left(1 - \cos\theta_p\right) \tag{2. 50}$$

The modular length of the warp yarn is the sum of the thread spacing length between adjacent weft yarns and the additive length being proportional to the crimp ratio of warp yarn; which is derived by Eq. 2.51:[53]

$$l_e = p_p(1+c_e) \tag{2. 51}$$

The modular length, l, is also obtained by following the cosines and tangent for the thread spacing length, p, and total diameter of warp and weft yarns, D (Eq. 2.52):[53]

$$l_p = \frac{p_e}{\cos\theta_p} - D\tan\theta_p + D\theta_p \tag{2. 52}$$

Equation 2.49 can be expressed as a function of θ_e as shown in Eq. 2.53:[53]

$$f\left(\theta_e\right) = \left(l_e - D\theta_e\right)\cos\theta_e + D\sin\theta_e - p_p = 0 \tag{2. 53}$$

Equation 2.53 can be expressed as a function of θ_p:[53]

$$f\left(\theta_p\right) = p_e\sin\theta_p - h_p\cos\theta_p - D\left(1-\cos\theta_p\right) = 0 \tag{2. 54}$$

Peirce's geometrical model of woven fabrics can be used to predict the physical or mechanical properties of the fabric structures. However, the simplest assumption in Peirce's model restricts the accurate prediction of the geometrical woven structure. In reality, the actual yarns are affected by the pressure generated on the warp and weft yarns during the weaving process, which causes the deformation of the cross-section profile of warp and weft yarns.[53, 143] Therefore, yarns under pressure cannot sustain their circular cross-sectional shape.

Because of the limitation of Peirce's model, other researchers extended his model to consider the pressure between warp and weft yarns. Kawabata et al.[57, 58, 146, 147] described the change of thickness of the cross-section of warp and weft yarns under lateral compressive pressure which is caused by the compression of two yarns that occurs while being interlaced with each other. They also examined the deformation of a twill weave structure and permanent deformation regions, which affects the tensile properties.[57] Kawabata's study indicated that the compressed geometrical weave structure model should be developed to simulate and predict the properties of woven fabric related to the wetting behavior to develop a liquid repellent surface. Kemp[54] proposed the racetrack shape cross-section for plain woven fabric, in which the cross-section was extended by two parallel lines between the half circles as shown in Fig. 2.25.

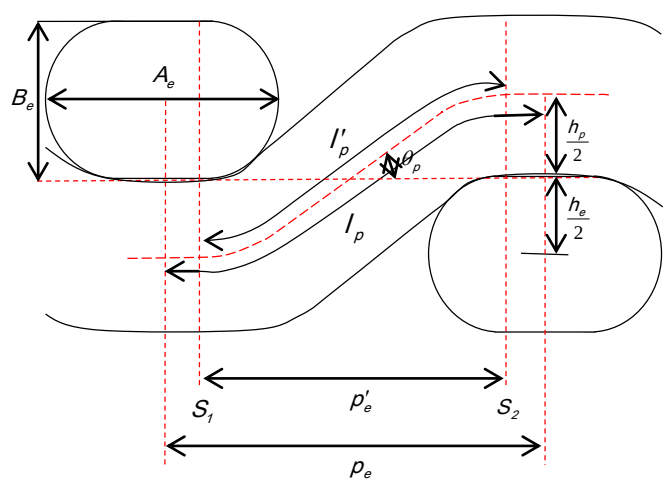

Figure 2. 25. Kemp's geometrical model of the racetrack cross-section for a plain fabric.

(Image from Ref. 54)

In Kemp's model,[54] A and B are the width and height of the cross-section of warp or weft yarn, p' is the distance between S_1 and S_2, l' is the length of the path between S_1 and S_2, and c' is the crimp of the warp or weft between S_1 and S_2. The other parameters have the same definition as Peirce's parameters. Two half circles placed on the plane S_1 and S_2 follow the cross-section within Peirce's model of plain woven fabric. Kemp's model introduces new equations for the parameters of p', l', and c' as follows; the subscripts 'e' and 'p' refer to warp and weft yarns, respectively. p'_e is the thread spacing length between adjacent warp yarns in the range of S_1 and S_2; it is obtained by removing the extended flat length in a width direction between the center of the circular cross-section in Peirce's model as shown in Eq. 2.55:[54]

$$p'_e = p_e - (A_e - B_e) \tag{2. 55}$$

where, p_e is the thread spacing length from center to center between adjacent warp yarns. A_e is the width of racetrack cross-section of warp yarn; B_e is the height of racetrack cross-section of warp yarn. Results are similar for p'_p.[54]

In Eq. 2.56,[54] l'_e is the modular length of warp yarn between S_1 and S_2; it is obtained by removing the flat length extended in the perpendicular to a longitudinal direction. Similar results are obtained for l'_p.

$$l'_e = l_e - (A_p - B_p) \tag{2. 56}$$

In Eq. 2.57,[54] c'_e is the crimp ratio of warp yarn within the range of S_1 and S_2; it refers to the fraction of the extended length of a warp yarn due to waviness over the projected thread spacing

length, p'_p; the waviness is caused by interweaving of weft yarn and warp yarn between adjacent warp yarns and weft yarns.

$$c'_e = \frac{l'_e - p'_p}{p'_p} = \frac{c_e p_p}{p_p - (A_p - B_p)} \tag{2. 57}$$

where the length of the waved warp yarn can be expressed by l'_e and p'_p; which is re-written again using the parameters of c_e, p_p, A_p, and B_p.

The race-track model by Kemp et al.[54] extended the geometrical model of a woven structure in terms of the deformation of yarns under tension while the warp and weft yarns are interlaced. However, the racetrack shape is not sufficient to simulate the actual deformed shape of yarns in terms of a mechanical model; Shanahan and Hearle[56] emphasized the flattening of the curvature, which leads to a decrease in bending energy. On the other hand, the bending energy increased with the racetrack geometry due to the semicircular ends of the curvature of the yarn cross-section. Therefore, Shanahan and Hearle[56] extended Peirce's plain woven model to a lenticular cross-section geometry, for which two identical arcs have been joined under the pressure between warp and weft yarns as shown in Fig. 2.26.

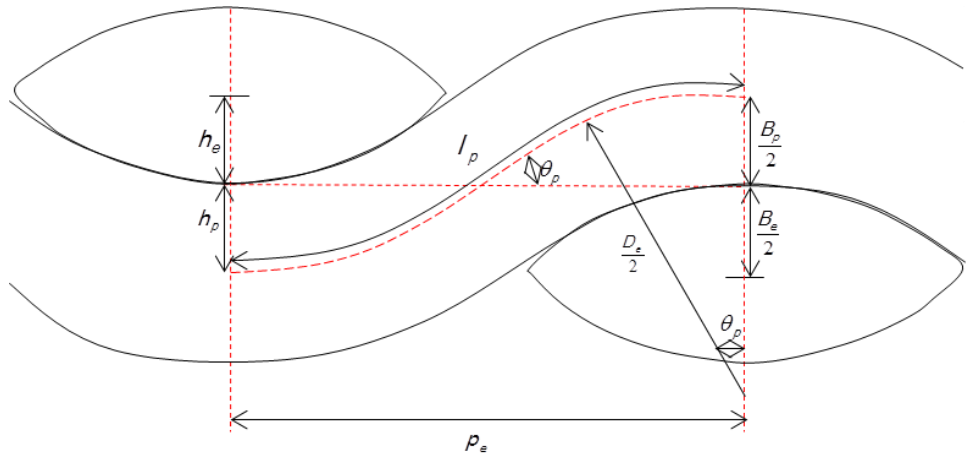

Figure 2. 26. Shanahan and Hearle's model of lenticular yarn cross-section for plain woven fabric. (Image from Ref. 102)

Shanahan and Hearle's geometrical model can be defined by seven parameters in an unit plain structure: B_p, B_e, h_e, h_p, D_e, p_e, and θ_p. In Shanahan and Hearle's model, the total height of adjacent warp and weft yarns is re-written by the crimp height, B_e and B_p, as given by:[56]

$$h_e + h_p = B_e + B_p \tag{2. 58}$$

where, the sum of heights, h_e and h_p, is equal to the total crimp height of the warp and weft yarns, B_e and B_p. D_e and D_p are introduced in the lenticular model, which is characterized by the radius of lenticular arcs, R_e and R_p, and the crimp height, B_p and B_e as given in Eq. 2.59 and Eq. 2.60:[56]

$$D_e = 2R_e + B_p \tag{2. 59}$$

$$D_p = 2R_p + B_e \tag{2. 60}$$

The line defined by D_e or D_p is drawn at the weaving angle, θ_p or θ_e in the centerline; it is specified as the radius of the circumference in the partial modular length at the weaving angle. The circumference at the weaving angle is used to calculate the thread spacing length, p_e and p_p as shown in Eq. 2.61 and Eq. 2.62:[56]

$$p_e = \left(l_p - D_p\theta_p\right)\cos\theta_p + D_p \sin\theta_p \tag{2. 61}$$

$$p_p = \left(l_e - D_e\theta_e\right)\cos\theta_e + D_e \sin\theta_e \tag{2. 62}$$

where, p is the thread spacing length between adjacent warp or weft yarns; it is specified by l, D and θ, and calculated by following the law of cosines and sines.

In Eq. 2.63 and Eq. 2.64,[56, 102] h is the height of the warp or weft yarn from the parallel center line drawn at the middle point of the modular length, l, which is calculated by using the variables l, D, and θ and the law of cosines and sines.

$$h_e = \left(l_e - D_e\theta_e\right)\sin\theta_e + D_e\left(1 - \sin\theta_e\right) \tag{2. 63}$$

$$h_p = \left(l_p - D_p\theta_p\right)\sin\theta_p + D_p\left(1 - \cos\theta_p\right) \tag{2. 64}$$

The fundamental geometrical models of woven structures have been developed continuously from an ideal circular cross-section model to a much more realistic model; i.e. lenticular cross-section model, to predict the fabric behavior related to its physical or mechanical properties. Peirce's model has also been used as a basic model to design a geometrical surface structure of woven fabrics for superhydro- or superoleophobicity; for which the Cassie-Baxter model

was extended to include Peirce's plain woven model; the Cassie-Baxter model is converted from fiber to fabric structures.

Prediction of yarn diameter and fabric thickness

The yarn diameter, 2*R*, is calculated by the yarn tex, *T*, fiber packing factor, *Φ*, and fiber density, *ρ*, as given by Eq.2.65:[62, 148]

$$2R_{cm} = \frac{\sqrt{T}}{280.2\sqrt{\phi\rho_f}} \tag{2. 65}$$

In the basic geometrical models of weave structures, the thickness of fabric, *H*, of warp and weft yarns is:[148]

$$H_e = h_e + 2R_e \tag{2. 66}$$

$$H_p = h_p + 2R_p \tag{2. 67}$$

If the thickness of warp and weft yarns is different, the thicker one is chosen for the fabric thickness; it applies to yarns with a flattened cross-section. If the thickness of the warp and weft yarns is the same, the fabric surface will be smooth and perform uniformly, and in this case, the fabric obtains the minimum thickness as given by:[148]

$$H_{\min} = \frac{1}{2}\left(h_e + 2R_e + h_p + 2R_p\right) \tag{2. 68}$$

here, $h_e = H_{\min} - 2R_e$

If the fine yarn is stretched in the fabric composed of fine and coarse yarns in the warp and weft direction, the coarse yarn will obtain the maximum crimp attributing the increase of thickness. Equation is:[148]

$$H_{\max} = D_{\min\_fine} + 2R_{coarse} \quad \text{if, } h_{coarse} = D_{\min\_fine} \tag{2. 69}$$

where, D is the minimum thickness of fine yarns. The thickness of fabric leads to the prediction of the flattening degree of the racetrack cross-section and lenticular cross-section.

Prediction of weavability via calculating cover factor

Woven fabric cover factor is the area covered with warp or weft yarn relative to the total fabric area, which is calculated by utilizing the geometrical parameters depicted in the geometrical model of weave structures. It is an important indicator to confirm the weavability under fabric weaving conditions, such as picks per inch and ends per inch; the picks per inch refers to how many filling (weft) yarns are interlaced within one inch, and the ends per inch means the number of warp yarns interlaced within one inch, which determines the density of woven structure. The cover factor is calculated by using the parameters of d and p; d is the diameter of yarns and p is the yarn spacing between the adjacent warp or weft yarn as described in Fig. 2.27.

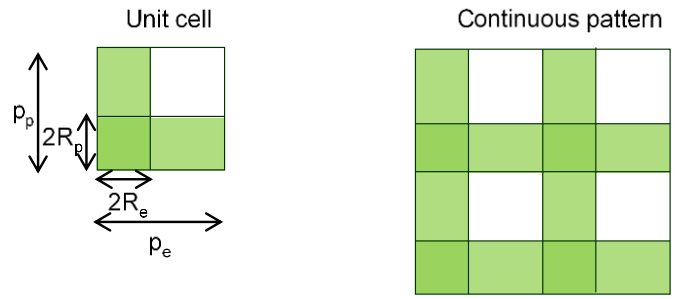

Figure 2. 27. Flat view of plain structures of unit cell and continuous pattern.

Figure 2.27 is a flat view of a plain weave structure. The area covered with warp and weft yarns is given by:[148]

$$C_e = \frac{Area\ Covered\ by\ \text{Warp}\ yarns}{Total\ fabric\ Area} = \frac{2R_e \cdot p_p}{p_e \cdot p_p} = \frac{2R_e}{p_e} \tag{2. 70}$$

$$C_e = \frac{Area\ Covered\ by\ \text{Weft}\ yarns}{Total\ fabric\ Area} = \frac{2R_p \cdot p_e}{p_p \cdot p_e} = \frac{2R_p}{p_p} \tag{2. 71}$$

since the fabric is covered with warp and weft yarns, the covered area of fabric, C_F, is:[148]

$$C_F = \frac{Area\ Covered\ by\ Warp\ and\ \text{Weft}\ yarns}{Total\ fabric\ Area} = \frac{2R_e \cdot p_p + 2R_p \cdot p_e - 2R_e \cdot 2R_p}{p_e \cdot p_p} \tag{2. 72}$$

where, subscript, *F*, refers to fabric, and the duplicate area of warp and weft yarns is removed. The equation is also expressed in terms of *C*:[148]

$$C_F = C_e + C_p - C_e \cdot C_p \tag{2. 73}$$

where, the subscripts *F*, *e*, and *p* refer to fabric, warp yarn, and weft yarn, respectively. Equation 2.65 can be rewritten in a function of the yarn spacing, *p*, for the fraction of fabric covered by warp or weft yarns as shown below:[148]

$$2R_{cm} = \frac{\sqrt{T}}{280.2\sqrt{\phi\rho_f}}$$

$$\frac{2R}{p} = \frac{E\sqrt{T}}{280.2\sqrt{\phi\rho_f}} = \frac{K}{28.02\sqrt{\phi\rho_f}} = \frac{K}{28\sqrt{\phi\rho_f}} \tag{2. 74}$$

$$\text{if, } E = \frac{1}{p}, K = E\sqrt{T} \times 10^{-1}$$

where, E is the number of ends (warp) or picks (weft) per cm. The cover factor, K, is characterized by E and T (tex). The cover factor, K, for the warp yarn, the weft yarn is given by:[148]

$$K_F = 28\left(C_e + C_p - C_e \cdot C_p\right)$$

$$= 28\left(\frac{2R_e}{p_e} + \frac{2R_p}{p_p} - \frac{2R_e \cdot 2R_p}{p_e \cdot p_p}\right)$$

$$= 28\frac{2R_e}{p_e} + 28\frac{2R_p}{p_p} - 28 \times \frac{28}{28}\frac{2R_e \cdot 2R_p}{p_e \cdot p_p}$$

$$= K_e + K_p - \frac{K_e \cdot K_p}{28} \tag{2. 75}$$

where,

$$K_F = 28C_F$$

$$K_e = 28C_e = 28\left(\frac{2R_e}{p_e}\right)$$

$$K_p = 28C_p = 28\left(\frac{2R_p}{p_p}\right)$$

If the cover factor, K, of warp and weft yarns lies within the range of Maximum Weavability in Peirce's graph[53] in Fig. 2.28, the fabric can be woven.[53]

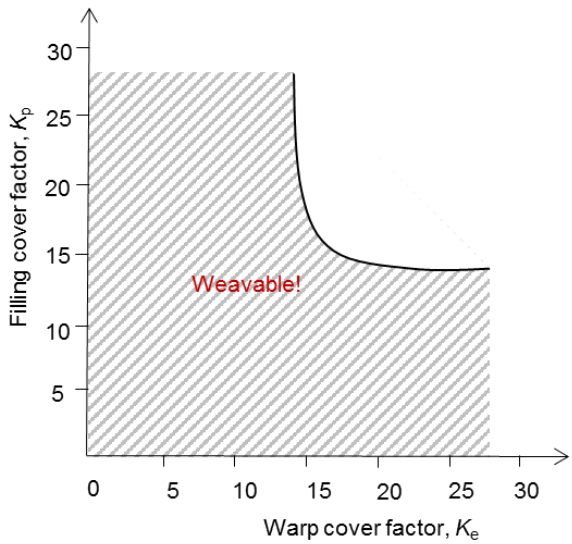

Figure 2. 28. Peirce's graph of Maximum Weavability

The graphical method by Peirce is a method to define the weavability of woven conditions. However, the weavability cannot be defined without the characterized number of the yarn diameter, *d*, and the yarn spacing, *p*. Therefore, the analytical method needs to be considered to predict the cover factor, *K*, which number can be proven in Peirce's Maximum Weavability as shown in Fig. 2.28. Equation 2.76 describes the relationship of cover factor, *K*, and yarn balance, β; the plain structure is considered for the cover factor, *K*, and β is characterized by the ratio of weft yarn diameter to warp yarn diameter. The conditions of *K* and β could be utilized to weave fabrics if the left side of the equation is less than one.[99]

$$\sqrt{1-\left(\frac{28}{(1+\beta)K_e}\right)^2}+\sqrt{1-\left(\frac{28\beta}{(1+\beta)K_p}\right)^2}<1 \qquad (2.\ 76)$$

where, $\beta=\frac{R_p}{R_e}$

2.3.2. Extension of fundamental models to Cassie-Baxter model for a superhydrophobic or superoleophobic surface from fibers to fabrics

A geometrical model of fiber, yarn, and fabric structures is extended from the Cassie-Baxter model expressed in Eq. 2.22 and Eq. 2.23. Lee et al.[45, 50] developed the geometrical modeling of single filament fiber, multi filament fibers, and also three woven structures; 1/1 plain, 2/1 twill, and 3/1 satin. The following several steps of equations shows the modeling result studied for fiber and yarn by Lee et al. and Michielsen et al.[45, 50, 52, 112] For monofilament fibers, it has been supposed that two filament fibers are parallel on a solid substrate as shown in Fig. 2.29.

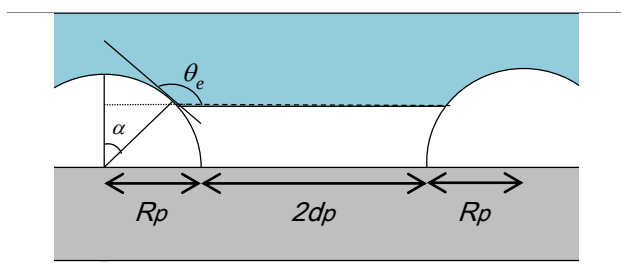

Figure 2. 29. Liquid droplet on two filament fibers.

(Image from Ref. 52)

The apparent contact angle of the fibers, $\theta_{r_f}^{CB}$, was created as shown in Eq. 2.77. f and r_f were characterized by the radius of fibers, R, a distance between two fibers, D (=2d), and α was also replaced with $\pi - \theta_e$ (Eq. 2.22, Eq. 2.23). It has been assumed that the surface free energy is minimum.[45, 50, 52, 112]

$$\cos\theta_r^{CB} = \frac{R_p(\pi - \theta_e)}{d_p + R_p}\cos\theta_e + \frac{R_p}{d_p + R_p}\sin\theta_e - 1 \tag{2. 77}$$

$$r_f = \frac{R_p\alpha}{R_p \sin\alpha} = \frac{\pi - \theta_e}{\sin\theta_e} \tag{2. 78}$$

$$\text{if}, \alpha = \pi - \theta_e$$

$$f = \frac{R_p \sin\theta_e}{R_p + d_p} \tag{2. 79}$$

In Eq. 2.78, r_f is a roughness ratio of the curved surface over a projected contact area for a liquid droplet on the fibers surface; f is a fraction of the projected contact area of the droplet over a distance from center-to-center of the two fibers. For a unit area, the center-to-center distance can be expressed by R+d. $r_f f$ is the roughness ratio to the fraction of the projected area in contact with the liquid droplet, and 1-f is the void space distance between two fibers, which is the composite interface of the air and liquid. α is the angle between the top of the cylinder and the liquid contact line.

From the two-dimensional geometrical structure of the filament fiber, Lee et al.[45] proposed a geometrical structure of a plain woven fabric constructed of two types of yarns; one was a

cylindrical monofilament yarn, and the other was a cylindrical multifilament yarn. The geometrical structures for cylindrical yarns are ideal when the external and internal pressures applied to the warp or weft yarn during the weaving process are ignored. The pressures can cause a distortion of the warp and weft yarns.

The study used the cross sections of woven structures as shown in Fig. 2.30.[45, 50, 52] For warp and weft yarns, each radius in a vertical direction is 2*R*, and the length from the center of the warp or weft yarn to the center of adjacent warp or weft yarns is 4*R*. The bottom length from the center of a warp yarn to the center of a weft yarn can be defined as $2\sqrt{3}R$ by the Pythagorean Theorem.

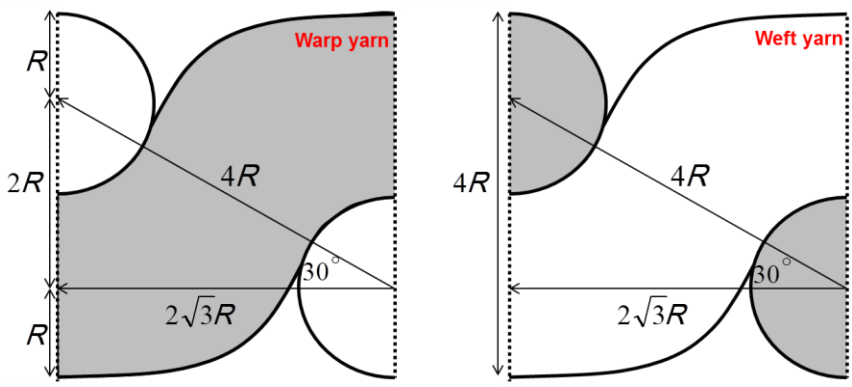

Figure 2. 30. Cross section views of a plain woven structure with cylindrical yarns.

(Image from Ref. 45 and 52)

The length of the vector from the center of a weft (or warp yarn) to the center of an adjacent warp (or weft yarn) can be expressed using *R* and *d* as shown:[45, 50]

$$2\left(R+d\right)=2\sqrt{3}R \tag{2. 80}$$

$$\cos\theta_r^{CB}=\frac{1}{\sqrt{3}}(\pi-\theta_e)\cos\theta_e+\frac{1}{\sqrt{3}}\sin\theta_e-1 \tag{2. 81}$$

The apparent contact angle of a liquid droplet is calculated in a plain woven structure using Eq. 2.81. The Young contact angle, θ_e, is replaced by the apparent contact angle obtained from protuberances on the surface of the fibers. Figure 2.30 shows the case when two monofilament warp or weft yarns are placed in a parallel direction. This model considered a liquid droplet sitting on the top surface of two parallel monofilament wrap or weft yarns.[45] However, this model did not consider the real structure of woven fabric and the behavior of a liquid droplet sitting on top of the actual woven fabric surface.

Therefore, a new model is needed to explain the real deposition of a liquid droplet onto a woven fabric. If a liquid droplet contacts the top of a solid surface, it will penetrate into the woven structure, and stop when the contact angle of the liquid with the warp or weft yarns reaches the Young contact angle. However, if the solid surface is modified for superhydrophobicity and superoleophobicity through a chemical or physical treatment, the liquid-vapor interface line will stop at a higher point. The interface line at a higher point of the geometrical structure will decrease the contact area between the liquid and solid, and it will lead to a higher contact angle. If the contact angle reaches over 150° for superhydro- or superoleophobicity, which is

accompanied by a smaller contact area, the liquid droplet rolls off easily as shown in the Lotus effect. The properties of the liquid and the solid are also critical factors to determine the Young contact angles of the droplet placed on a woven fabric surface.

2.4 Summary

For woven fabrics, the non-wetting performance is enhanced through a multi-level approach considering the composite of fibers, yarns, and weaving structures; the types of fibers strongly influence the determination of yarn properties, and the types of yarns affect the fabric properties. Moreover a specific weave structure maximizes the functionality of the woven fabric for a specific end use. The composite performance of woven fabric is obtained from the weave construction. Therefore, to enhance the performance of woven fabric, the properties of fiber and yarn should be considered within the weave structures.

The type of weave structure plays a critical role in establishing the unique geometrical structure for each weave type. Chemical treatment is an effective way to improve the fiber properties through the surface modification of fibers; the low surface energy and specific morphological structure are achieved in the fiber level. These structures were inspired by biomaterials exhibiting superhydrophobicity and the self-cleaning effect, such as the lotus leaf; and this bio-mimicry assists the fabric surface to reach superhydrophobicity and self-cleaning. The morphological modification especially introduces void spaces beneath a liquid droplet, which

is a dominant factor to enhance the phobic surface by creating a liquid-vapor composite region supporting the liquid.

Since oily liquids have lower surface tensions, the existence of void spaces and the composite interfacial region are much more critical in obtaining superoleophobicity. Multiscale structures have been recommended by many researchers to reduce the contact area of liquid and to increase the void space to support an oil droplet. The composite structure of microscale and nanoscale protuberances prevents the transition of Wenzel and Cassie-Baxter states by enhancing the energy barrier of the liquid-vapor interfacial region.

On the macroscale, the weave structure also contributes to the development of roughness and void space to support the interfacial region and minimize the transition of wetting state from the Cassie-Baxter state with higher energy to the Wenzel state with lower energy. The designing of the geometry of a woven fabric is a potentially significant way to maximize the geometrical effect to achieve a liquid repellent surface, even for oil with low surface tension.

The geometric models of different weave structures have been studied to compare the effect on the apparent contact angle of a liquid droplet on a woven fabric surface. The idealized geometrical models of weave structures assist in defining the relationship of parameters used in the schematic for a plain structure. For the consideration of yarn compression under tension, the racetrack cross-section geometry model and lenticular cross-section geometry model

followed the circular cross-section geometry model of Peirce. It suggests that the compressed cross-section will support the development of a liquid repellent surface based on more realistic yarn behavior.

Chapter 3 Experimental

3.1 Materials

Through a market review, commonly used woven fabric structures have been defined for the outermost layer of jackets and pants in high performance clothing. The woven structures include plain, 2/1 twill, and basket. The plain is a representative structure having good physical and mechanical properties. The 2/2 basket is used for fabrics requiring extreme strength.

Preparation of fabric samples

Based on the commonly used woven structures identified in the market review, fabric samples have been manufactured in the facilities of the College of Textiles, NCSU and have also been collected through the retail market of woven fabrics. The laboratory designed woven fabrics were produced utilizing a hand weaving loom, AVL COMPU-DOBBY IV. The hand weaving loom provided 16 harnesses for a plain woven structure, which has been selected as the highest performing structure from the theoretical prediction and the measurement of the liquid wetting behavior. To spread the warp yarns out regularly following the designed fabric density (ends per inch, picks per inch), the stainless steel reeds at 39 or 40 dents per inch were utilized. The void space has been varied through varying the pick level, thus reducing the maximum fabric density.

Preparation of smooth surface and rough surface multifilament yarns

For hand weaving, the multifilament nylon yarn was provided by Premiere Fibers, Inc. The yarn consists of 34 filaments; 200 denier and 0.018 cm yarn diameter. The rough surface yarn is an artificial duck feather yarn produced in a laboratory of CoT (College of Textiles), NCSU. On the surface of smooth surface multifilament yarn, bell-shape protuberances were engineered to modify the smooth surface yarn to the artificial duck feather yarn. The limited amount of the artificial duck feather yarn produced prohibited the use of industrial weaving equipment, also it was fragile to bear the high tension of the industrial machine. For these reasons, a hand weaving machine (AVL Dobby Loom) was utilized to weave the Laboratory designed woven fabric samples. For the weft yarn, the smooth surface yarn and the rough surface yarn were used for each fabric sample to examine the effect of micro-scale structures created in the multifilament yarn on liquid resistance against a fabric surface.

3.2 Cleansing of materials

Before chemical treatment, all fabrics were cleaned by immersing them in isopropyl alcohol for at least an hour at room temperature to remove contamination on the fabric surfaces.

3.3 Chemical treatment for achieving low surface tension

1H,1H,2H,2H-Heptadecafluoro-trimethoxysilane (FS, $C_{13}H_{13}O_3F_{17}Si$, Gelest INC., Morrisville, PA) and ammonium hydroxide (NH_4OH, Sigma-Aldrich, St. Louis, MO) were dissolved in isopropyl alcohol (VWR, West Chester, PA) to make a FS solution. The weight

ratio of fabric, FS, ammonium hydroxide, and isopropyl alcohol was in the order of 1: 1.4: 0.2: 20 respectively. The fabrics were immersed in isopropyl alcohol to pre-wet them and padded to remove excess liquid. The pre-wetted fabrics were immersed in the FS solution overnight. Then, the fabrics were padded and cured in a microwave oven (Panasonic NN-SD967S, Osaka, Japan) at 150℃ for 2 minutes. The cured fabrics were rinsed two times in isopropyl alcohol and dried in a microwave oven at 120℃ for 3 minutes.

3.4 Characterization

3.4.1 Contact angle measurement

The fabric contact angle is measured by using a lab-designed goniometer at room temperature. The dodecane (γ_{LV} = 25.3 mN/m) was dropped on the woven fabric surface. The droplet volume was 10 μℓ. The image of liquid droplets was obtained from a digital camera (Canon, EOS EF-S-18-55IS, Lake Success, NY, USA), attached to an optical stereomicroscope (Meiji Techno, EMZ-13TR, Saitama, Japan).

3.4.2 Geometric structure observation

Scanning electron microscopy (SEM, JEOL, 6400F, Tokyo, Japan) images were used to observe the structural geometries of yarns: smooth surface yarn and artificial duck feather yarn, and fabrics: collected commercial fabrics, NCSU manufactured fabrics, and Laboratory designed woven fabrics.

3.4.3 Fiber radius measurement

The radius of smooth surface fiber was measured using a Mitutoya MDS-1" MJ digimatic micrometer (Mitutoya USA, Aurora, IL). At least five fibers were randomly selected from the multifilament nylon yarns (Premiere Fibers, Inc). The diameter was directly read from the micrometer when the micrometer tips touched the fiber placed between the tips.

3.4.4 Yarn diameter prediction

The diameters ($2R$) of smooth surface yarn and rough surface yarn were predicted using the characteristics of the nylon yarn and fibers. The characteristics include the fiber density, ρ_f (g/cm^3), the fiber packing coefficient, ϕ, and the linear density of yarn, N_{d} (g/9km) or N_{tex} (g/km).

3.4.5 Statistical analysis

The statistical analysis was conducted using bivariate and Two-way Anova (SPSS Statistics 22) to identify the correlation of the measured contact angle with the woven fabric's geometrical parameters: e.g. yarn flattening, and size of void space.

Chapter 4 Results and Discussion

4.1 Development of woven fabrics' geometrical models

Through a market review, commonly used woven fabric structures have been defined for the outermost layer of jackets and pants in high performance clothing. The most prevalent structures include plain, 2/1 twill, and basket weaves.

4.1.1 Geometrical models of circular yarn

Liquid deposition on plain woven fabric surface of circular cross-section yarn

In examining liquid deposition, it is essential to understand the droplet's wetting behavior on a woven fabric structure. Figure 4.1 shows the geometry of a plain structure, assuming that the yarn is completely circular. The geometrical parameters are defined by Pythagoras' theorem for the length, $2R$, and the vector angle, 30°. The liquid droplet is deposited on top of the plain structure surface. It assumes that the geometry of the top surface creates two different arcs with the radius, R, and another radius, $3R$. Each arc is drawn at the angle α relative to a vertical line. The angle, α, is determined by the liquid surface tension and the local structure of the solid surface. Thus the same liquid will have the same angle, α.

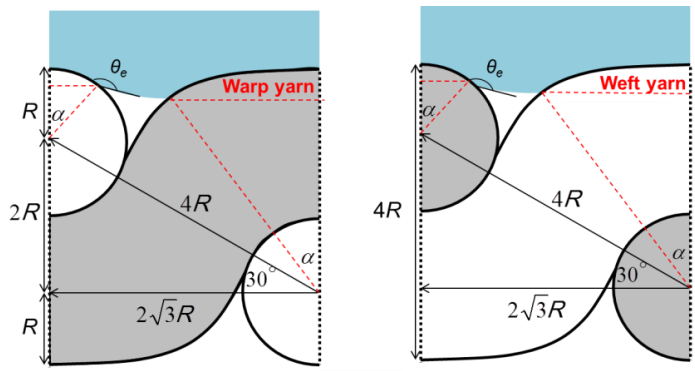

Figure 4. 1 Liquid deposition on plain woven structure surface of circular cross-section yarn.

Extension of the Cassie-Baxter model into selected woven structures of circular yarn

The plain weave is a representative basic woven fabric structure. The structural geometry of the plain weave is idealized by the circular cross-sectional yarn and defined by the Pythagorean Theorem. The structural geometries of 2/1 twill and 2/2 basket weaves present the extended surface length by R and $2R$ respectively in following the definition of each structure. The change of the geometries influences the determination of the contact area of a liquid on each woven fabric surface as shown in Fig. 4.2.

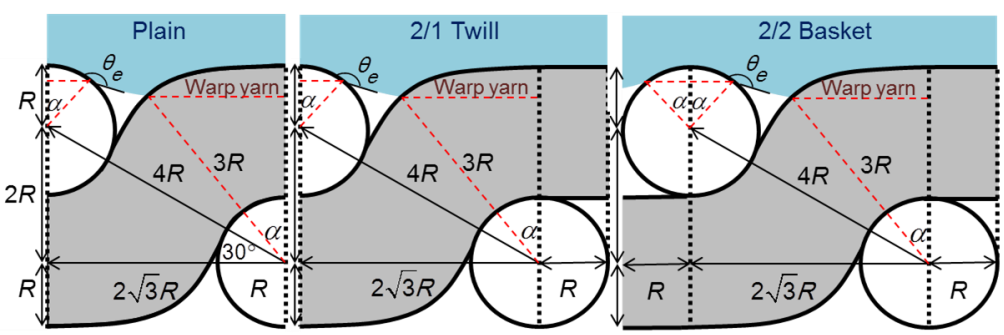

Figure 4. 2 Geometries and liquid depositions in different woven fabric structures.

Each woven structure generates different roughness qualities, derived from the different surface geometry. How the liquid deposits on each surface is critical to develop the Cassie-Baxter equations for the woven structures. In a plain weave, the two arcs created by the radius, *R* and 3*R*, become the contact line of a liquid on the top surface of the plain structure. 2/1 Twill weave has the extension by *R* in the right direction: the top surface of the 2/2 basket weave is extended by *R* in the right and left directions. The equations can be used to predict the liquid wetting behavior in a solid structure. The difference in the wetting behavior is caused by the liquid contact area to the solid surface, $r_f f$, and the liquid contact area to the air in the groove, f-1, as described in Eq. 4.1:

$$\cos\theta_r^{CB} = r_f \ f \ \cos\theta_e + f - 1 \tag{4. 1}$$

f is a fraction of the projected area of the rough surface wet by a liquid and r_f is a roughness ratio of the wet area. According to the geometrical definition in Fig. 4.2, the Cassie-Baxter equations for each woven fabric structure are directly derived by the Pythagorean Theorem. The Cassie-Baxter equation of the plain woven structure is:

$$\cos\theta_{r_{F\_plain}}^{CB} = \frac{2(\pi-\theta_e)}{\sqrt{3}}\cos\theta_e + \frac{2\sin\theta_e}{\sqrt{3}} - 1 \quad for \ \ \alpha = \pi - \theta_e \tag{4. 2}$$

In consideration of the extended surface area by *R*, the Cassie-Baxter equation of the 2/1 twill structure is expressed as:

$$\cos\theta_{r_{F\_2/1twill}}^{CB} = \frac{4(\pi-\theta_e)+1}{2\sqrt{3}+1}\cos\theta_e + \frac{4\sin\theta_e+1}{2\sqrt{3}+1} - 1 \quad for \ \ \alpha = \pi - \theta_e \tag{4. 3}$$

By extending the surface areas by *R* in the right and left directions, the Cassie-Baxter equation of the 2/2 basket structure is given by:

$$\cos\theta^{CB}_{r_{F\_2/2Basket}} = \frac{5(\pi-\theta_e)+1}{2\sqrt{3}+2}\cos\theta_e + \frac{5\sin(\pi-\theta_e)+1}{2\sqrt{3}+2} - 1 \quad for \;\; \alpha = \pi - \theta_e \tag{4. 4}$$

The Cassie-Baxter equation for the plain woven structure reflected the way that the liquid droplet sits on the woven fabric surface. This proves the limitation in the Cassie-Baxter model developed by Lee et al.[45] This model[45] did not take into account the full structural geometry of the plain weave and the deposition of a liquid droplet on the plain woven fabric surface. Thus, it led to an incorrect derivation of the Cassie-Baxter equation for the plain weave. On the other hand, the final equation for the 2/1 twill woven structure is in agreement with that by Lee et al.[50] This approach provides a consistent concept of the liquid contact area on the surfaces of woven fabrics, from which the modeling of woven structures can be developed, and results in a consistent concept of the fabric.

4.1.2 Geometrical models of lenticular yarn using *e*

Yarn compression

The Cassie-Baxter models of woven structures studied in Fig. 4.2 made the assumption that the warp and weft yarns are completely circular. However, the real yarn shape in woven fabrics is compressed from a circular shape to a lenticular shape when warp and weft yarns interlace, which causes tension between the warp and weft yarns. As the tension increases, the yarns are much more flattened.

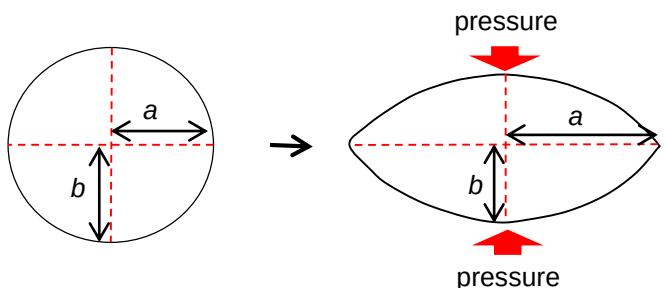

(a) Circular cross-section (a=b) (b) Lenticular cross-section (a > b)

Figure 4. 3 Change of yarn cross-section in vertical and horizontal directions.

Figure 4.3 shows the change of the yarn cross-section in the vertical and horizontal directions caused by yarn flattening under tension. The yarn has two axes in the yarn cross-section; '*a*' is a major axis, and '*b*' is a minor axis. The yarn flattening is expressed by the flattening factor, *e*, as shown in Eq. 4.5:

$$e = \sqrt{\frac{b}{a}} \leftrightarrow b = ae^2 \tag{4. 5}$$

The flattening factor is characterized by the major axis and the minor axis. The relationship between the two different axes is used to derive the Cassie-Baxter equations of the selected woven sample with consideration for the yarn flattening. The structures include plain, 2/1 twill, and 2/2 basket weaves.

Assuming that all fibers within a yarn are in parallel to each other in the completely flattened yarn, the range of the major axis, *a*, and the minor axis, *b*, will be defined by the fiber diameter, d_f, and the number of fibers, N_f, as seen below:

$$2b \geq d_f \tag{4. 6}$$

$$2a \leq d_f \times N_f \tag{4. 7}$$

If the fiber surface is developed by regularly distributed protuberances with the same size, 2*a* is redefined by the height of protuberance, h_p, fiber diameter, d_f, and number of fibers, N_f, in the completely flattened yarn as following:

$$N_f\left(d_f + h_p\right) + h_p \leq 2a \leq N_f\left(d_f + 2h_p\right) \tag{4. 8}$$

In Fig. 4.4, the blue dashed curve refers to the change of the yarn flattening factor, *e*, by the decrease or increase of the major axis, *a*. Another curve (red) obtained by 1-*e* represents the amount of the yarn flattening by the change of the major axis, *a*. The yarn flattening increases steeply first, and then increases more gradually.

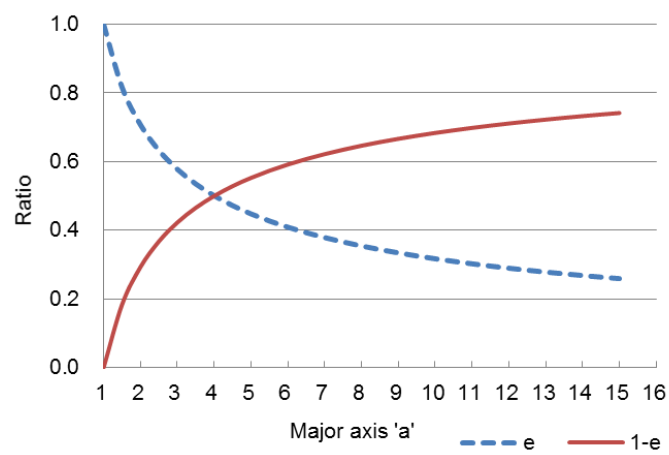

Figure 4. 4 Changes of flattening factor, *e*, and increase of flattening, 1-*e*, upon an increase of the major axis, *a*.

The Cassie-Baxter equation expressed using 'e' will provide the apparent contact angle on the compressed yarns' surface of the woven fabrics. The apparent contact angles of the fabrics represent the liquid wetting behavior upon the structural geometries of fabrics. The impact of the yarn flattening on the liquid wetting behavior will be presented by predicting the liquid's apparent contact angle on the geometrically modeled woven fabric surface of the lenticular cross-section yarn.

Extension of lenticular yarn's Cassie-Baxter model by e

The Shanahan and Hearle model is a representative geometry of the plain structure for the lenticular cross-section of yarn. To extend this model to the Cassie-Baxter model, the major and minor axes are rewritten as a and b as shown in Fig. 4.5. The other parameters are the same as the Shanahan and Hearle model. To predict the liquid contact area for the flattened yarn surface, the following assumptions are used:

- The geometries of the flattened warp and weft yarns are the same and symmetrical.
- When yarn is flattened, the major axis, a, increases while the minor axis, b, decreases: the yarn flattening factor, e, is defined as $\sqrt{b/a}$, $0 < b/a \leq 1$.
- In the lenticular model developed using the flattening factor, e, and the void space ratio, T.
- In yarn flattening, an arc with radius, R, is generated in a warp or weft yarn: R is defined using a and b by the Pythagorean Theorem.
- The flattened yarns have arcs of radii R and $R+2b$.

- The liquid contact area is determined by Young's contact angle, θ_e, in a woven structure constructed of monofilament yarns. If a woven fabric is constructed of multifilament yarns, θ_e will be replaced by the yarn contact angle, θ_y. Both contact angles depend on the liquid properties and the local structure of the solid.
- The yarn spacing, *P*, is defined by the major axis, a, and the other projected area characterized by the Pythagorean Theorem.

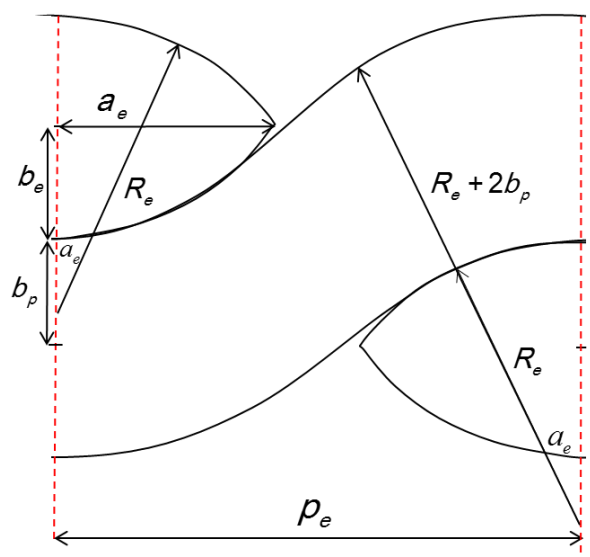

Figure 4. 5 Plain woven structural geometry using lenticular cross-section yarn.

Based on the geometrical assumptions and definitions, the yarn spacing, *P*, is:

$$P_e^2 = 4b_p\left(2R_e + b_p\right)$$
$$\text{when, } R = \frac{a^2 + b^2}{2b} \tag{4. 9}$$

Since the geometries of the warp and weft yarns are the same and symmetrical, the geometrical parameters *P*, *R*, *a*, and *b* can be used without the suffix as *e* for the warp yarn and *p* for the weft yarn. When *P* is rewritten in terms of the flattening factor, *e*, it becomes:

$$P = 2a\sqrt{1+2e^4} \tag{4. 10}$$

The newly defined yarn spacing, *P*, will be utilized to derive the Cassie-Baxter equation of selected woven structures: plain, 2/1 twill, and 2/2 basket weaves.

Cassie-Baxter equation of plain structure expressed by e in the lenticular yarn model

The fractions $r_f f$ (= f_1) and f (f_2 = 1-f) should be redefined using the parameters of *a*, *b*, and *e* to derive the Cassie-Baxter equation of woven structures with the lenticular cross-section yarn model. The fraction of the liquid contact area to the projected distance between two adjacent warp or weft yarns, *rf*, is expressed by those geometrical parameters and θ_e in Eq. 4.11:

$$rf = \frac{R\alpha + \left(R+2b\right)\alpha}{P} = \frac{\left(1+3e^4\right)\left(\pi - \theta_e\right)}{2e^2\sqrt{1+2e^4}}$$
$$for,\ \alpha = \pi - \theta_e \tag{4. 11}$$

The fraction of the projected liquid contact area to the projected distance between two adjacent warp or weft yarns, *f*, is:

$$f = \frac{R\sin\alpha + (R+2b)\sin\alpha}{P} = \frac{(1+3e^4)\sin\theta_e}{2e^2\sqrt{1+2e^4}} \tag{4. 12}$$

By the definition of r_f f and f-1, the Cassie-Baxter equation for a plain woven structure is expressed as:

$$\cos\theta^{CB}_{r_{F\_plain}} = \frac{(1+3e^4)(\pi-\theta_e)}{2e^2\sqrt{1+2e^4}}\cos\theta_e + \frac{(1+3e^4)\sin\theta_e}{2e^2\sqrt{1+2e^4}} - 1 \tag{4. 13}$$

where, $\alpha = \pi - \theta_e$, $0 < e \le 1$

The plain woven structure has the most interlacements of warp and weft yarns and the largest amount of void space in a unit area. In a unit structure of a plain weave, the ratio of the void space between adjacent warp or weft yarns over the liquid contact area would be higher than the one in the other structures. Therefore, this plain woven structural geometry is expected to show better fabric wetting resistance to a liquid than the other woven structures.

Cassie-Baxter equation of 2/1 twill structure expressed by e in lenticular yarn model

In a 2/1 twill structure, a weft yarn floats over two adjacent warp yarns. Therefore, the distance between adjacent warp or weft yarns, *P*, is extended by the major axis, *a*, as shown in Fig 4.6.

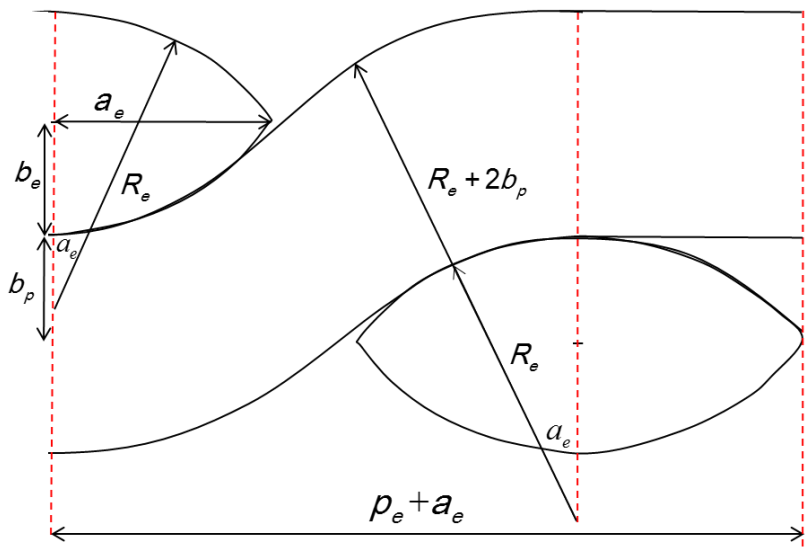

Figure 4. 6 2/1 twill woven structural geometry using lenticular cross-section yarn.

The fractions, *rf* and *f*, are rewritten by the extended axis, *a*, in either the left or right direction of weft yarn as given by:

$$rf = \frac{R\alpha + (R+2b)\alpha + a}{P+a} = \frac{(1+3e^4)(\pi-\theta_e)+e^2}{e^2\left(1+2\sqrt{1+2e^4}\right)} \tag{4. 14}$$

$$f = \frac{R\sin\alpha + (R+2b)\sin\alpha + a}{P+a} = \frac{(1+3e^4)\sin\theta_e + e^2}{e^2\left(1+2\sqrt{1+2e^4}\right)} \tag{4. 15}$$

In the same way as the plain woven structure, the Cassie-Baxter equation for the 2/1 twill woven structure is formulated by the definition of $r_f f$ and f-1as:

$$\cos\theta^{CB}_{r_{F\_2/1Twill}} = \frac{(1+3e^4)(\pi-\theta_e)+e^2}{e^2\left(1+2\sqrt{1+2e^4}\right)}\cos\theta_e + \frac{(1+3e^4)\sin\theta_e + e^2}{e^2\left(1+2\sqrt{1+2e^4}\right)} - 1 \tag{4. 16}$$

This 2/1 twill structure has an extension of weft yarn in either the right or left direction in a unit structure. This extension will increase the ratio of the liquid contact area to the void space since there is no change of the void space in the geometrical models developed for these selected woven fabric structures. The larger liquid contact area is supposed to decrease the fabrics' wetting resistance.

Cassie-Baxter equation of 2/2 basket structure expressed by e in lenticular yarn model

A basket woven structure is an extension of a plain structure in the direction of warp and weft yarns. The 2/2 basket woven structure floats the warp and weft yarns over two weft and warp yarns, respectively, as drawn in Fig. 4.7.

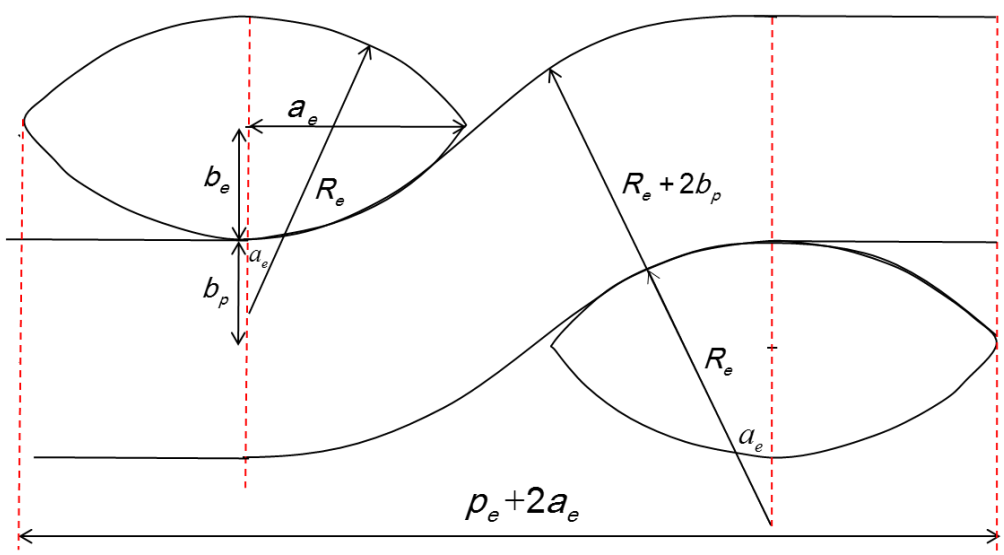

Figure 4. 7 2/2 basket woven structural geometry using lenticular cross-section yarn.

The 2/2 basket woven structure is characterized by the extension of warp and weft yarns by the length of the major axis, 2*a*. The fraction of *rf* and *f* is re-expressed for the extended length by 2*a* as shown below:

$$rf = \frac{2R\alpha + (R+2b)\alpha + a}{P+2a} = \frac{(3+7e^4)(\pi-\theta_e)+2e^2}{4e^2\left(1+\sqrt{1+2e^4}\right)} \tag{4. 17}$$

$$f = \frac{2R\sin\alpha + (R+2b)\sin\alpha + a}{P+2a} = \frac{(3+7e^4)\sin(\pi-\theta_e)+2e^2}{4e^2\left(1+\sqrt{1+2e^4}\right)} \tag{4. 18}$$

By the definition of $r_f f$ and f-1, the Cassie-Baxter equation of the 2/2 basket woven structure is rewritten as following:

$$\cos\theta^{CB}_{r_{F\_2/2\,Basket}} = \frac{(3+7e^4)(\pi-\theta_e)+2e^2}{4e^2\left(1+\sqrt{1+2e^4}\right)}\cos\theta_e + \frac{(3+7e^4)\sin(\pi-\theta_e)+2e^2}{4e^2\left(1+\sqrt{1+2e^4}\right)} - 1 \tag{4. 19}$$

In the 2/2 basket woven fabric, two weft or warp yarns float over two warp or weft yarns. The longer float length creates the larger liquid contact area. Therefore, the 2/2 basket woven fabric is expected to show the weaker liquid resistance against the surface than the plain woven structure due to the larger liquid contact area on the surface. On the other hand, the roughness of the 2/2 basket woven structure would be higher than the 2/1 twill woven structure. In the 2/1 twill weave, the weft yarn floats over two warp yarns and then crosses under one warp yarn, creating unique diagonal lines in the *S* or *Z* direction. The diagonal ridgeline of the weave becomes a channel that directs the dragging of the liquid when sliding off the surface. This dragging is supposed to impede the roll-off of a liquid droplet on a woven fabric surface.

4.1.3 Geometrical models of lenticular yarn using *e* and *T*

Prediction of maximum cover factor

Fabric structure plays an important role in determining the amount of void space and the impact of void space on the liquid behavior. In wovens, the cover factor is the area covered with warp or weft yarn to the total fabric area, which varies by ends or picks per unit length of the woven structure. More ends or picks per length leads to a higher cover factor value. It also results in higher fabric density. The void space between yarns depends on the fabric density; the lower fabric density has a larger void space in a unit structure. In addition, the cover factor is an indicator of the weavability with regards to the fabric density. If the maximum cover factor is specified in the range of weavability for a given yarn diameter, the fabric density is characterized by the ends or picks per unit length. Based on the maximum fabric density, the ends or picks per unit length can vary the amount of void space between adjacent warp or weft yarns. The different amount of void space will change its impact on the liquid behavior. The cover factor is characterized by the parameters of d and p; d is the diameter of yarns and p is the yarn spacing between the adjacent warp or weft yarns as described in Fig. 4.8.

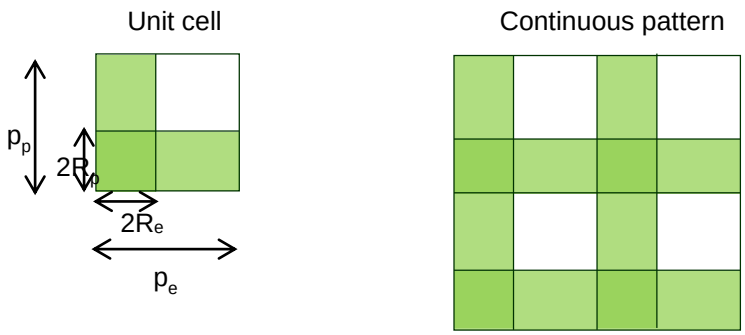

Figure 4. 8 Unit cell and continuous pattern of plain structure.

If the cover factors of warp and weft yarns are verified by using the yarn diameter, *d*, and the yarn spacing, *p*, the weavability could be defined for these cover factors through the graphical method of Peirce. However, without knowing those geometrical characteristics of the yarn, the maximum cover factor, *K*, could be predicted through the use of the analytical method for defining weavability. When accommodating the analytical method with identification of the cover factor, *K*, it is assumed that the size of warp and weft yarn would be the same.

In the analytical method, Equation 4.20 describes the relationship of *K* and the yarn balance, β; *K* considers the closest plain structure and β is characterized by the ratio of weft yarn diameter to warp yarn diameter. The structure will be able to be woven if the left side equation is less than one.[99] To predict the maximum *K*, it is assumed that the yarn diameter of warp and weft yarn is the same and the interlacement of warp and weft yarns is completely balanced with the same number of ends and picks per unit length. With these assumption, Equation 4.20 can be expressed by:

$$\sqrt{1-\left(\frac{28}{(1+\beta)K_e}\right)^2}+\sqrt{1-\left(\frac{28\beta}{(1+\beta)K_p}\right)^2}<1$$

$$if, \beta=\frac{R_p}{R_e}=1 \quad (R_p=R_e), K_e=K_p$$

$$\sqrt{1-\left(\frac{14}{K}\right)^2}+\sqrt{1-\left(\frac{14}{K}\right)^2}<1 \tag{4. 20}$$

$$\sqrt{1-\left(\frac{14}{K}\right)^2}<\frac{1}{2}$$

$$16.166>K$$

$$K_{\max}=16$$

where, the subscripts of *e* and *p* refer to warp and weft yarn, respectively. When the interlacement of warp and weft yarns is balanced with the same number of yarns in a unit length, the cover factor for warp and weft yarns will be the same. Therefore, the subscripts, *e* and *p* are eliminated in the expression for *K*. The equation characterized by *K* is revised in Eq. 4.20. In the end, *K* has to be less than 16.2 to satisfy the weavability of the fabric structure, then the largest cover factor is 16 for both the warp and weft yarns, as given by Peirce's Maximum Weavability graph shown in Fig. 4.9.[53]

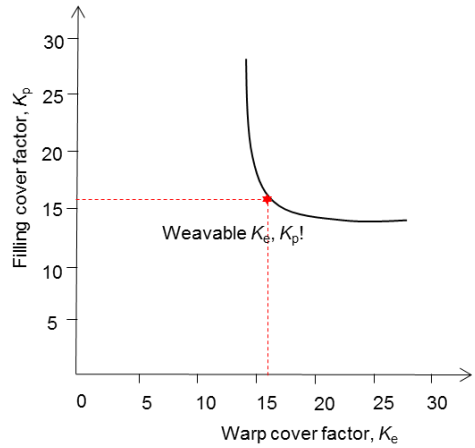

Figure 4. 9 Verification of maximum weavability using Peirce's graph.

Identification of fabric density using the predicted maximum cover factor, K=16

For the determination of the real yarn diameter, nylon fibers were used to depict the geometry of yarn formation with 37 total fibers in the first through the fourth layers. The fiber diameter and the yarn linear density (denier) are presented in Table 4.1.

Table 4. 1 Characteristic of multifilament nylon yarn

Layers (N)	Number of fibers (n)	N_d (g/9km)	$2R_f$ (cm)
4	37	157.5	0.0026

The properties of the nylon fiber and yarn are shown in Table 4.2 for the fiber density and the fiber packing coefficient. The fiber packing coefficient varies by the amount of twist; non-

twisted, normal twist, and hard twist. Based on the information in Table 4.1 and Table 4.2,[62, 86] the yarn diameter was calculated using Eq. 2.4 and Eq. 2.6 as shown in Table 4.3.

Table 4. 2 Properties of nylon fiber and yarn

ρ_f (g/cm^3)	ϕ		
	non-twisted	normal twist	hard twist
1.14	0.25	0.6	0.9

Table 4. 3 Calculation of yarn diameter

	Equation 2.4	Equation 2.6		
		non-twisted	normal twist	hard twist
$2R_y$ (cm)	0.0182	0.0280	0.0180	0.0147

With the maximum cover factor and the yarn diameter, the yarn spacing, *p*, is calculated using Eq. 2.75. The maximum ends or picks per unit length were obtained by the inverse relationship of the fabric density to the yarn spacing. The distance between two adjacent warp or weft yarns is given by p-2R_y; it is the void space between yarns in the woven structure. The ratio of void space to the yarn diameter is expressed as *T* in Table 4.4. If the yarn diameter and the fabric density are the same for a plain weave, the distance between two adjacent warp or weft yarns is equivalent, leading to the same void space in the warp or weft direction. Then, the void space ratio to the yarn diameter, *T*, will be same in the both directions. The number in Table 4.4

represents the geometrical parameters in a woven structure for the warp and weft yarns when the cover factor is equal to the maximum cover factor K_{max} = 16.

Table 4. 4 Characteristic of geometrical parameters in woven structure

K_{max}	$2R_y$ (cm)	p (cm)	p-2R_y (cm)	T	1/p (ends or picks per cm)
16	0.0182	0.0319	0.0137	0.75	31.4

Variation of fabric density

The fabric density determines the void space. The void space increases as the fabric density decreases. The ratio of the fabric density compared to the maximum fabric density (T=0.75, K=16) was reduced by 5% from 1 to 0.5 as shown in Table 4.5.

Table 4. 5 Change of void space ratio at varied fabric density

W_{fd}	K	T
1.00	16.0	0.75
0.95	15.2	0.84
0.90	14.4	0.95
0.85	13.6	1.06
0.80	12.8	1.19
0.75	12.0	1.34
0.70	11.2	1.50
0.65	10.4	1.69
0.60	9.6	1.92
0.55	8.8	2.18
0.50	8.0	2.50

Extension of Cassie-Baxter model using T

The fabric density ratio (W_{fd}) is the ratio of fabric density to the maximum fabric density, therefore, W_{fd} equals 1 when K=16. The cover factor, K, and the void space ratio, T, also vary by changing W_{fd}.

In the previous study, the Cassie-Baxter model was expressed using the flattening factor, e, to consider the yarn compression that occurs when interlacing warp and weft yarns to construct a woven structure. However, only using e in the Cassie-Baxter model is limited in describing the impact of void space on the liquid behavior. Therefore, the ratio of void space to yarn diameter, T, is applied in extending the Cassie-Baxter model below.

The center-to-center distance of adjacent yarn, P, defined in Fig. 4.8 is re-expressed by the ratio of void space to the yarn diameter, T as:

$$\begin{aligned} P &= 2R_y + 2\mathrm{R}_y\left(\frac{p - 2\mathrm{R}_y}{2R_y}\right) \\ &= 2R_y + 2R_y \times T \\ &for,\ T \geq 0.75 \end{aligned} \tag{4. 21}$$

where, a is a yarn radius, and p is the warp or weft yarn spacing. If the yarn diameter, d_y, is equal to twice the major axis, 2a, the equation can be rewritten as:

$$\begin{aligned} P &= 2a + 2a \times T \\ &= 2a(1+T) \end{aligned} \tag{4. 22}$$

The value of P represents the projected area of two adjacent warp or weft yarns. P, reformulated using T, will be utilized for deriving the Cassie-Baxter equation of the selected

woven structures. These equations also include the flattening factor, *e*. Therefore, the newly developed Cassie-Baxter equations with *e* and *T* will be able to predict the impact of the yarn flattening and the void space on the liquid resistance of the woven fabrics.

Cassie-Baxter equation of plain structure expressed by T in the lenticular yarn model

For the plain woven structure in the lenticular cross-section model as shown in Fig. 4.5, the fraction of the liquid contact area to the projected area between two warp or weft yarns, *rf*, is:

$$rf = \frac{R\alpha + (R+2b)\alpha}{P} = \frac{(1+3e^4)(\pi - \theta_e)}{2e^2(1+T)} \tag{4. 23}$$

where, *D* is the diameter of the new circle due to flattening, *a* is the length of the major axis, *b* is the length of the minor axis, *e* is the flattening factor, and α is the angle of the liquid contact area. Likewise, the fraction of projected liquid contact area to the projected area between two warp or weft yarns, *f*, is:

$$f = \frac{R\sin\alpha + (R+2b)\sin\alpha}{P} = \frac{(1+3e^4)\sin\theta_e}{2e^2(1+T)} \tag{4. 24}$$

Two fractions of *rf* and *f* characterize the Cassie-Baxter equation given by:

$$\cos\theta^{CB}_{r_{F\_plain}} = \frac{(1+3e^4)(\pi - \theta_e)}{2e^2(1+T)}\cos\theta_e + \frac{(1+3e^4)\sin\theta_e}{2e^2(1+T)} - 1 \tag{4. 25}$$

$$if,\ \alpha = \pi - \theta_e,\ T \geq 0.75,\ 0 < e \leq 1$$

Cassie-Baxter equation of 2/1 twill structure expressed using T in lenticular yarn model

The 2/1 twill woven structure has one weft yarn floating over two warp yarns, therefore, the center-to-center distance of two adjacent warp or weft yarns, *P*, is extended by the yarn radius, *a*, as shown in Fig. 4.6. The added yarn radius increases the contact area of liquid on a surface of woven structure.

For the 2/1 twill woven structure in the lenticular cross-section model, the fraction of liquid contact area to the projected distance between two warp or weft yarns, *rf*, can be expressed using *T*:

$$rf = \frac{R\alpha + (R+2b)\alpha + a}{P+a} = \frac{(1+3e^4)(\pi - \theta_e) + e^2}{e^2(3+2T)} \tag{4. 26}$$

The fraction of projected area of liquid contact area to the projected area between two warp or weft yarns, *f*, is given by:

$$f = \frac{R\sin\alpha + (R+2b)\sin\alpha + a}{P+a} = \frac{(1+3e^4)\sin\theta_e + e^2}{e^2(3+2T)} \tag{4. 27}$$

The Cassie-Baxter equation is obtained:

$$\cos\theta^{CB}_{r_{F\_2/1Twill}} = \frac{(1+3e^4)(\pi - \theta_e) + e^2}{e^2(3+2T)}\cos\theta_e + \frac{(1+3e^4)\sin\theta_e + e^2}{e^2(3+2T)} - 1 \tag{4. 28}$$

$$for,\ \alpha = \pi - \theta_e,\ T \geq 0.75,\ 0 < e \leq 1$$

Cassie-Baxter equation of 2/2 basket structure expressed using T in lenticular yarn model

The 2/2 basket woven structure is extended in the warp and weft directions by floating the warp and weft yarns over two weft and warp yarns. The geometry of a 2/2 basket woven structure is shown in Fig. 4.7 for the lenticular cross-section of yarn.

The 2/2 basket woven structure is characterized by the extension of warp and weft yarns by the yarn diameter, 2*a*. The fraction of the contact area of liquid to the distance between two warp or weft yarns, *rf*, is then expressed by the extended length, 2*a*, as shown below:

$$rf = \frac{2R\alpha + (R+2b)\alpha + a}{P+2a} = \frac{(3+7e^4)(\pi - \theta_e) + 2e^2}{4e^2(2+T)} \tag{4. 29}$$

The fraction of the projected liquid contact area to the projected distance between warp or weft yarns, *f*, is given by:

$$f = \frac{2R\sin\alpha + (R+2b)\sin\alpha + a}{P+2a} = \frac{(3+7e^4)\sin(\pi - \theta_e) + 2e^2}{4e^2(2+T)} \tag{4. 30}$$

The Cassie-Baxter equation of the 2/2 basket structure is expressed by:

$$\cos\theta^{CB}_{r_{F\_2/2\,Basket}} = \frac{(3+7e^4)(\pi - \theta_e) + 2e^2}{4e^2(2+T)}\cos\theta_e + \frac{(3+7e^4)\sin(\pi - \theta_e) + 2e^2}{4e^2(2+T)} - 1 \tag{4. 31}$$

$$for,\ \alpha = \pi - \theta_e,\ T \geq 0.75,\ 0 < e \leq 1$$

The derived Cassie-Baxter equations for the plain, 2/1 twill, and 2/2 basket woven structures considers the void space via *T*. The ratio can be varied with the different amount of void space between yarns; as the void space increases, the ratio increases. The void space is determined

by the fabric density specified by the ends or picks per unit length. The fabric density is characterized by the cover factor, K, and the yarn diameter, $2a$ ($=d_y$); the maximum cover factor in the range of weavability leads to the maximum fabric density for a given yarn diameter. It means that the void space minimizes the maximum fabric density through the tightly packed warp or weft yarns in the unit length. Therefore, the void space between yarns increases through loosely packing the warp or weft yarns from the maximum fabric density, which leads to a lower number of ends or picks per unit length. On the other hand, the void space decreases by tightly packing the warp or weft yarns up to the maximum fabric density, which leads to a higher number of ends or picks per unit length. It is expected that the larger void space in yarns enhances the liquid resistance of the fabric in respect to supporting a liquid droplet on the surface of the woven structures. The apparent contact angle is a parameter used to predict the liquid resistance of the fabric or the liquid behavior.

4.1.4 Geometry model of multifilament yarn

Researchers have strongly emphasized the void space in a solid structure as a key factor to enhance the oleophobicity of fabric because the surface tension across the air-liquid interface can support a liquid droplet and survive on the solid surface. For woven fabrics, the effect of void space in a multifilament yarn can be considered in improving the fabric performance in oleophobicity. Also, the oleophobic fabric surface can be developed by predicting the impact of different void spaces on change of contact angle and generating protuberances on the fiber surface. Figure 4.10 shows the formation of multifilament yarn and the creation of void space

between the fibers; the amount of void space in a multifilament yarn will increase or decrease by changing the distance between two fibers.

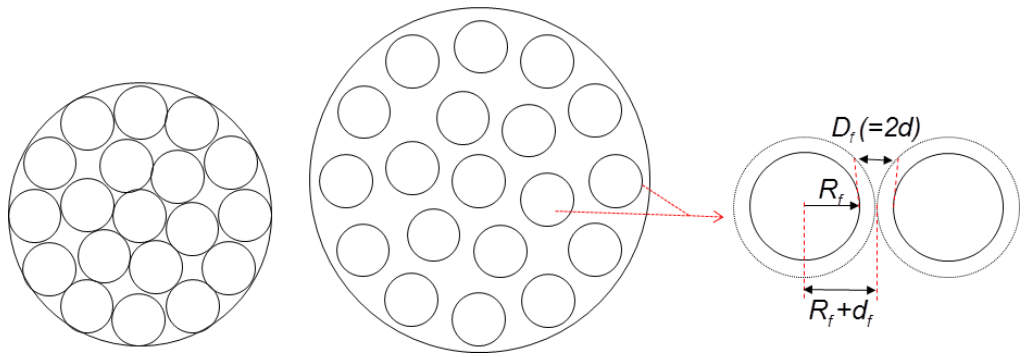

(a) (b) (c)

Figure 4. 10 (a) Tightly packed yarn (b) loosely packed yarn (c) geometry of two fibers with void space between fibers.

For a multifilament yarn, a projected area includes the void space between fibers as shown in Eq. 4.32; which is characterized by a fiber radius, R_f, the distance between two fibers, d_f, and the Young contact angle, θ_e,. The suffix, *f*, refers to fiber.

$$\cos\theta^{CB}_{r_{multifilament-yarn}} = \frac{R_f(\pi-\theta_e)}{R_f+d_f}\cos\theta_e + \frac{R_f}{R_f+d_f}\sin\theta_e - 1 \qquad (4.\ 32)$$
$$if,\ \alpha = \pi - \theta_e$$

where, the distance, d_f, can be expressed by the ratio of d_f to R_f ; which leads to the prediction of contact angle for various ratios of the distance to the fiber radius. Based on Eq. 4.33, it can

be assumed that the higher ratio of d_f to R_f will result in a higher contact angle for a given fiber radius and the Young contact angle.

$$\cos\theta^{CB}_{r_{multifilament-yarn}} = \frac{R_f(\pi-\theta_e)}{R_f+\left(\frac{d_f}{R_f}\right)R_f}\cos\theta_e + \frac{R_f}{R_f+\left(\frac{d_f}{R_f}\right)R_f}\sin\theta_e - 1 \tag{4. 33}$$

Equation 4.33 is simplified to Eq. 4.34:

$$\cos\theta^{CB}_{r_{multifilament-yarn}} = \frac{(\pi-\theta_e)}{1+\frac{d_f}{R_f}}\cos\theta_e + \frac{1}{1+\frac{d_f}{R_f}}\sin\theta_e - 1 \tag{4. 34}$$

$$if,\ \alpha = \pi - \theta_e$$

4.1.5 Geometry model of void space for its size

Sagging phenomenon and its impact on geometry model of void space

The sagging phenomenon is caused by the inside and outside pressure difference of a liquid when the liquid droplet contacts vapor in the rough structure as described in Fig. 2.16. The sagging height, h_1, is varied by the structural geometry and the liquid property. If the liquid is the same, the protuberance height and its distance will play an important role in the liquid penetration into the rough structure. The protuberance height, h_p, impacts the determination of the pore depth, h_2: the protuberance distance, D_p (=$2d_p$), contributes to decreasing or increasing the sagging height, h_1. This indicates that when creating the rough surface, the protuberance

height and the distance between two adjacent protuberances need to be considered in designing the structural geometry for the prevention of the liquid penetration.

Depth of void space in geometry model

The sagging height, h_1, is dependent on the liquid property for a given roughness geometry. The pore depth, h_2, is affected by the protuberance height, h_p, as depicted in Fig. 2.17. Thus, defining the protuberance height, h_p, for a liquid is important for creating the optimum structural geometry of the rough surface. If it is assumed that the liquid-vapor interface line resides below the middle of the protuberance height in the metastable state and h_1 is smaller than h_2 for a given distance, d_p, the protuberance height, h_p, should be higher than two times of the maximum pore depth, h_2, for the small droplet as given by:

$$\begin{aligned} &h_p > 2h_2 \\ &if,\ h_2 > h_1 \end{aligned} \tag{4. 35}$$

For the large droplet, the protuberance's height should be significantly higher than two times that of the maximum pore depth, h_2.

$$\begin{aligned} &h_p >> 2h_2 \\ &if,\ h_2 > h_1 \end{aligned} \tag{4. 36}$$

The geometrical relationship amongst h_1, d_p, and R_{sag} (Fig. 2.17) provides the minimum height of the protuberance preventing the penetration of the liquid droplet into the solid structure.

Maximum size of void space, D

When a liquid droplet is deposited on a rough solid surface, there is a pressure difference across the liquid-vapor interface referred to as the Laplace pressure or the capillary pressure.[125, 130] Due to the pressure difference, the liquid in contact with the vapor generates a curvature with the radius, *R*, as seen in Fig. 2.15 and Fig. 2.16. According to equation 2.26, *R* is determined by the radius of the narrow cylindrical tube, *a*. Equation 2.27 combined with Eq. 2.25 and Eq. 2.26 expresses the pressure difference. Since the capillary pressure reaches the equilibrium state at the capillary height, *h*, in Eq. 2.28, the protuberance height on a rough surface should be higher than the capillary height of the liquid. If the capillary height, *h* (or h_1 in Fig. 2.16), at the equilibrium state equals the pore depth, h_2 (Fig. 2.16), the capillary height, *h* (or h_1), should be reduced by adjusting the distance, *D* (=2*d* in Fig. 2.16), between the two adjacent protuberances (the cylindrical tube radius, 2*a*). For that, Tuteja et al.[38] also defined that h_2 has to be much higher that h_1 to prevent the touch-down of the liquid droplet to the rough surface bottom, leading to the penetraion of the liquid into the soild structure. If the assumption is developed: *h* or h_1=h_2, the relation is provided that the pressure difference for '*a*' (=*d*) needs to be equal or greater than the pressure difference for '*h*' (=h_2) when h_2 equals to *a* or h_1. This relation is expressed in Eq. 4.37 by combining Eq. 2.27 and Eq. 2.28:

$$\frac{2\gamma_{LV}\cos\theta}{a} \geq \rho g h \qquad (4.\ 37)$$

The capillary length, ℓ^2_{cap}, is a characteristic of a liquid determined by the liquid properties γ, ρ, and *g*. Rearranging the equation as in Eq. 4.38, gives ℓ^2_{cap} as defined in Eq. 4.39.

$$\frac{\gamma_{LV}}{pg} \geq \frac{ah}{2\cos\theta} \tag{4. 38}$$

$$\ell_{\text{cap}}^2 \geq \frac{ah}{2\cos\theta} \tag{4. 39}$$

If it is assumed that the value of h over cosine θ is close to 1, Equation 4.40 is simplified as shown in Eq. 4.41:

$$\begin{aligned} &\ell_{\text{cap}}^2 \geq \frac{a}{2} \\ &if,\ \frac{h}{\cos\theta} \approx 1 \\ &\text{here, } \ell_{cap} = \sqrt{\frac{\gamma_{LV}}{pg}} \end{aligned} \tag{4. 40}$$

Since $2a = 2d_{\text{p}} = D$:

$$\begin{aligned} &4\ell_{\text{cap}}^2 \geq D \\ &\text{when, } 2a = 2d_p = D \end{aligned} \tag{4. 41}$$

This final Equation 4.41 indicates that the distance between two protuberances, fibers, or yarns should be limited by $4\ell^2_{\text{cap}}$ to prevent the penetration of the liquid droplet into any solid structure. When a liquid droplet is deposited on top of a solid surface, it creates the liquid-vapor interface. If the distance, D, does not satisfy the predicted range in fiber, yarn, or woven structure, the sagging length of the liquid will exceed the height of the groove created by any protuberance on a solid surface or any yarn interlacement in a woven fabric structure. In the end, the liquid-vapor interface touches down to the bottom of the groove, and it will fill the groove completely. This indicates that the wetting behavior of the liquid is changed from the Cassie-Baxter state to the Wenzel state.

The maximum distance, *D*, is dependent on the type of liquid. Table 4.6 shows the capillary length and the maximum distance for the different liquids. Thus the design of the solid geometry should consider the different maximum distances for the different liquids. In designing a solid structure, the distance, *D*, for each liquid may be engineered to minimize the liquid penetration.

Table 4. 6 Calculation of maximum distance, *D*, between two adjacent protuberances, fibers, or yarns

	γ_{LV} (N/m)	ρ (g/mL)	g (m/s^2)	ℓ_{cap} (cm)	D (cm)
Water	0.07	1.00	9.8	0.27	0.30
Dodecane	0.03	0.75	9.8	0.19	0.14
Methanol	0.02	0.79	9.8	0.17	0.12
Vertrel XF	0.01	1.58	9.8	0.10	0.04

Void space geometry model applied to woven and yarn structural geometry

In the previous section, the height, h_p, and the distance, d_p, have been provided by the geometry of the solid surface with the protuberance. The prediction of h_p and d_p could be applied to the yarn geometry in the woven fabric structural geometry and the fiber geometry in the multifilament yarn's structural geometry. The yarn radius is expressed by *R*, and the distance between the two adjacent yarns by *D*. The subscripts of *e* and *p* refer to the warp yarn and the

weft yarn, respectively. The subscripts are also renamed *y* or *f*, referring to yarn or fiber. The geometrical parameters are compared in Table 4.7.

Table 4. 7 Geometrical parameters for protuberances on a fiber surface and interlacing yarns in a weave structure

	Parameter	
	Yarn in woven structure	Fiber in yarn structure
Height	h_y (=2R_y)	h_f (=2R_f)
Distance	D_y (=2d_y)	D_f (=2d_f)
Sagging height	h_1	h_1
Pore depth	h_2	h_2
Radius of curvature	R_{sag}	R_{sag}

4.2 Prediction of wetting behavior using geometric models

4.2.1 Prediction using geometric model of circular yarn

The results above show that the fabric contact angle becomes larger than 0˚ ($\theta_F > 0$˚) or higher than the applied Young contact angle ($\theta_F < \theta_e$) at specific Young contact angles. For $\theta_F < \theta_e$, the specific Young contact angle was 104˚ for plain and 2/1 twill weave structures, and 102˚ for 2/2 basket weave structure as shown in Fig. 4.14 (b). This is explained by the transition of the droplet state to the Wenzel state ($\theta_F < \theta_e$) or the Cassie-Baxter state ($\theta_F > \theta_e$) at the defined Young contact angle for each structure: plain, 2/1 twill, and 2/2 basket. Those defined Young contact angles are limited for smooth solid surfaces. The Young contact angle can be replaced with a fiber or yarn contact angle when fiber or yarn structure impacts on improving the fabric contact angle. This emphasizes that a multiscale structure needs to be developed by creating nano or micro scale roughness in a fiber or yarn to enhance the liquid resistance. The solid surface energy should be lower than the liquid surface tension.

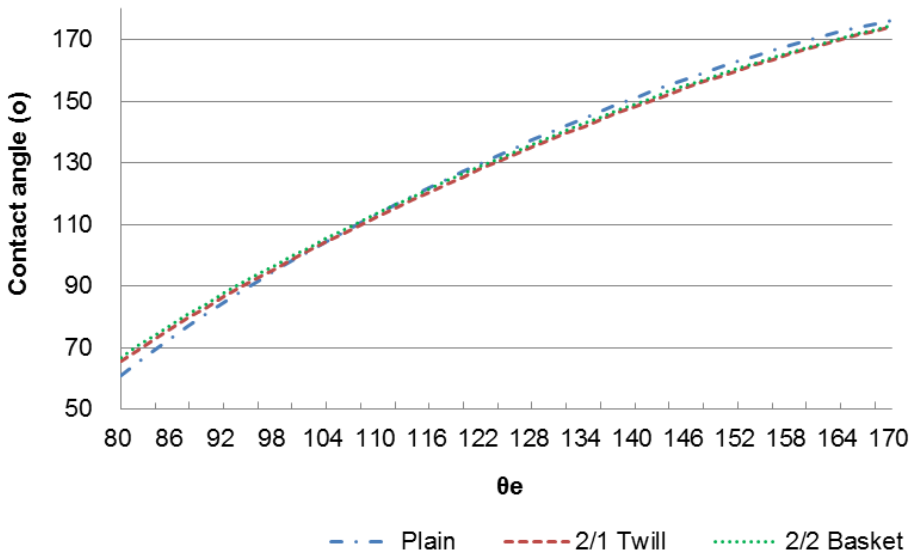

(a) Predicted contact angle

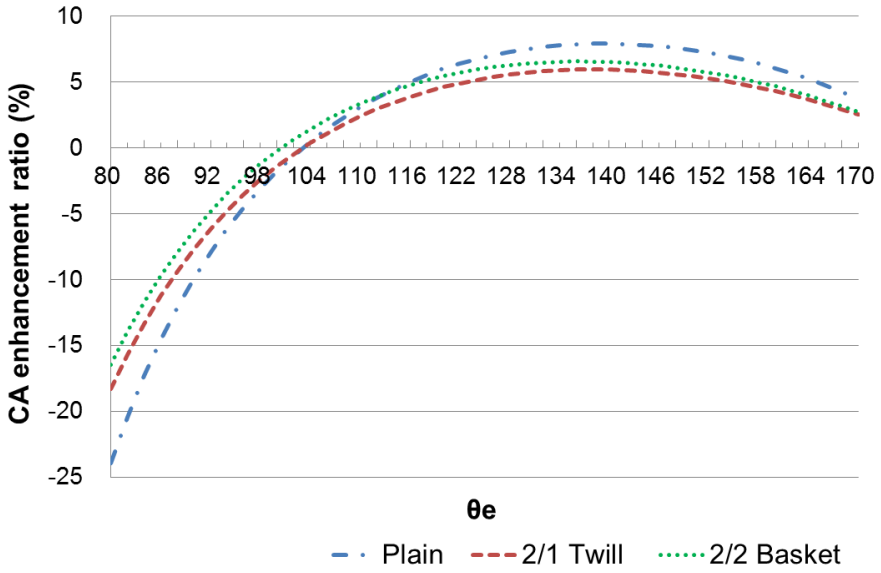

(b) Contact angle enhancement ratio

Figure 4. 11 (a) Predicted contact angle and (b) the ratio of contact angle of each woven structures from the initial angle, *θe*.

In the region of $\theta_F > \theta_e$, the enhancement ratio of the predicted apparent contact angle to the Young contact angle is slightly higher in the plain structure than a 2/1 twill and a 2/2 basket weave. The enhancement ratio is at the maximum when the Young contact angle is around 140˚ in the plain woven structure. It is possible that the higher angle in a plain structure is provided by its short float length, leading to the lower contact area of a liquid on the plain woven fabric surface.

4.2.2 Prediction using a geometric model of lenticular yarn by *e*

The flattening factor, *e*, is a parameter to show the relationship between the major axis and minor axis of a yarn cross-section when the yarn cross-section is being transformed from circular to lenticular shape under pressure. If *e*=1, the yarn cross-section is circular; if it is less than 1, the minor axis, *b*, is flattened to the major axis, *a*. It is expected that the larger flattening leads to the lower contact angle at the same Young contact angle (θ_e) compared to the circular yarn cross-section.

Contact angles when e=1 (a=b)

The Cassie-Baxter equation was extended with *e* using the newly developed Cassie-Baxter model of the lenticular yarn. The predicted fabric's liquid resistance when *e*=1 (circular yarn) showed the same tendency of the fabric contact angle for three weave structures as described in the previous section, 4.2.1. The enhancement ratio of the fabric contact angle was the highest in plain weave. The Young contact angle transiting from the Wenzel state to the Cassie-

Baxter state of a liquid was 109˚ for plain and 2/1 twill and 105˚ for 2/2 basket, which were slightly higher than the Young contact angles in the circular Cassie-Baxter model.

Contact angles when e<1 (a>b)

The flattening factor, *e*, begins to decrease when the length of minor axis, *b*, is compressed under pressure during the interlacing of warp and weft yarns; a smaller flattening factor indicates larger compression of the minor axis, *b*, and flattening of the major axis, *a*. When $e<1$, the enhancement ratio of contact angle is observed in the negative and positive region; at a specific initial angle (θ_e), the transition from negative to positive region is shown in the enhancement ratio of contact angle for each woven structure; plain, 2/1 twill, 2/2 basket.

The influence of the flattening factor on the change of the contact angle is exhibited at specific initial contact angles as shown in Fig. 4.16: (a) at 109˚, (b) at 122˚, (c) at 150˚, (d) at 170˚. In most of the initial angles for each structure, the enhancement ratio of contact angle increases slightly at first, and then begins to decrease at a specific yarn flattening ratio. At high initial contact angles, the tendency of increasing and decreasing at certain points is reduced; (c) and (d) shows the reduced tendency of plain and basket structures compared to (a) and (b). As the initial contact angle becomes higher, the impact of the yarn flattening decreases on the contact angle: none of the structures are affected strongly if the initial angle is high: e.g. 150°.

Figure 4. 12 Influence of flattening ratio of cross-section on changes of contact angle calculated at initial angles (θ_e): (a) at 109˚, (b) at 122˚, (c) at 150˚, (d) at 170˚.

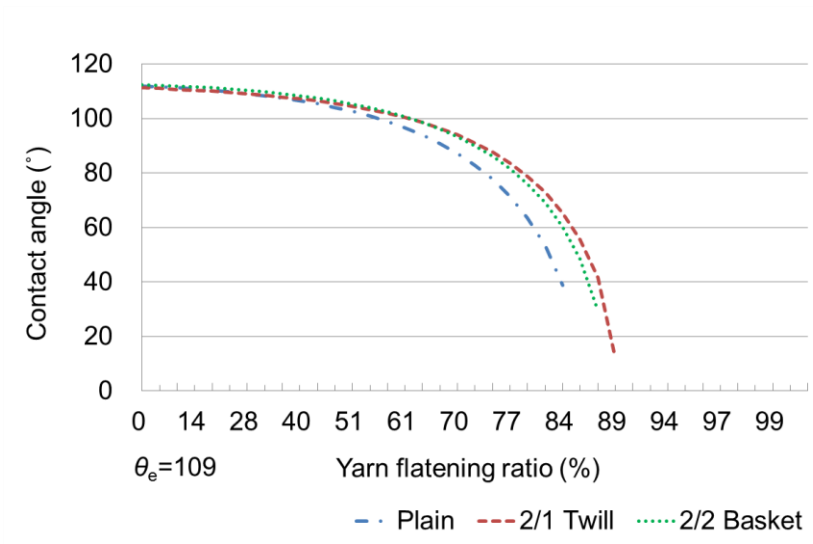
120
100
80
60
40
20
0
Contact angle (°)
0 14 28 40 51 61 70 77 84 89 94 97 99
θe=109
Yarn flatening ratio (%)
Plain
2/1 Twill
2/2 Basket

(a)

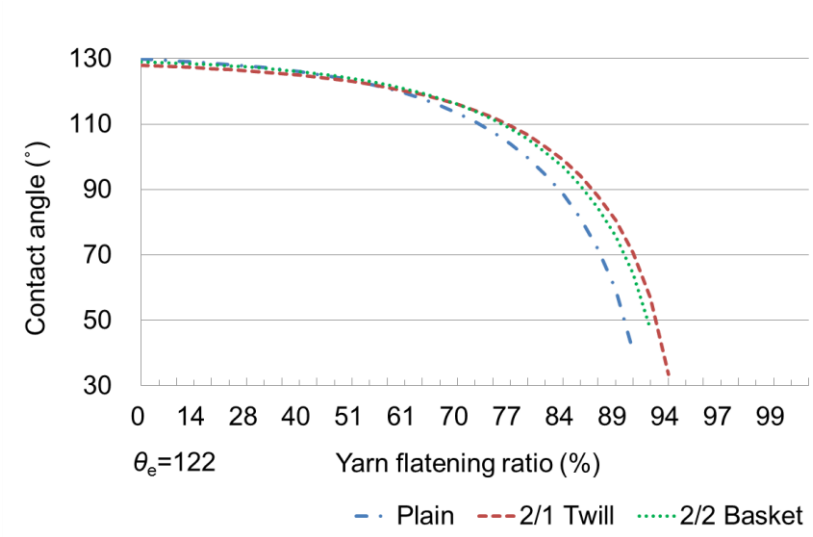
130
110
90
70
50
30
Contact angle (°)
0 14 28 40 51 61 70 77 84 89 94 97 99
θe=122
Yarn flatening ratio (%)
Plain
2/1 Twill
2/2 Basket

(b)

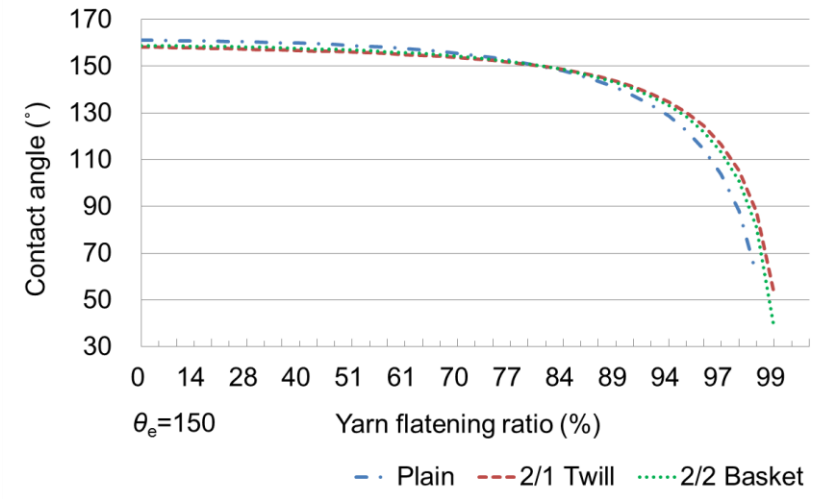
170
150
130
110
90
70
50
30
Contact angle (°)
0 14 28 40 51 61 70 77 84 89 94 97 99
θe=150
Yarn flatening ratio (%)
Plain
2/1 Twill
2/2 Basket

(c)

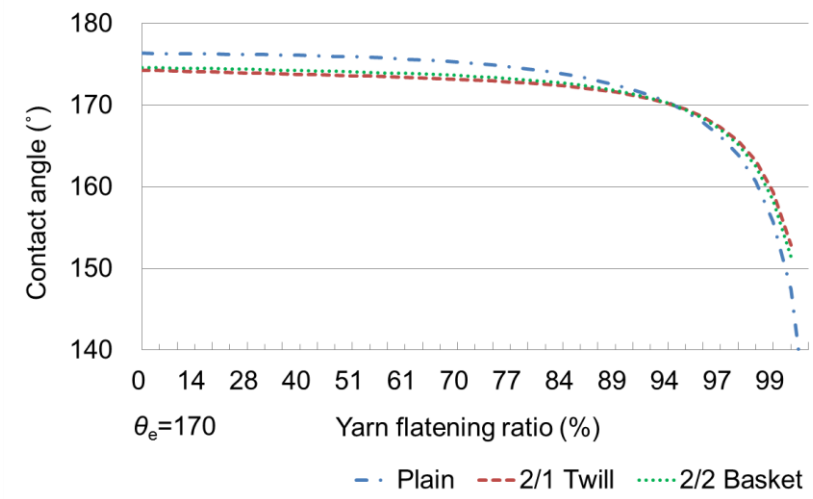
180
170
160
150
140
Contact angle (°)
0 14 28 40 51 61 70 77 84 89 94 97 99
θe=170
Yarn flatening ratio (%)
Plain
2/1 Twill
2/2 Basket

(d)

The result of the predicted contact angles under the influence of yarn flattening indicates that woven structures require initial contact angles high enough to avoid the decrease of contact angle; the initial contact angle is dependent on the woven structure. The influence of the flattening ratio affects each woven structure differently; the plain structure is more subject to the yarn flattening under pressure than the 2/1 twill and 2/2 basket, while the plain presents the slightly higher contact angles. This shows that the flattening of yarn cross-section is an important factor contributing to the determination of the surface property of woven fabric; for liquid relevant properties, it will affect the superhydrophobicity, superoleophobicity, liquid repellency, etc. by reducing the roughness and increasing the contact area of liquid, leading the decrease of void space to support the liquid-vapor interfacial region.

In summary, when a yarn is compressed, the flattening factor decreases. To examine the impact of the yarn flattening on a liquid wetting behavior, the four Young contact angles have been chosen. They are 109˚, 122˚, 150˚, and 170˚. The result shows that the fabric contact angle increases slightly at first, then decreases when the flattening ratio reaches a specific point as shown in Figure 4.16. The fabric contact angle decreases more greatly when the Young contact angle is low. Also, the tendency of the fabric contact angle to change is different in three of the woven fabric structures. While plain is affected more by flattening, the 2/1 twill and 2/2 basket are relatively stable to the yarn flattening effect. The plain structure tends to have the highest angle when the Young contact angle is high enough.

The results when e=1 and e < 1 indicate that the Young contact angle and the yarn compression are important for determining the liquid resistance of woven fabrics having different weave structures. Therefore, both factors should be considered for creating the geometry of a superoleophobic surface.

4.2.3 Prediction using geometric model of lenticular yarn by *e* and *T*

Contact angle at maximum fabric density (e=1, T=0.75)

The maximum fabric density was calculated at the maximum cover factor of 16 for a given yarn diameter as shown in Table 4.3. For the derivation of maximum cover factor, it is assumed that the warp and weft yarns were the same and the cross-section of the yarn is circular, which means that the flattening factor equals 1 (e=1, a=b), i.e. the yarn is not affected by the yarn compression while the warp and weft yarns are interlaced during weaving. The void space ratio to the yarn diameter is specified by the difference between the yarn spacing (warp or weft), p, and the yarn diameter, $2R_y$. The void space ratio of 0.75 means that the void space between two adjacent yarns is 75% of the yarn diameter. The void space ratio can be varied by decreasing the fabric density from the maximum ends or picks per unit length. The different void space ratios will affect the change of liquid behavior. The apparent contact angle can be used to predict the liquid behavior in the different geometrical conditions. Therefore, it is calculated for each woven structure using the Cassie-Baxter equation extended by the void space ratio, T.

Figure 4.17 shows the change of apparent contact angle of the woven structures such as plain, 2/1 twill, and 2/2 basket weave for e=1 and T=0.75. The graph points out that the different void space ratios contribute to the change of the woven geometrical structure, which leads to the different results of the apparent contact angle. The contact angle of the 2/1 twill woven structure begins to steeply increase at the low yarn contact angle, θ_y, however, it goes down below the contact angle of the plain woven structure from a specific point of the yarn contact angle, θ_y. The 2/2 basket structure usually leads to the lower contact angle than the other structures. However, for θ_y > 105°, the difference in the fabric contact angle is small.

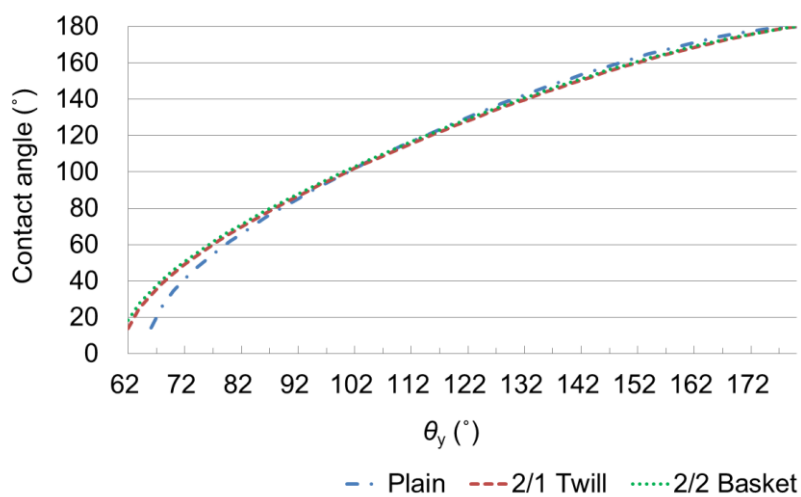

Figure 4. 13 Apparent contact angle of woven structures at T=0.75

For the apparent fabric contact angle, the yarn contact angle, θ_y, is used in the Cassie-Baxter equation instead of the Young contact angle (θ_e). The yarn contact angle is the apparent contact angle of yarn, which is calculated in the Cassie-Baxter model of yarn. The yarn contact angle was allowed to range from 30˚ to 180˚. However, the fabrics did not show apparent contact angles greater than 0° until the yarn contact angle reached specific values as given in Table 4.8 below. For apparent yarn contact angles less than these values, the fabric was fully wetted.

Table 4. 8 Minimum yarn contact angle (θ_y) for θ_F>0 when e=1, T =0.75

W_{fd}	T	θ_y (˚)		
		Plain	2/1 Twill	2/2 Basket
-	-	70	65	64
1.00	0.75	66	62	61

Each yarn contact angle was compared with the one obtained in the Cassie-Baxter model without consideration of the void space ratio, T. Both models assume that the cross-section of the yarn is circular, however, they have different void space ratios. The results show that the void space between yarns contributes to lowering of the yarn contact angle to obtain the first fabric apparent contact angle. This implies that the void space plays a role in enhancing the liquid behavior. Therefore, the void space between yarns should be considered in any fabric structure. In addition, the impact of the void space ratio has to be defined to improve the functionality of fiber, yarn, or fabric structure more effectively.

Figure 4.18 shows the enhancement ratio of the apparent contact angle for each woven structure when the fabric density is maximum for a given yarn diameter (W_{rd}=1, T=0.75). The enhancement ratio of a 2/1 twill structure is the largest below a yarn contact angle of 120˚, however, the plain woven structure becomes higher than the 2/1 twill woven structure above 120˚. The result of an enhancement ratio explains the change of the apparent contact angle of the 2/1 twill structure.

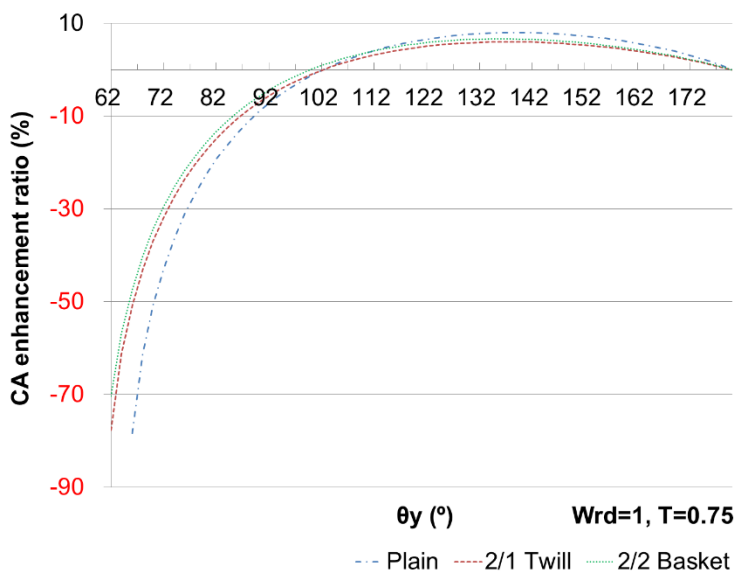

Figure 4. 14 Enhancement ratio of apparent contact angle for different woven structures.

The enhancement ratio in Fig. 4.18 indicates that each structure needs to meet a specific yarn contact angle to obtain a higher fabric contact angle (θ_F) than the yarn contact angle (θ_y). Table 4.9 shows the different yarn contact angles which should be obtained from the yarn structure

for each woven structures; plain, 2/1 twill, and 2/2 basket, when e=1 and T=0.75. The required yarn contact angle is lower for the plain and the 2/1 twill structures than 2/2 basket structure, which is in agreement with the result in Fig. 4.8. The plain and 2/1 twill structures are more efficient weave structures for liquid repellency since they show the higher apparent contact angle for the woven fabric than the 2/2 basket weave at the same yarn contact angle. The required minimum yarn contact angle (e=1, T=0.75) is compared with the minimum yarn contact angle (e=1) obtained in the Cassie-Baxter model without considering the void space, T. All of the woven structures with T show a lower minimum yarn contact angle than the one without T. This implies that the void space in the woven structures allows the lowering of the minimum yarn contact angle which is required to obtain a higher fabric apparent contact angle than the yarn contact angle. In addition, the void space is reduced when the yarn twist increases, which leads the decrease of the apparent contact angle from the yarn structure by packing fibers much more closely. This suggests that the creation of irregular protuberances on a fiber surface could be beneficial to maximize the amount of void space even when the yarn is twisted.

Table 4. 9 Minimum yarn contact angle (θ_y) for $\theta_F > \theta_y$ when e=1, T =0.75

W_{fd}	T	θ_y (˚)		
		Plain	2/1 Twill	2/2 Basket
-	-	109	109	105
1.00	0.75	103	103	100

Contact angles at various fabric densities below maximum (e=1, T >0.75)

By decreasing or increasing the fabric density, the void space can be enlarged or reduced in the woven structures. The maximum fabric density at the maximum cover factor (K=16) was reduced by 5% of the maximum fabric density.

As the fabric density decreases, the void space between yarns increases steeply. When the fabric density reduces by 30%, the void space increases to two times the void space at the maximum fabric density; and by 50% the void space increases to over three times. Above 50%, the void space begins to increase much more steeply compared to the void space at the maximum density. This shows that the fabric density strongly affects the change of void space in the woven structures. The varied values of T are used to predict the apparent contact angle at the different fabric density for the woven structures. The apparent contact angle can be calculated using Eq. 4.24 and Eq. 4.28, and Eq. 4.31.

The apparent contact angle of woven structures increases as the fabric density decreases and the void space increases. The larger void space ratio leads to the steep increase of contact angle until the yarn contact angle reaches 108˚-110˚. As the yarn contact angle is closer to 180˚, the enhancement of the apparent contact angle becomes smaller for each structure. The void space influences more strongly the change of apparent contact angle of each structure at the low yarn contact angle. It means that the void space in the woven structures plays a critical role to enhance the liquid behavior.

Even though an increase of the void space drives to the higher apparent contact angle of the woven structures, it also requires a specific yarn contact angle for $\theta_F > 0^\circ$ as seen in Table 4.10. As the fabric density deceases, the yarn contact angle for $\theta_F > 0^\circ$ becomes lower. When 15% of the maximum fabric density, the yarn contact angle reduces up to 15% for plain, 15% for 2/1 twill, and 11% for 2/2 basket woven structures; when 70% of the maximum fabric density, it decreases by 38% for plain, 37% for 2/1 twill, and 30% for 2/2 basket; when 50% of the maximum fabric density, it was 55% for plain, 52% for 2/1 twill, and 51% for 2/2 basket weave.

Table 4. 10 Minimum yarn contact angle (θ_y) for θ_F>0 when e=1, T >0.75

W_{fd}	T	θ_y (˚)		
		Plain	2/1 Twill	2/2 Basket
1.00	0.75	66	62	61
0.95	0.84	63	59	59
0.90	0.95	59	56	56
0.85	1.06	56	53	54
0.80	1.19	52	49	51
0.75	1.34	47	44	47
0.70	1.50	41	39	43
0.65	1.69	34	32	38
0.60	1.92	30	30	31
0.55	2.18	30	30	30
0.50	2.50	30	30	30
0.45	2.89	30	30	30
0.40	3.37	30	30	30
0.35	4.00	30	30	30
0.30	4.84	30	30	30
0.25	6.00	30	30	30
0.20	7.75	30	30	30
0.15	10.66	30	30	30
0.10	16.50	30	30	30
0.50	33.99	30	30	30

This result shows that the plain weave is most greatly affected by the void space, which decreases the required yarn contact angle for $\theta_F > 0^\circ$. It means that the plain woven structure will be more effective to achieve the better liquid resistance than other structures. With over 35% for plain and 2/1 twill and 45% for basket, the structures begin to show the apparent contact angle even at 30˚ of the yarn contact angle.

Table 4.11 shows the necessary minimum yarn contact angle to obtain the higher fabric apparent contact angle than the yarn contact angle in the extended Cassie-Baxter model using *T*. The minimum yarn contact angle varies at the different fabric density.

The fabric density becomes lower as the void space increases; at 85% of the maximum fabric density, it reduces by 16% for plain and 2/1 twill, and 12% for 2/2 basket; when 70%, it is 38% for plain and 2/1 twill, and 31% for 2/2 basket; at 50%, it decreases by 71% for plain and 2/1 twill, and 70% for 2/2 basket. The minimum yarn contact angle decreases as the void space increases at the low fabric density. This implies that creating void space will lead to the more efficient functionality of woven fabric for the liquid resistance.

Table 4. 11 Minimum yarn contact angle (θ_y) for $\theta_F > \theta_y$ when e=1, T >0.75

W_{fd}	T	θ_y (˚)		
		Plain	2/1 Twill	2/2 Basket
1.00	0.75	103	103	100
0.95	0.84	98	98	97
0.90	0.95	93	93	93
0.85	1.06	87	87	88
0.80	1.19	81	81	83
0.75	1.34	73	73	76
0.70	1.50	64	64	69
0.65	1.69	52	52	60
0.60	1.92	35	35	49
0.55	2.18	30	30	33
0.50	2.50	30	30	30
0.45	2.89	30	30	30
0.40	3.37	30	30	30
0.35	4.00	30	30	30
0.30	4.84	30	30	30
0.25	6.00	30	30	30
0.20	7.75	30	30	30
0.15	10.66	30	30	30
0.10	16.50	30	30	30
0.50	33.99	30	30	30

The Cassie-Baster model extended by the void space ratio, T, is comparable with the one without considering T. This is because the extended Cassie-Baxter model identifies the impact of the void space between yarns in the geometry of woven structures. In this model, the apparent contact angle of fabric is obtained by calculating the extended equation. It leads to more accurate prediction of liquid behavior on a fabric surface through including the consideration of the void space in the designed woven fabric geometry. The fabric density

determines the void space between yarns. The change of void space strongly influences the increase or decrease of the fabric apparent contact angle. A larger void space ratio than 0.75 leads to a lowering of the minimum yarn contact angle necessary to display the first apparent contact angle and the higher apparent contact angle than the yarn contact angle which is applied in the extended Cassie-Baxter equation.

Especially, the plain woven structure shows the larger impact of the void space and its change since it contains the larger void space in the same unit area for a given yarn diameter compared to the other structures; 2/1 twill and 2/2 basket. It is expected to decrease the contact area of liquid on the surface of plain woven fabric, which is critical to maximize the liquid resistance against a solid surface. In developing the Cassie-Baxter model by *T*, it assumes that the yarn cross-section is completely circular and the size of droplet is large enough to breach the void space between fibers and yarns. However, the yarn flattening in the woven structure is an important factor for a more exact prediction of liquid behavior on the surface of designated fabric geometry. The size of droplet will also influence the determination of a maximum range of void space in the woven structures. Therefore, it requires discussing the impact of the yarn flattening with regards to the void space and the droplet size to define the most powerful geometry of woven fabric to maximize the liquid behavior. A further consideration of the yarn flattening and the liquid size will strongly enhance the geometry of cloth fabrics to repel the liquid on the fabric surface.

Change of contact angle when $e \leq 1$ (T=0.75)

In identifying the effect of yarn flattening on the fabric's contact angle at the varied void space ratios, *T*, three yarn contact angles have been chosen at 66˚, 103˚, and 150˚. The yarn contact angle (θ_y) of 66˚ is the minimum angle to obtain the fabric contact angle (θ_F) over 0˚ ($\theta_F > 0$˚). The other yarn contact angle of 103˚ is the minimum angle to show the higher fabric contact angle than the yarn contact angle ($\theta_F > \theta_y$). The third yarn contact angle of 150˚ is the minimum angle of a liquid at which the solid surface reaches the superhydrophobicity or superoleophobicity state.

In the prediction of different fabrics' contact angles, almost all of the fabric contact angles at each θ_y in the flattening factors from *e*=1 to *e*=0.1 have the higher value in the order of plain, 2/1 twill, and 2/2 basket structures. It indicates that the void space ratio to the yarn diameter, *T*, is greater in the plain woven fabric structure than the other structures even as the yarn flattening is continuing (A.4.1 - A.4.10). However, a few contact angles at *e*=1 to *e*=0.7 show the higher fabric contact angle in the 2/1 twill structure than in the plain structure, when θ_y=66˚. The plain structure has a transition point of *T* from the lower fabric contact angle, θ_F, to the higher one relative to the 2/1 twill woven structure ($\theta_{F\_plain} < \theta_{F\_2/1twill}$ to $\theta_{F\_plain} > \theta_{F\_2/1twill}$). The transition value of *T* is shown in Table 4.12. At each of the three yarn contact angles, the fabric contact angles of plain, 2/1 twill, and 2/2 basket structures are calculated by the newly developed Cassie Baxter equations.

Table 4. 12 T for transition to $\theta_{F\_plain} > \theta_{F\_2/1twill}$ at θ_y=66˚

e	1.0	0.9	0.8	0.7
T	1.50	1.34	1.19	1.19

In Table 4.12, the void space ratio, T, decreases as the yarn flattening becomes greater. That is, the plain woven structure obtains a higher fabric contact angle than the 2/1 twill woven structure at lower T as the yarn is being flattened under tension. In the range of e=1 to e=0.7, the liquid resistance of the woven fabric is not affected greatly by the yarn flattening, which means the warp and weft yarns are compressed by around 50%. However, the liquid resistance decreased as the yarn compression was continued over 50% (e < 0.7). When $\theta_F > \theta_y$, the plain woven structure showed the highest contact angle amongst the three structures. This is because the surface of the plain woven structure has a lower contact area of the liquid droplet, leading to better performance in liquid repellency. In summary, this prediction examined the change of the fabric contact angle at varied T values in three different woven structures for the given yarn contact angle (θ_y=66˚, 103˚, or 150˚) when $e \leq 1$. In the next section, the change of the fabric contact angle will be analyzed in the same woven fabric structure to determine the difference of enhancement ratio in the fabric contact angle as e=1 to e=0.1.

Difference of contact angle in the same woven structure when e ≤ 1

The enhancement ratio shows how much the fabric contact angle increases when the value of variables changes from one to another. In this study, the variable T switches from 0.75 to 86.49

and the variable *e* has a range from 1 to 0.1. The fabric contact angle is predicted for three woven fabric structures by Eq. 4.25, Eq. 4.28, and Eq. 4.31 at varied *T* value for a given yarn flattening ratios. The fabric contact angles in the different flattening ratio are compared to each other by the enhancement ratio in the same woven structure; plain, 2/1 twill, or 2/2 basket woven structure. The difference among the enhancement ratio at each *e* will identify how the yarn flattening impacts the change of the fabric contact angle (A.4.11 – A.4.13).

The enhancement ratio is expressed as a percentage (%). The graph of the enhancement ratio goes downwards to the lower percentage in the same woven structure when the yarn flattening ranges from 1 to 0.1. At θ_y=66˚, three woven structures had the largest reduction of the enhancement ratio when *e* switches to 0.9, then next to 0.8. The plain and 2/2 basket woven structures decrease more significantly than the 2/1 twill woven structure in the enhancement ratio when changing from *e*=1 to *e*=0.9 or *e*=0.8. The fabric contact angle reduces around 10% - 30% in the plain structure while the reduction is around 10% between *e*=1 to *e*=0.9 (θ_y=66). For the 2/1 twill structure, it also shows the reduction of the fabric contact angle when the yarn flattening factor decreases. It is around 3% - 20% from *e*=1 to *e*=0.9 and less than 10% from *e*=0.9 to *e*=0.8. After *e*=0.8, the reduction of the fabric contact angle gradually decreases between the two different ratios of yarn flattening.

At θ_y=103˚ and θ_y=150˚, the difference of the enhancement ratio between two flattening factors, *e*, greatly decreases compared to the one at θ_y=66˚. The largest reduction is between *e*=0.3 to

e=0.2 for θ_y=103˚ and between e=0.2 to e=0.1 for θ_y=150˚. This result is comparable with the largest reduction between e=0.2 to e=0.1 when θ_y=66˚. It identifies that there is a critical point of yarn flattening showing a significant reduction of the fabric contact angle in the woven structure for a given θ_y. The reduction of the fabric contact angle is high in the order of θ_y=66˚, θ_y=103˚, and θ_y=150˚. It implies that the effect of yarn flattening becomes greater in the reduction of the fabric contact angle when the yarn contact angle, θ_y, decreases. That is, the impact of yarn flattening on the change of contact angle depends on the woven fabric structure and the yarn contact angle.

4.2.4 Prediction using geometry model of multifilament yarn

Contact angle at different ratios of fiber distance, d_f, to fiber radius, R_f

The different ratios of d_f to R_f are applied to Eq. 4.24 at the given Young contact angle and a specific fiber radius to determine the effect of void space on change of contact angle. The range of the Young contact angles is considered from 180° to 10° to examine the difference of apparent contact angle which is changed after applying different ratios of fiber distance to fiber radius for the given Young contact angle.

The contact angle is more strongly affected by the ratio of fiber distance to fiber radius at the lower Young contact angle. The difference between the Young contact angle and the apparent contact angle increased as the Young contact angle decreased as seen in Table 4.13. This table

shows that the lower contact angle leads to a larger enhancement ratio of apparent contact angle when the distance ratio of fibers to fiber radius (d_f/R_f) changes from 0 to 3.5. The ratio of distance between 0 to 1 increases more steeply than the apparent contact angle rather than the higher value of distance ratio; ratios over 1 show a moderate increase of apparent contact angle.

Table 4. 13 Difference of enhancement ratio between θ_e and θ_y at $d_f/R_f = 0$ and 3.

θ_e	Difference between θ_e and θ_y (%)	
	$d_f/R_f = 0$	$d_f/R_f = 3$
175	2.0	2.5
170	3.8	5.0
165	5.3	7.3
160	6.5	9.7
155	7.5	12.0
150	8.3	14.5
145	8.9	16.6
140	9.0	17.0
135	9.6	22.3
130	9.7	25.0
125	9.6	28.0
120	9.3	31.3
115	8.7	34.7
110	7.8	38.0
105	6.6	42.3
100	5.0	46.6

The enhancement ratio between the Young contact angle and apparent contact angle begins to increase significantly from a Young contact angle of 95°; especially at low value of fiber

distance ratio from 0 to 0.6. The apparent contact angle reaches over 100° even though the Young contact angle is low. It means that the apparent contact angle will be more steeply increased at the Young contact angle below 100° as shown in A. 4.14 (f), (g), (h), (i), (j). The difference between the Young contact angle and the apparent contact angle is more largely increased at the distance ratio is larger.

Minimum ratio of fiber distance, d_f, to fiber radius, R_f

Under the Young contact angle of 90°, the apparent contact angle of yarn begins to negatively increase for some distance ratio of fibers; in which the apparent contact angle is lower than the Young contact angle. However, it started to increase at a specific point of distance ratio, d_f over R_f, and the higher ratio was required as the Young contact angle is decreased. Also, a Young contact angle below 55° does not show any apparent contact angle until the fiber distance ratio to fiber radius reaches to a specific point; 0.05 for 55°, 0.15 for 50°, 0.20 for 45°, 0.40 for 40°, 0.35 for 35°, 0.40 for 30°, 0.45 for 25°, 0. 50 for 15° and 10°. It means that the low Young contact angle requires sufficient distance between fibers to obtain the apparent contact angle as well as a specific value of distance to increasing the apparent contact angle compared to the Young contact angle. It indicates that the low Young contact angle is affected significantly by the void space in a solid structure to reach an apparent contact angle's increase.

Table 4. 14 Minimum ratio of fiber distance to fiber radius to obtain the minimum Young contact angle of each woven structure

θ_e (°)	ratio of d_f to R_f		
	Plain	2/1 twill	2/2 basket
95	0.16	0.16	0.11
90	0.35	0.35	0.30
85	0.50	0.50	0.46
80	0.75	0.75	0.65
75	0.95	0.95	0.85
70	1.15	1.15	1.05
65	1.35	1.35	1.25
60	1.55	1.55	1.45
55	1.80	1.80	1.65
50	2.00	2.00	1.85
45	2.20	2.20	2.05
40	2.40	2.35	2.25
35	2.55	2.55	2.40
30	2.70	2.70	2.55
25	2.85	2.85	2.70
20	3.00	2.95	2.80
15	3.10	3.05	2.90
10	3.15	3.15	2.95

In the previous study, it was pointed out that the specific minimum Young contact angle for each woven structure should be achieved at the level of yarn structure; 104.5° for plain 104.4° for 2/1 twill, and 102.6° for 2/2 basket structure; each minimum Young's contact angle can be considered by the apparent contact angle of multifilament yarn which is described above. As seen in the following graph in A. 4.14, the apparent contact angle of multifilament yarn is always higher than the required minimum Young contact angle of woven structures if the

Young contact angle of fiber is equal or over 100°. However, if the Young contact angle of fiber is lower than 100, it needs to achieve a minimum distance between filaments as shown in Table 4.14.

The result shows that each woven structure requires a higher ratio of fiber distance as the lower Young contact angle is applied for the prediction of apparent contact angle of multifilament yarn. The specific ratio of fiber distance to fiber radius emphasized the importance of sufficient void space between filaments, which plays a critical role to support a liquid droplet on a solid surface, even for a liquid with low surface tension; the low surface tension leads to larger contact area of liquid due to stronger adhesiveness of liquid to a solid surface. Sufficient void space according to the minimum distance ratio (d_f/R_f) or which is more than the ratio (d_f/R_f) should be provided to enhance the oleophobicity at the yarn level.

For sufficient void space, developing a protuberance on a fiber surface can be considered to maintain the void space between fibers (filaments) in a multifilament yarn. The steep and longer protuberance on a fiber surface would lead to the stronger persistence of void space between fibers when the multifilaments are bundled together in a yarn. In multifilament yarn formation, yarn twisting is also considered due to the reduction of yarn diameter under the torsion of filaments in a yarn.

4.3 Evaluation using actual woven fabrics

The geometry of woven fabric has been studied theoretically to define its relationship to wetting behavior in the deposition of a liquid droplet on the fabric surface. This relationship emphasizes that the void space in the solid structure is critical to improving the wetting behavior. The void space contributes to minimizing the contact area of the liquid droplet to the solid surface, contributing to the liquid-repellency. The impact of air has been identified in the theoretical model of the woven fabric structure. It should be proven via testing the actual woven fabric. The woven fabric structure or the amount of the void space will result in different wetting behaviors, observed by the contact angle of the liquid droplet on the fabric surface. When testing, it is assumed that the surface energy is low enough relative to the surface tension of the liquid. Thus, the geometry of the solid surface will be the strongest influence to change the wetting behavior of the liquid on the woven fabric surface.

4.3.1 Wetting behavior of NCSU manufactured woven fabrics

Characteristics of NCSU manufactured woven fabrics

Several types of woven fabrics have been produced by the woven fabric manufacturing facilities in the College of Textiles (CoT), NCSU as shown in Table 4.15. Each group is manufactured with the same type of fibers, for example cotton or cotton blend. Also the woven fabrics are also organized by different fabric densities or different woven structures.

Table 4. 15 Characteristics of NCSU manufactured fabrics

Group		Fabric type	Fabric density		Fiber type		Yarn density (den)		Yarn diameter (cm)	
			Ends/inch	Picks/inch	Warp	Weft	Warp	Weft	Warp	Weft
A	1	plain (a)	96	59.5	50/50 Cot/PET	50/50 Cot/Ny	266	332	0.022	0.025
	2	plain (b)	96	58.0	50/50 Cot/PET	50/50 Cot/Ny	266	332	0.022	0.025
	3	plain (c)	96	56.6	50/50 Cot/PET	50/50 Cot/Ny	266	332	0.022	0.025
	4	plain (d)	96	53.8	50/50 Cot/PET	50/50 Cot/Ny	266	332	0.022	0.025
	5	plain (e)	96	49.6	50/50 Cot/PET	50/50 Cot/Ny	266	332	0.022	0.025
	6	3/3 RH twill	96	59.5	50/50 Cot/PET	50/50 Cot/Ny	266	332	0.022	0.025
	7	3/3 basket	96	59.5	50/50 Cot/PET	50/50 Cot/Ny	266	332	0.022	0.025
	8	3/3 warp rib	96	59.5	50/50 Cot/PET	50/50 Cot/Ny	266	332	0.022	0.025
	9	3/3 filling rib	96	59.5	50/50 Cot/PET	50/50 Cot/Ny	266	332	0.022	0.025
B	1	2/2 weft rib	36	40	Cot	Cot	744	744	0.036	0.036
	2	2/1 RH twill	36	40	Cot	Cot	744	744	0.036	0.036
	3	2/2 basket	36	40	Cot	Cot	744	744	0.036	0.036
	4	3/1 twill	36	40	Cot	Cot	744	744	0.036	0.036
	5	plain	36	40	Cot	Cot	744	744	0.036	0.036

Structural geometry and liquid contact angle of NCSU manufactured woven fabrics

The structural geometry and the liquid contact angle were observed after all NCSU manufactured woven fabrics were chemically treated using FS ($C_{13}H_{13}O_3F_{17}Si$). Yarn geometries of the NCSU manufactured woven fabrics are described in Table 4.16. The yarn diameter ($2R_y$) and the yarn distance (D_y) are identified through capturing the SEM images of the fabrics (Fig. 4.19). The fabric contact angle is observed in the images of a liquid droplet deposited on a woven fabric surface (Fig. 4.20).

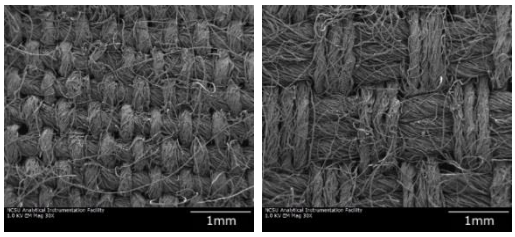

(a) (b)

Figure 4. 15 SEM images of FS treated woven fabrics: (a) A5 plain weave, (b) A7 basket weave.

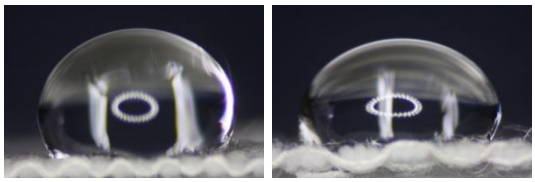

(a) (b)

Figure 4. 16 Deposition of dodecane on FS treated woven fabric surface: (a) A5 plain weave, (b) A7 basket weave.

Table 4. 16 Fabric contact angle (θ_F) of dodecane in different FS treated NCSU manufactured woven fabric structures

Group		Fabric type	Yarn geometry			θ_F (˚)
			$2R_y$	$p\text{-}2R_y$	T_y	
A	1	plain (a)	264.6	58.4	0.22	108.3
	2	plain (b)	253.2	60.3	0.24	116.7
	3	plain (c)	248.3	66.1	0.27	116.0
	4	plain (d)	247.7	72.6	0.29	120.3
	5	plain (e)	251.6	87.3	0.35	122.7
	6	3/3 RH twill	242.3	47.9	0.20	118.3
	7	3/3 basket	238.6	169.9	0.71	124.0
	8	3/3 warp rib	254.2	184.3	0.72	119.0
	9	3/3 filling rib	246.2	148.1	0.60	111.3
B	1	2/2 weft rib	499.5	179.8	0.36	131.2
	2	2/1 RH twill	488.1	145.7	0.30	131.3
	3	2/2 basket	539.9	281.3	0.52	125.0
	4	3/1 twill	542.9	131.6	0.24	130.4
	5	plain	564.4	112.8	0.20	138.0

Sample group A shows that the fabric contact angle in plain weave becomes larger when the void space ratio to the yarn diameter increases. It proves the impact of the void space on improving the liquid repellency behavior. Within the same fabric density subgroup of group A, the void space ratio is varied by the different woven structures. Plain weave obtained the much smaller void space ratio to the yarn diameter than the others such as basket, warp rib, and filling rib. The smaller void space ratio means that the plain weave has larger liquid-solid contact area relative to liquid-vapor contact area than other structures. This could be the reason that the other structures show higher fabric contact angle than plain weave in group A at the

same fabric density. It implies the potential capability of a plain structure, which can improve the liquid wetting behavior much more than other structures when its geometry is constructed well to obtain enough void space.

The results for group B also show that plain weave obtains the highest dodecane fabric contact angle. The void space ratio, *T*, is relatively small in plain weaves as compared to the other structures. However, it shows better wetting behavior for the liquid on the plain structure surface. It indicates that the plain weave is the most effective woven structure to achieve an oleophobic or superoleophobic woven fabric surface.

Moreover, the FS treated plain woven fabrics of A1 and B5 obtained different values in the dodecane fabric contact angle even though they have similar void space ratios. It is expected that the difference is caused by the different types of fibers used in each group: cotton/polyester blended for A1 and cotton for B5. The result implies that the fiber raw material in a yarn should be considered when improving the performance of woven fabric in regards to the wetting behavior.

4.3.2 Wetting behavior of collected commercial woven fabrics

Several types of commercial woven fabrics have been collected based on the prediction of the wetting behavior in the NCSU manufactured woven fabrics. Plain or its derivative woven structures were chosen to observe the geometrical impact on the liquid wetting behavior in the

selected commercially available woven fabrics. The derivative structures include basket, twill, weft rib, and ripstop. Testing with the commercial fabrics is recommended to identify any well-performing existing commercial woven fabrics for liquids of low surface tension relative to water.

Characteristics of collected commercial woven fabrics

Table 4.17 shows the characteristics of the top two performing woven fabrics among the selected commercial woven fabrics. The structure of $A_{Com}1$ is plain, defined as the best performing structure in the theoretical prediction and the experimental test of the NCSU manufactured woven fabrics. $A_{Com}2$ is a 3/3 weft rib structure, modified from plain.

Table 4. 17 Characteristics of high performing commercial woven fabrics

Group		Fabric type	Fabric density		Fiber type		Yarn density (den)		Yarn diameter (cm)	
			Ends/inch	Picks/inch	Warp	Weft	Warp	Weft	Warp	Weft
A_{Com}	1	plain (a)	36	31	55/45 linen/rayon	55/45 linen/rayon	1022	1022	0.042	0.042
	2	3/3 weft rib	87	28	Cot	Cot	1049	1049	0.042	0.042

Structural geometry and liquid contact angle in selected commercial woven fabrics

All commercial woven fabrics were chemically treated using FS ($C_{13}H_{13}O_3F_{17}Si$) before conducting the observation of their structural geometries and liquid contact angles. The liquid deposition of dodecane on each woven fabric structure is described in Fig. 4.21 and Fig. 4.22. The surface of the selected commercial woven fabrics showed good wetting resistance against the low surface tension liquid. The geometry of yarn in each structure and the result in the fabric contact angle are shown in Table 4.18.

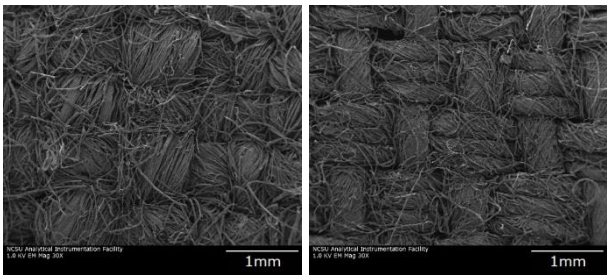

(a) (b)

Figure 4. 17 SEM images of FS treated woven fabrics: (a) $A_{Com}1$, (b) $A_{Com}2$.

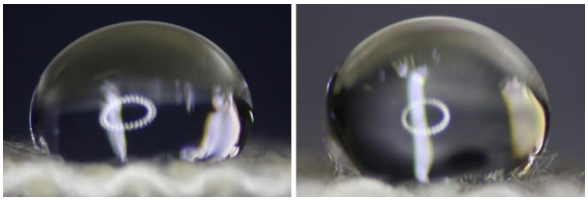

(a) (b)

Figure 4. 18 Deposition of dodecane on FS treated woven fabric surface: (a) $A_{Com}1$-dodecane, (b) $A_{Com}2$-dodecane.

Table 4. 18 Fabric contact angle (θ_F) of dodecane in different FS treated commercial woven fabric structures

Group		Fabric type	Yarn geometry			θ_F (˚)
			$2R_y$	$p\text{-}2R_y$	T_y	dodecane
A_{Com}	1	plain	631.0	146.0	0.23	125
	2	3/3 weft rib	352.5	235.7	0.67	148

The fabric contact angles of dodecane in $A_{Com}1$ and $A_{Com}2$ are in an agreement with the prediction by the void space ratio to a yarn diameter, *T* (Table 4.18). The larger void space ratio leads to the higher fabric contact angle of dodecane in both fabrics. In theory and in the experimental tests, plain weave has been expected to be the most effective structure to improve the liquid wetting behavior. However, in this result, $A_{Com}2$ obtained a higher fabric contact angle than $A_{Com}1$. The cause for the result may be related to the much larger void space ratio, *T*, in the woven structure causing the higher angle of dodecane in $A_{Com}2$.

4.3.3 Geometry analysis of selected high performing woven fabrics

Determination of best-performing woven fabrics among fabric samples

The contact angles of dodecane in woven fabrics attained higher degrees in plain woven structures than in the others such as basket, twill, weft rib, and ripstop. The liquid contact angles were compared within each group in considering void spaces between adjacent yarns

(D_y) and the void space ratio to yarn diameter (T). Although the differences in the void spaces were larger between the plain structure and other structures, plain structures showed small differences in the liquid contact angles compared to the others. Based on the results of the liquid contact angles and the relative geometries of woven structures, the highest performing woven fabric was selected in each group of the NCSU manufactured woven fabrics and the commercially woven fabrics. Table 4.19 shows the geometric values of yarn diameter ($2R_y$), void space (D_y), void space ratio to yarn diameter (T), and liquid contact angles. The subscript *e* and *p* refer to ends (warp yarn) and picks (weft yarn).

Table 4. 19 Geometric values and liquid contact angles of selected woven fabrics

Group		Fabric type	Yarn geometry (cm)				T_e	T_p	θ_F (˚)
			$2R_{ye}$	$2R_{yp}$	p_e-$2R_{ye}$	p_p-$2R_{yp}$			
B_{NCSU}	5	plain	0.052	0.061	0.014	0.008	0.28	0.13	138±4
A_{NCSU}	5	plain (e)	0.020	0.030	0.006	0.012	0.28	0.39	123±8
A_{Com}	1	plain	0.058	0.069	0.021	0.008	0.36	0.12	117±9

The tension of a warp yarn is higher than that of the weft yarn, and warp yarns are less affected by compression occurring when warp and weft yarns interlace (A.4.15). Therefore, warp yarns are less flattened than the weft yarns, which results in a larger void space ratio, T_e in B_{NCSU} and A_{Com} (A.4.16). The A_{NCSU} fabric sample was woven with a relatively low value of picks per inch to ends per inch. For the reason, T_p is larger than T_e.

The result indicates that the plain woven structure is preferred as a weave structure rather than twill, basket, etc. for obtaining a liquid repellent fabric surface. This is in agreement with the theoretical result predicted utilizing the Cassie-Baxter models.

Comparison of actual cover factor and theoretical cover factor

Woven fabric cover factor is the area covered with warp and weft yarn relative to the total fabric area, which is calculated by utilizing the geometrical parameters depicted in the geometrical model of weave structures. It is an important indicator to confirm how many warp or weft yarns are interlaced within one inch. The number of interlacement for a given yarn diameter determines the covered area by warp and weft yarns to the total unit area. The area that is not covered by yarns determines the void spaces within the unit area. The cover factor is calculated using the parameters of $2R$ and p; $2R$ is the diameter of yarns and p is the yarn spacing between the adjacent warp or weft yarns.

The geometries of the selected woven fabrics from groups of $A_{NCSU,}$ $B_{NCSU,}$ and A_{Com} have been studied by analyzing the SEM images. Table 4.20 shows the geometric values of d and p for warp (e) and weft (p) yarns. By using the geometric values, the cover factors were calculated for the warp yarn (K_e), weft yarn (K_p), and fabric (K_f).

Table 4. 20 Actual cover factor observed through SEM image

Group		Fabric type	Yarn geometry (cm)				Cover factor		
			$2R_{ye}$	$2R_{yp}$	p_e	p_p	K_e	K_p	K_F
B_{NCSU}	5	plain	0.052	0.061	0.066	0.069	22	25	27
A_{NCSU}	5	plain (e)	0.020	0.030	0.026	0.042	22	20	26
A_{Com}	1	plain	0.058	0.069	0.079	0.077	21	25	27

Table 4.21 shows the geometric values predicted by utilizing yarn characteristics. Yarn diameter, 2*R*, was calculated in regards to yarn density, fiber density, and fiber packing coefficient. Yarn spacing, *p*, was obtained through assuming the same value of ends or picks per centimeter or per inch of the fabric density with the values observed in the SEM images of the actual fabrics.

Table 4. 21 Theoretical cover factor predicted by yarn characteristics

Group		Fabric type	Yarn geometry (cm)				Cover factor		
			$2R_{ye}$	$2R_{yp}$	p_e	p_p	K_e	K_p	K_F
B_{NCSU}	5	plain	0.036	0.036	0.071	0.064	14	16	22
A_{NCSU}	5	plain (e)	0.022	0.025	0.026	0.051	23	14	25
A_{Com}	1	plain	0.042	0.042	0.071	0.082	17	14	22

The geometric values in Table 4.20 and Table 4.21 show how the yarn compression changes the cover factor for the two yarns and fabrics. The cover factor of the weft yarn increases in

the actual fabric more than that of the warp yarn. The large difference in weft yarn coverage is caused by the large flattening of the weft yarn (A.4.15). The flattening of yarns also increases the fabric cover factor (K_F), decreasing the void spaces including air to the total unit area (A.4.16).

Comparison of actual void space and theoretical void space

Void space is considered an important factor due to the air that can be included in a woven fabric structure. The air prevents a liquid from penetrating into woven structures through the creation of a vapor-liquid interface. The vapor-liquid interface contributes to the transfer of a liquid from the Wenzel state to the Cassie-Baxter state. In the Cassie-Baxter state, the more air there is, the higher liquid contact angle will be when a liquid droplet is placed on the fabric surface. For the actual fabrics, the void spaces were directly measured through SEM images (Table 4.22).

Table 4. 22 Actual void space of fabric geometry observed through SEM images

Group		Fabric type	Void space (cm)		Ratio		
			$p\text{-}2R_{ye}$	$p\text{-}2R_{yp}$	T_e	T_p	T_y
B_{NCSU}	5	plain	0.014	0.008	0.28	0.13	0.21
A_{NCSU}	5	plain (e)	0.006	0.012	0.28	0.39	0.34
A_{Com}	1	plain	0.021	0.008	0.36	0.12	0.24

The prediction of void spaces has been made by calculating the difference between yarn diameter, 2*R*, and yarn spacing, *p*, as described in Table 4.23. Void spaces, D_y, between yarns significantly decreased from the predicted geometry to the observed geometry of the actual woven fabric. The reduction of the void space is caused by the yarn compression occurring when yarns interlace, which lets the yarns be packed into a denser fabric. This decreased the void space ratio to yarn diameter, *T*, which shows a larger difference in the weft yarn than in the warp yarn (A. 4.17)

Table 4. 23 Theoretical void space of fabric geometry predicted by yarn characteristics

Group		Fabric type	Void space (cm)		Ratio		
			$p\text{-}2R_{ye}$	$p\text{-}2R_{yp}$	T_e	T_p	T_y
B_{NCSU}	5	plain	0.035	0.028	0.99	0.79	0.89
A_{NCSU}	5	plain (e)	0.005	0.026	0.22	1.02	0.62
A_{Com}	1	plain	0.029	0.040	0.68	0.95	0.82

4.3.4 Wetting behavior of Laboratory designed woven fabrics (F_{Lab})

Characteristics of prepared smooth yarn surface (SY) and rough yarn surface (RY) multifilament yarns

The smooth surface yarn (SY) and rough surface yarn (RY) multifilament yarns consisted of 34 nylon fibers: smooth surface fibers in the SY and rough surface fibers in the RY respectively.

The roughness was developed through creating protuberances on a fiber at a micro level via the coating process including a liquid bath, UV curing, surface drying, and filament winding. The geometrical difference between the SY and RY is identified using the SEM images of the yarns as shown in Fig. 4.23.

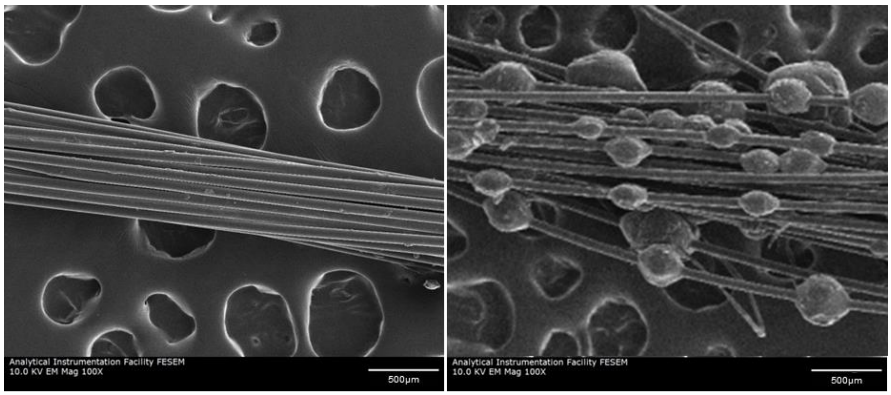

(a) (b)

Figure 4. 19 SEM images for (a) rough surface multifilament yarn, RY, and (b) smooth surface multifilament yarn, SY: 100X, 10KV.

To design structural geometries of the Lab. woven fabrics using the SY and RY, the fabric density should be defined for the two given yarns. The fabric density is characterized by the fabric cover factor (K) and the yarn diameter ($2R_y$). The yarn diameters for the SY and RY were obtained by Eq. 2.7 utilizing the yarn and nylon fiber properties: yarn density (N_{tex}), fiber density (ρ_f), and fiber packing coefficient (ϕ) as shown in Table 4.24. For the RY, it was assumed that the yarn diameter increases relative to the distance between two adjacent fibers,

d_f, as introduced in Fig. 4.10. The fiber distance, d_f, is generated by the averaged size of the protuberances on the fiber surfaces. The protuberances' size in the RY was accounted for by the difference of the fiber linear density (N_{tex}) to the SY. The SY and RY utilized the same number of the fiber packing coefficient considering the regular yarn twist as seen in Table 2.3.

Table 4. 24 Yarn diameters calculated by characteristics of SY and RY

Yarn	Fiber	N_{tex} (g/km)	ρ_f (g/cm^3)	fiber packing coefficient (ϕ)	$2R_y$ (cm)
SY	nylon	17.5 (±0.4)	1.14	0.6	0.018
RY	nylon	136 (±58)	1.14	0.6	0.050

In Table 4.24, it shows that the diameter of the RY was larger than one of the SY. The larger diameter was caused by the roughness and the void spaces created by the micro-scale protuberances on the fiber surfaces of the multifilament yarn. The micro-scale protuberances on fibers transformed from a tightly packed yarn structure (Fig. 2.22 (a)) to a loosely packed yarn structure (Fig. 2.33 (b)) through generating openness, increasing the void space between fibers, in a multifilament yarn structure. The void space supports a liquid droplet on a solid surface to create the liquid-vapor interface beneath the liquid. The presence of the liquid-vapor interface will enhance the liquid repellent property upon the rough surface by reducing the direct contact area of the liquid to a solid surface. The rough surface filament yarn (RY) will be inserted into the open shed of the warp sheet in a horizontal direction as the weft filling pick.

The fabric density referring to the ends or picks per inch is determined by the cover factor for a given yarn. Since the yarn diameters of the SY and RY were identified by their properties, the fabric densities for the laboratory designed woven fabric (F_{Lab}) could be described using the yarn diameters: 0.018 cm for the SY and 0.050 cm for the RY, and the cover factor: K_e=16, K_p=14, K_F=22.

Geometric design of F_{Lab} using yarn diameter ($2R_y$) and cover factor (K)

The highest performing weave structure and the optimum cover factor were selected through an evaluation of the NCSU manufactured woven fabrics and the collected commercial woven fabrics: the structure is plain weave and the cover factors are 16 for a warp direction, 14 for a weft direction, and 22 for fabric (K_e=16, K_p=14, K_F =22). The plain weave and cover factors were utilized to design the structural geometry of $F_{Lab.}$ woven by the SY and RY.

By using these selected cover factors, the fabric density (ends or picks per inch) for the given SY and RY was determined for F_{Lab_SY1} and $F_{Lab.\_RY1}$ as shown in Table 4.25. Then, the fabric density for the RY was varied by decreasing the weft-directional cover factor (picks per inch) from 14 to 5. The varied fabric densities were utilized for the creation of the geometries of the woven fabrics: F_{Lab_RY1} through F_{Lab_RY6}. For all F_{Lab}, the warp-directional density using the SY was maintained at the same ends per inch (K_e=16, 80 ends per inch)

Table 4. 25 Fabric densities determined by selected and varied cover factor for F_{Lab_SY} and F_{Lab_RY}

Fabric		Type	$2R_y$ (cm)		Fabric density		Cover factor		
			wrap	weft	epi	ppi	K_e	K_p	K_F
F_{Lab}	SY1	plain	0.018	0.018	80	69	16	14	22.0
F_{Lab}	RY1	plain	0.018	0.050	80	25	16	14	22.0
	RY2				80	23	16	13	21.6
	RY3				80	20	16	11	20.7
	RY4				80	16	16	9	19.8
	RY5				80	13	16	7	19.0
	RY6				80	9	16	5	18.1

The fabric densities determines the amount of void space between adjacent warp or weft yarns. The higher density leads to a smaller void space. Also, the yarn compression is also influenced by the fabric density as well as tension in the warp or weft yarn. By the selected fabric densities in Table 4.25, the void space, p-$2R_y$, and the void space ratio, T, were defined for the theoretical $F_{Lab._SY}$ and $F_{Lab._RY}$ as shown in Table 4.26. The yarn spacing, p, includes the yarn diameter and the void space between the two adjacent yarns. The theoretical F_{Lab} was assumed that the flattening factor, e, is equal to 1 for the warp yarn (e_e) and weft yarn (e_p). The flattening factor of fabric, e_f, is an average number of e_e and e_p, therefore, e_f equals 1. Each suffix y, e, p, and f refers to yarn, warp yarn, weft yarn, and fabric, respectively.

Table 4. 26 Geometrical characteristics of theoretical fabrics: F_{Lab_SY} and F_{Lab_RY}

Fabric		$2R_{ye}$	$2R_{yp}$	$p\text{-}2R_{ye}$	$p\text{-}2R_{yp}$	T_e	T_p	T_y	$e_{e,p,f}$
F_{Lab}	SY1	0.018	0.018	0.014	0.018	0.75	1.01	0.88	1
	RY1	0.018	0.050	0.014	0.051	0.75	1.01	0.88	1
	RY2	0.018	0.050	0.014	0.058	0.75	1.16	0.96	1
	RY3	0.018	0.050	0.014	0.077	0.75	1.54	1.14	1
	RY4	0.018	0.050	0.014	0.107	0.75	2.13	1.44	1
	RY5	0.018	0.050	0.014	0.150	0.75	2.98	1.86	1
	RY6	0.018	0.050	0.014	0.234	0.75	4.65	2.70	1

Table 4.26 shows that the void space ratio, T_f, is maintained at the same value for F_{Lab_SY1} and F_{Lab_RY1} even though the weft-directional void space becomes larger in F_{Lab_RY1}. The different void space in F_{Lab_SY1} and F_{Lab_RY1} is attributed to utilizing the different size of yarn in the weft direction for the same cover factors. These geometrical characteristics are expected to change in the actual woven fabrics due to the yarn compression, occurring when the warp and weft yarns interlace. This geometric change will affect the liquid resistance on a fabric surface. Comparing the geometries in the theoretical and actual F_{Lab_SY} and F_{Lab_RY} will describe how the yarn interlacing influences their geometries. The structural geometry of the actual F_{Lab} could be identified through the SEM images of the prepared F_{Lab} with the yarns characterized by different roughness levels. All laboratory designed woven fabrics (F_{Lab}) were chemically treated using FS ($C_{13}H_{13}O_3F_{17}Si$) before observing structural geometries and measuring fabric contact angles.

Observation of structural geometries in actual $F_{Lab._{SY}}$ and $F_{Lab._{RY}}$ using SEM images

After creating the woven fabrics designed by the selected conditions given in Table 4.25, their structural geometries were observed through SEM images of the actual F_{Lab}. The observed geometries were compared between F_{Lab_SY1} and F_{Lab_RY1} and amongst F_{Lab_RY1} through F_{Lab_RY6}. The former comparison is to define the effect of roughness in a yarn structure on enhancing the liquid resistance of the woven fabric; the latter is to identify the highest performing structure amongst the F_{Lab_RY} varied by the different picks per inch. The picks per inch increase or decrease the void space between two adjacent weft yarns. This will assist in determining the appropriate amount of void space in a weave structure for obtaining a superoleophobic surface.

The value of geometrical parameters, the yarn diameter, $2R_y$, and the void space, p-$2R_y$, was directly obtained utilizing the SEM images of the top view for the actual $F_{Lab._{SY}}$ and $F_{Lab._{RY}}$. Each geometric value was averaged after measuring at least 5 times at the different locations on the surface of the actual $F_{Lab._{SY}}$ and $F_{Lab._{RY}}$. Then, the ratio of the void space to the yarn diameter, T, was calculated by comparing the occupancy of those values in a unit area of the plain weave. The flattening ratio, e, was also determined by comparing the major axis ‘a’ and the minor axis ‘b’. When the yarn is compressed under tension, the horizontal-direction length increases and the vertical-direction length deceases: the former and the latter refer to the major axis, a and the minor axis, b. The values of a and b were also measured directly from the SEM images of the cross-section view of the actual $F_{Lab._{SY}}$ and $F_{Lab._{RY}}$.

Geometric characteristics in actual F_{Lab_SY1} and F_{Lab_RY1}

Figure 4.24 shows the SEM images of the structural geometries constructed in the F_{Lab_SY1} and F_{Lab_RY1}. For (a) F_{Lab_SY1}, the SY was interlaced in the warp and weft directions. Under tension created between warp and weft yarns, the yarn compression occurred, leading to a decrease in the void space between adjacent warp or weft yarns. On the other hand, for (b) F_{Lab_RY1}, the RY was utilized in the weft direction and the SY in the warp direction. The RY was generated in a loosely packed structure by the protuberances created on its fiber surfaces. Also, the roughness in RY leads to an increase in the void space between yarns in a plain weave. The size and distribution of the micro-scale protuberances on the fiber surfaces played an important role when determining the amount of void space in the loosely packed yarn structure.

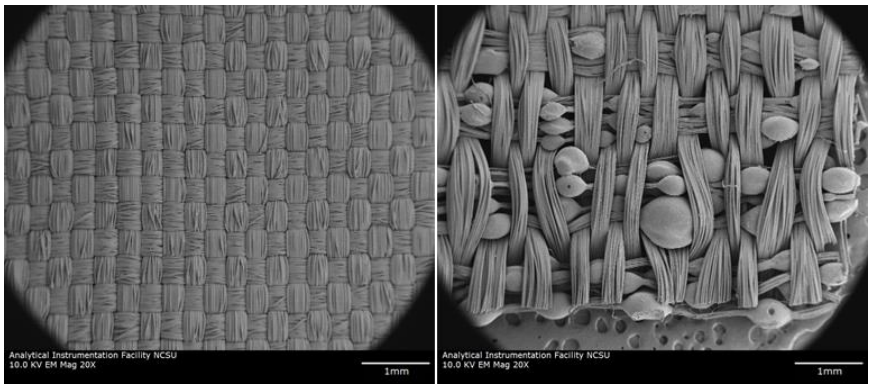

(a) (b)

Figure 4. 20 SEM images of structural geometries in FS treated woven fabric's top view: (a) F_{Lab_SY1} and (b) F_{Lab_RY1} (20X, 10KV). The length bar in each image is 1 mm.

Table 4.27 shows the geometric values of $2R_y$, $p\text{-}2R_y$, T, and e observed from the SEM images of the actual $F_{Lab._SY1}$ and $F_{Lab._RY1}$. This represents the geometric changes impacted by the different yarn structures: tightly packed and loosely packed yarn structures through the roughness created on the fiber surface.

Table 4. 27 Geometric characteristics of actual F_{Lab_SY1} and F_{Lab_RY1} (FS treated)

Fabric		$2R_{ye}$	$2R_{yp}$	p-$2R_{ye}$	p-$2R_{yp}$	T_e	T_p	T_y	e_e	e_p	e_f
$F_{Lab.}$	SY1	0.029	0.032	0.001	0.005	0.03	0.15	0.09	0.73	0.52	0.62
	RY1	0.034	0.087	0.006	0.033	0.17	0.38	0.28	0.77	0.60	0.69

Compared with the theoretical geometry, these values show that the yarns were compressed in the actual fabrics: increasing the major axis 'a' around 1.6-1.8 times for F_{Lab_SY1} and around 1.7-1.9 times for F_{Lab_RY1}. This resulted in a large decease in the void space ratio, T_e and T_p, by 85-96 % for F_{Lab_SY1} and by 63-77 % for F_{Lab_RY1}. The fabric's void space ratio, T_y, was represented by the average value of T_e and T_p. This shows that T_y decreased by around 90 % in F_{Lab_SY1} and around 70 % in F_{Lab_RY1}. The void space ratio, T_y, was maintained at the higher values in F_{Lab_RY1} than in F_{Lab_SY1}. It seems that the micro-scale roughness in a yarn prevented the closure of the spaces between the adjacent yarns under yarn compression in F_{Lab_RY1}.

Apparent contact angles (θ_{F_Md}) in FS treated actual F_{Lab_SY1} and F_{Lab_RY1} samples

The liquid resistance of the fabric surface is reflected by the different geometries between F_{Lab_SY1} and F_{Lab_RY1} in regards to the roughness and the void space. The liquid resistance was estimated via measuring the liquid contact angle on the fabric surface. The liquid droplet of dodecane on the surface of (a) F_{Lab_SY1} and (b) F_{Lab_RY1} is shown in Fig. 4.25.

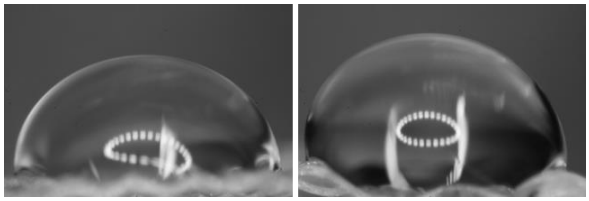

(a) (b)

Figure 4. 21 Liquid droplet of dodecane deposited on FS treated surfaces of (a) F_{Lab_SY1} and (b) F_{Lab_RY1}.

Table 4.28 shows the result of the contact angle of the dodecane, dropped on the F_{Lab} surface. The liquid contact angle in $F_{Lab.\_RY1}$ was higher than the one in F_{Lab_SY1} by around 4.4 %. However, the difference was not significant when considering the standard deviations.

Table 4. 28 Measured θ_{F_Md} of dodecane in FS treated actual F_{Lab} (˚)

Fabric		θ_{F_Md}
$F_{Lab.}$	SY1	91 ± 3
	RY1	95 ± 8

For the F_{Lab_SY1} and F_{Lab_RY1} samples, the yarn structure varied in the tightly packed structure and the loosely packed structure by the protuberances created on the fiber surfaces. This result confirmed that the micro-scale void space and roughness have an influence in creating a higher performing liquid resistant surface. Moreover, the micro-scale roughness on the fiber surfaces contributed to maintain the macro-scale void space in the fabric structure, thus, the void space ratio observed in the fabric structure of the F_{Lab_RY1} was larger than that in F_{Lab_SY1}. In the fabric structure, the void space ratio is determined by the distance between the two adjacent yarns over the yarn diameter. However, a higher contact angle is still required to drive the liquid droplet roll-off on the fabric surface, especially for any low surface tension liquid such as dodecane. As this result represented the important role of the void space for improving the liquid resistance of the fabric, the different size of the void space will be examined to identify the highest performing void space for the F_{Lab_RY}.

Geometric characteristics in actual F_{Lab_RY1} to F_{Lab_RY6}

For the F_{Lab_RY1} to the F_{Lab_RY6} samples, the size of the void space was varied by decreasing the picks per inch from K_p=14 to K_p=5 as seen in Table 4.25. As the weft directional fabric density (K_p) decreases, the void space (p-d_{yp}) becomes larger, resulting in a higher void space ratio, T_p and T_y. Figure 4.26 shows the SEM images of the F_{Lab_RY}'s top view characterized by the different void space between adjacent weft yarns. The weft directional fabric density, K_p, was lower in the F_{Lab_RY5} than in the F_{Lab_RY4}. Therefore, these top views show the larger void space in the F_{Lab_RY5} compared with that in the F_{Lab_RY4}.

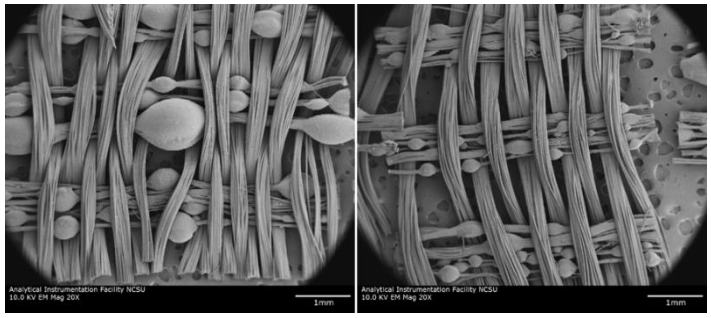

(a) (b)

Figure 4. 22 SEM images from the top view of geometries in FS treated woven fabric: (a) F_{Lab_RY4} and (b) F_{Lab_RY5} (20X, 10KV). Scale bars are 1 mm.

The geometric values were obtained from the SEM images and the void space ratio, T, and the flattening factor, e, were calculated as shown in Table 4.29. The void space, T_p, increased as the weft directional fabric density, K_p, decreased. The average void space between yarns also increased by the higher T_p. The change of the void space ratio, T_y, shows the same tendency as the predicted one in the theoretical F_{Lab_RY1} through the F_{Lab_RY6}.

Table 4. 29 Geometric characteristics of FS treated actual F_{Lab_SY} and F_{Lab_RY}

Fabric		$2R_{ye}$	$2R_{yp}$	p-$2R_{ye}$	p-$2R_{yp}$	T_e	T_p	T_y	e_e	e_p	e_f
F_{Lab}	RY1	0.034	0.087	0.001	0.033	0.17	0.38	0.28	0.77	0.60	0.69
	RY2	0.031	0.091	0.006	0.056	0.19	0.61	0.40	0.77	0.60	0.68
	RY3	0.030	0.091	0.011	0.064	0.35	0.71	0.53	0.77	0.52	0.64
	RY4	0.027	0.110	0.011	0.087	0.40	0.79	0.60	0.78	0.49	0.63
	RY5	0.031	0.078	0.013	0.109	0.41	1.40	0.91	0.85	0.44	0.65
	RY6	0.031	0.072	0.006	0.186	0.21	2.58	1.40	0.85	0.45	0.65

However, the values of the void space in the actual F_{Lab_RY} was much smaller when compared with the theoretical F_{Lab_RY}: about 70 % for F_{Lab_RY1}, 58% for F_{Lab_RY2}, 54 % for F_{Lab_RY3}, 57 % for F_{Lab_RY4}, 51 % for F_{Lab_RY5}, and 48 % for F_{Lab_RY6}. This is because of the highly compressed warp and weft yarn as seen in Fig.4.26.

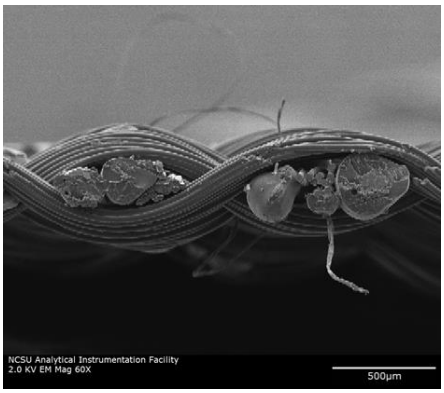

Figure 4. 23 SEM images of yarn compression in FS treated F_{Lab_RY1} (60X, 2.0KV). Scale bar is 500 μm.

The yarn compression greatly reduced the void space ratio to the yarn diameter, T_e and T_p, leading to the decrease of T_y as shown in Fig. 4.28 and Fig. 4.29. In Fig. 4.28, the warp yarn was less flattened from F_{Lab_RY1} to F_{Lab_RY6} as the picks per inch decreased. On the other hand, the weft yarn was more flattened from F_{Lab_RY1} to F_{Lab_RY6}. The assumption is that the tension between the warp and weft yarns became weak at lower picks per inch than F_{Lab_RY1}, causing the longer distance between adjacent weft yarns. This weakened tension reduced the flattening of the warp yarn, however, it increased the flattening of the weft yarn through much more

loosely packing the rough surface yarn in the larger void space between the two yarns. The tendency of the yarn flattening ratio was different for the warp yarn and weft yarn of the actual F_{Lab_RY}. In the statistical analysis using bivariate, the flattening ratio of the warp and weft yarns was negatively correlated at $P \leq 0.05$ ($0.8 \leq |r|$). The roughness generated by the interlacement of yarns is maintained by the less flattened warp or weft yarns, which is the macro-scale roughness. Therefore, the higher values will be utilized as the flattening factor of the actual woven fabrics.

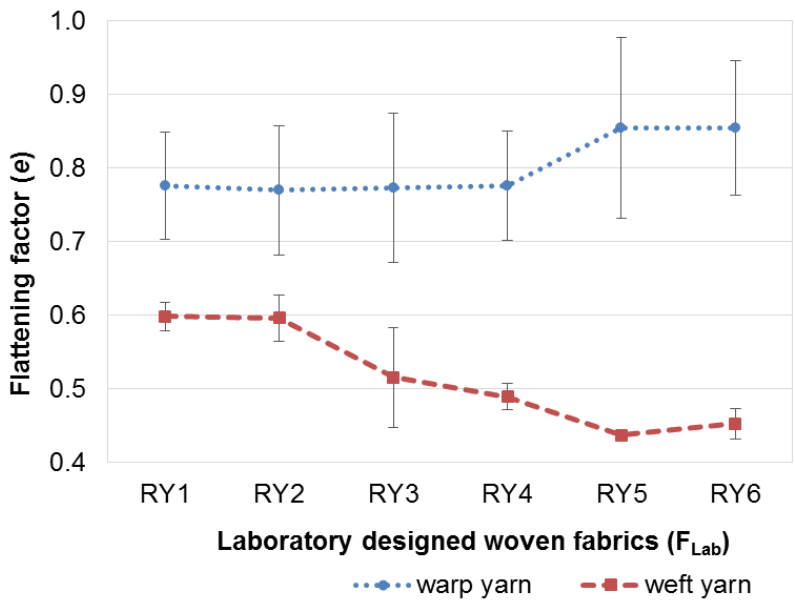

Figure 4. 24 Flattening ratio of warp (e_e) and weft (e_p) yarns in FS treated actual F_{Lab_RY1} to F_{Lab_RY6}.

The void space ratio greatly decreased in the actual F_{Lab_RY} because of the yarn flattening. However, the change of the void space ratio from F_{Lab_RY1} to F_{Lab_RY6} showed the same tendency in the theoretical and the actual F_{Lab_RY} samples. The void space ratio showed strong correlation with the yarn flattening factor of the warp and weft yarns ($0.8 \leq |r|$) at $P \leq 0.05$. The warp yarn flattening factor, e_e, was positively correlated while the weft yarn flattening factor, e_p, was negatively correlated with T_y as seen in Fig. 4.28 and Fig. 4.29.

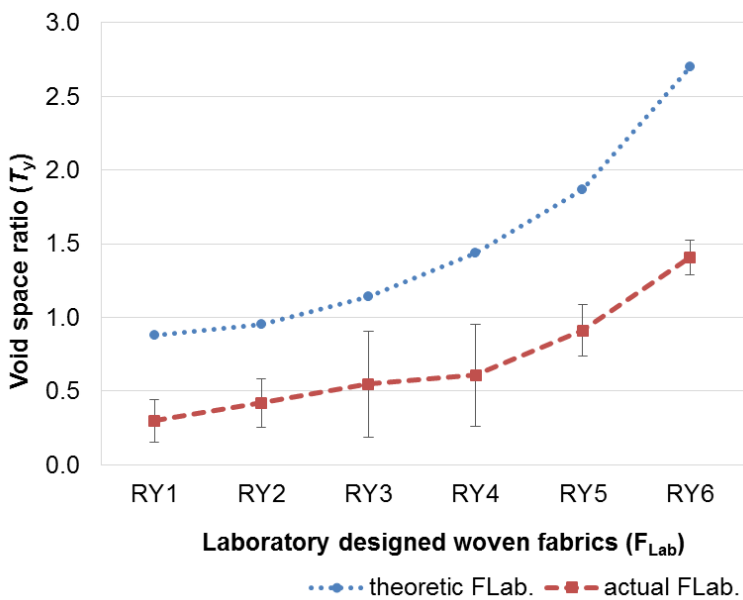

Figure 4. 25 Void space ratio (T_y) in theoretical and FS treated actual F_{Lab_RY1} to F_{Lab_RY6}.

Apparent contact angles (θ_{F_Md}) in FS treated actual F_{Lab_RY1} to F_{Lab_RY6} samples

The change of the yarn flattening and the void space ratio will influence the liquid resistance of the actual F_{Lab_RY}. In the prediction of liquid wetting behavior against the woven fabric surface using the Cassie-Baxter model developed by e and T, the fabric's apparent contact angle (θ_F) slightly increased until the yarn flattening approached around 50 % in a plain weave while the larger the void space ratio becomes, the higher θ_F. Since the yarn flattening of the actual F_{Lab_RY} occurred by less than 30 %, the apparent contact angle, θ_F, will be slightly higher compared with that when e=1. However, the yarn flattening ratio at a similar amount of around e_e=0.77 to e_e=0.85 in the F_{Lab_RY}. This means that the liquid resistance measured by the fabric's apparent contact angle, θ_F, could be compared using the void space ratio, T_f.

The oil resistance of the F_{Lab_RY}'s surface was estimated by measuring the apparent contact angle of dodecane dropped on the surface of the FS treated F_{Lab_RY}. Figure 4.30 shows the deposition of the dodecane droplet. It is observed that the shape of the droplet changes on the different geometric surface characterized by the size of void space. The more spherical shape will result in the higher oil resistance of the fabric surface.

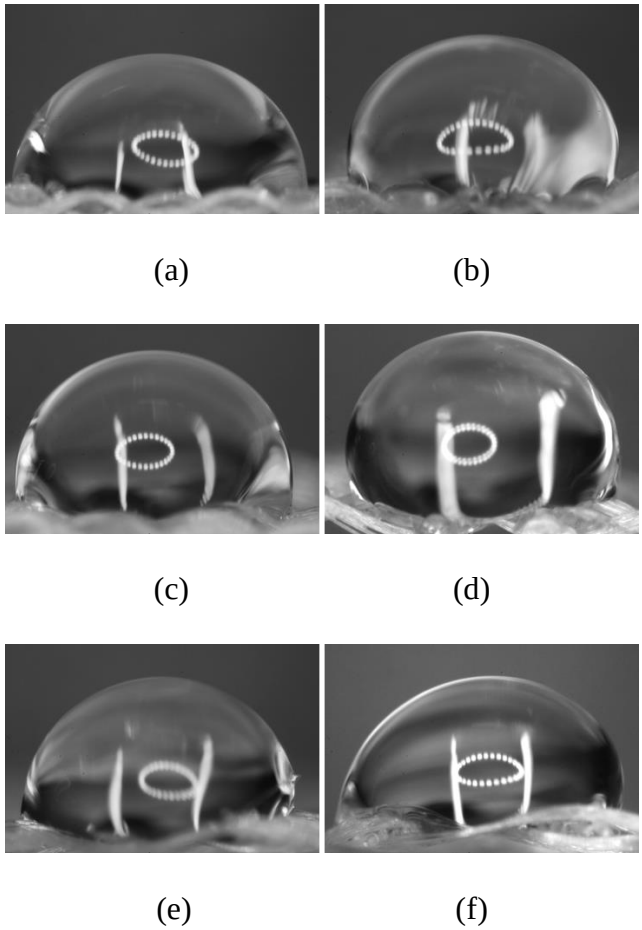

Figure 4.26 Liquid droplet of dodecane deposited on FS treated surfaces: (a) F_{Lab_RY1}, (b) F_{Lab_RY2}, (c) F_{Lab_RY3}, (d)F_{Lab_RY4} (e)F_{Lab_RY5}, and (f)F_{Lab_RY6}.

Table 4.30 shows the measured apparent contact angles of dodecane on the actual fabric surfaces. This result shows that θ_F increased from F_{Lab_RY1} to F_{Lab_RY4} as the void space ratio, T_y, increases. When the void space ratio was up to 0.6, θ_F increased by about 11 % in F_{Lab_RY4} compared to in $F_{Lab\_RY1,}$ represented the highest performance for the liquid resistance amongst

F_{Lab_RY1} to F_{Lab_RY6}. This confirms that the void space ratio of T_y=0.6 is the optimum value for this rough surface yarn (RY).

Table 4.30 Measured θ_{F_Md} of dodecane in FS treated actual F_{Lab_RY}.

Fabric		θ_{F_Md} (°)
F_{Lab}	RY1	95 ± 8
	RY2	97 ± 3
	RY3	98 ± 5
	RY4	105 ± 8
	RY5	97 ± 10
	RY6	98 ± 6

The statistical analysis including the variables of F_{Lab_RY1} to F_{Lab_RY6} presented that the correlation of θ_{F_Md} with the warp yarn flattening ratio, e_e, is significant ($F_{2,3}$=15.726, $P \leq 0.05$), however, the correlation with the void space ratio, T_y, was not significant. On the other hand, when the variable included F_{Lab_RY1} to F_{Lab_RY4}, the correlation of θ_{F_Md} was significant for e_e ($F_{2,2}$=21.457, $P \leq 0.05$) and T_y ($0.8 \leq |r|$, $P \leq 0.05$). The difference of these statistical analyses could be explained by the decrease of θ_{F_Md} in F_{Lab_RY5} and F_{Lab_RY6}.

θ_{F_Md} decreased in F_{Lab_RY5} and F_{Lab_RY6} to a contact angle less than in F_{Lab_RY4}. The reason is attributed to the void space distributed in the F_{Lab_RY5} and F_{Lab_RY6}. The size of some void spaces in those fabrics were close to the maximum void space size identified by the definitions of the Laplace pressure and the Capillary pressure for dodecane. This means that the liquid

droplet is not able to be supported by the liquid-vapor interface created in the void space even if its size is not overwhelmed by the maximum void space size. This result emphasizes the importance of designing the void space smaller than the maximum void space for a liquid to enhance the liquid resistance of a fabric surface.

4.4 Comparison of measured and predicted liquid resistance in theoretical and actual geometries of F_{Lab}

For the laboratory designed woven fabrics, the geometries were focused on creating the different scales (micro-scale and macro-scale) of roughness in a plain weave: micro-scale roughness in a yarn structure and macro-scale roughness in a fabric structure. The liquid resistance on the fabric surface was examined by two variables: the first is the presence of micro-scale roughness in the woven fabric structure and the second is the macro-scale void space varied by the different fabric densities. The low fabric density increases the void space, as the fabric structure become more loosely interlaced.

To define the impact of each variable on the liquid resistance, the apparent contact angles were measured in the actual F_{Lab}. Moreover, the measured apparent contact angles were compared with the predicted apparent contact angles in the theoretical and actual geometries of the F_{Lab}. The comparison will contribute to justifying the newly developed Cassie-Baxter models for the lenticular yarn, accounting for the yarn compression.

Prediction of θ_y using theoretical and actual geometries of yarn structure in FS treated F_{Lab_SY} and F_{Lab_RY}

The micro-scale roughness was created via using the rough surface yarn in which the bell-shape protuberances at the micro-scale were developed on the fiber surfaces. The bell-shape protuberances also generated the void spaces in the yarn structure at the micro-scale.

Generating the void space transformed the tightly packed yarn structure to a loosely packed yarn structure, in which the void space was created between two adjacent fibers. In the actual yarn, the tightly packed yarn is represented by the smooth surface yarn (SY): the loosely packed yarn by the rough surface yarn (RY).

In the theoretical geometry of the loosely packed yarn, the parameter, $2R_f$ and p_f refer to a fiber diameter and a fiber spacing in a unit structure. The fiber spacing includes the void space, p_f-$2R_f$. The void space ratio, T_f, was obtained by comparing d_{f2}-d_{f1} to d_{f1}. Equation 2.76 was utilized to determine the fiber spacing, d_{f2}, for the given RY diameter calculated using the linear density of the RY. In the actual geometry of the SY and RY, the values of parameters were directly obtained from the SEM images. The values of parameters, d_{f1}, d_{f2}, d_{f2}-d_{f1}, and T_f were presented as shown in Table 4.31.

Table 4. 31 Predicted θ_y using theoretical and actual geometries of yarn structures in FS treated F_{Lab}

Fabric			Yarn	$2R_f$ (cm)	P_f (cm)	p-$2R_f$ (cm)	T_f	θ_e(˚)	θ_y (˚)
Theoretical	F_{Lab}	SY	warp	0.0026	0.0026	0	0.00	65	41
			weft						
		RY	warp	0.0026	0.0026	0	0.00		
			weft	0.0026	0.0072	0.0046	1.76		111
Actual	F_{Lab}	SY	warp	0.0031	0.0035	0.0004	0.13		56
			weft						
		RY	warp	0.0031	0.0038	0.0007	0.24		65
			weft	0.0031	0.0073	0.0042	1.35		105

The parameter values of the theoretical and actual geometries were utilized to predict the yarn's apparent contact angle, θ_y, in the Cassie-Baxter equation characterized by the void space ratio to the fiber diameter, T_f, and the Young contact angle, θ_e. θ_e was obtained from the FS treated nylon film by dropping a liquid droplet on its surface: it was 65˚ for dodecane. This contact angle indicates the liquid resistance of the smooth nylon surface against dodecane with a low surface tension. The contact angle, θ_y, in the SY and RY show the impact of the nylon yarn's structure on changing the liquid resistance.

By the different T_f, the yarn's contact angle, θ_y, was determined in the theoretical and actual yarn geometries. For the SY, when T_f=0 in the theoretical yarn structure, θ_y=41˚, and when T_y=0.13 and 0.24 in the actual yarn structures, θ_y=56˚ and θ_y=65.2˚, respectively. For the RY, when T_f=1.76 in the theoretical geometry, θ_y=111.4˚, and when T_f=1.35 in the actual geometry, θ_y=104.6˚. The RY geometry showed the higher contact angle, θ_y, than the Young contact angle, θ_e, while θ_y in the SY geometry was lower than θ_e. This is because the higher void space between fibers reduces the ratio of the liquid contact area to a solid surface against the liquid contact area to vapor. If a liquid droplet is placed on the RY surface, the liquid-vapor interface will be generated and prevent the liquid from penetration into the yarn structure.

Comparison of predicted and measured θ_F in FS treated F_{Lab_SY} and F_{Lab_RY}

To predict the fabric's apparent contact angle, the Cassie-Baxter models were developed employing the flattening factor, *e*, and the yarn void space ratio, T_y, as well as the yarn contact

angle, θ_y. The predicted and measured values of e and T_y in the theoretical and actual F_{Lab} are presented in Table 4.32 below.

Table 4. 32 Selected e_e and T_y in theoretical and actual geometries of FS treated F_{Lab_SY} and F_{Lab_RY}

Fabric		Theoretical		Actual	
		e_e	T_y	e_e	T_y
F_{Lab}	SY1	1.00	0.88	0.73	0.09
F_{Lab}	RY1	1.00	0.88	0.77	0.28
	RY2	1.00	0.96	0.77	0.40
	RY3	1.00	1.14	0.77	0.53
	RY4	1.00	1.44	0.78	0.60
	RY5	1.00	1.86	0.85	0.91
	RY6	1.00	2.70	0.85	1.40

The predicted contact angles, θ_{F_Pd}, were obtained from the theoretical geometry and the actual geometry of the woven fabric, F_{Lab_SY1} and F_{Lab_RY1} as shown in Table 4.33. For the theoretical F_{Lab_RY1}, the θ_{F_Pd} equals to 110˚, which is about 16 % higher than the θ_{F_Md} (95.2˚) in the actual geometry. In the prediction using the actual geometric values of e_e and T_y, the θ_{F_Pd} was 93˚, which is about 2 % lower than the θ_{F_Md} (95.2˚).

This result indicates that it is possible to obtain the θ_{F_Pd} much closer to the θ_{F_Md} when the prediction considers the geometrical changes in the actual woven fabric. The yarn compression

is a critical change of the geometry impacting the liquid resistance of the fabric surface through decreasing *e* and *T*. This provides the justification of the newly developed Cassie-Baxter model by *e* and *T*.

Table 4. 33 Predicted θ_{F_Pd} and measured θ_{F_Md} in FS treated F_{Lab_SY1} and F_{Lab_RY1} for dodecane (˚)

Fabric			θ_{y_Pd}	θ_{F_Pd}	θ_{F_Md}
Theoretical	F_{Lab}	SY1	41	-	-
		RY1	111	110	-
Actual	F_{Lab}	SY1	56	-	91 ± 3
		RY1	105	100	95 ± 8

Comparison of θ_{F_Pd} and θ_{F_Md} in FS treated F_{Lab_RY1} through F_{Lab_RY6}

The F_{Lab_RY} was varied with the different size of the void space from F_{Lab_RY1} to F_{Lab_RY6} to identify the highest performing void space for the liquid of dodecane. For the F_{Lab_RY}, the contact angle, θ_F, was predicted using the Cassie-Baxter models for the woven fabric characterized by θ_y, or θ_y and *e*, or θ_y, *e*, and *T*. Table 4.31 shows the values of *e* and *T* used for predicting the contact angles. The Cassie-Baxter model using θ_y for the prediction assumed that the yarn in a woven fabric construction is circular. The other Cassie-Baxter models using θ_y and *e*, or θ_y, *e*, and *T* were extended based on Shanahan and Hearle's lenticular model of a woven fabric.

Table 4.34 shows the predicted θ_{F_Pd} and measured θ_{F_Md} in the F_{Lab_RY1} through F_{Lab_RY6} for dodecane for the two different yarn contact angle: θ_y=111.4˚ and θ_y=104.6˚. Each θ_y was predicted in the theoretical yarn structure and the actual yarn structure, respectively. The θ_{F_Pd} when θ_y=111.4˚ was compared with the one when θ_y=104.6˚ obtained the Cassie-Baxter model by θ_y, e, and T.

Table 4. 34 Predicted θ_{F_Pd} and measured θ_{F_Md} in F_{Lab_RY} for dodecane (˚)

Fabric		(1) θ_{F_Pd} (θ_y=111.4˚)	(2) θ_{F_Pd} (θ_y=104.6˚)			(3) θ_{F_Md}
		θ_y, e, T	θ_y	θ_y, e	θ_y, e, T	
$F_{Lab.}$	RY1	109	105	100	98	95 ± 8
	RY2	113	105	99	102	97 ± 3
	RY3	116	105	99	106	98 ± 5
	RY4	118	105	99	108	105 ± 8
	RY5	123	105	102	114	97 ±10
	RY6	129	105	102	122	98 ± 6

The predicted contact angles when θ_y=104.6˚ were much closer to the measured contact angles, θ_{F_Md}, for the F_{Lab_RY} as shown in Fig. 4.27. When θ_y=104.6˚, the difference between the θ_{F_Pd} and the θ_{F_Md} was around 2 % to 8 % in the F_{Lab_RY1} through the F_{Lab_RY4}, however, it increased to about 14 % to 18 % when θ_y=111.4˚. This result indicates that the model considering the actual geometry can predict the contact angle (θ_F) more accurately.

In addition, the θ_{F_Pd} was compared to the models using only θ_y, or θ_y and e when θ_y=104.6˚ as shown in Fig. 4.28. The θ_{F_Pd} predicted using only θ_y did not reflect the different size of the

void spaces and the yarn flattening in the F_{Lab_RY1} through F_{Lab_RY6}. Another model using θ_y and e accounted for the yarn flattening for the θ_{F_Pd}, however, it could not reflect the impact of the void space for the θ_{F_Pd}. Amongst three models, only the last model characterized by θ_y, e, and T predicted the tendency of the θ_{F_Md} most accurately.

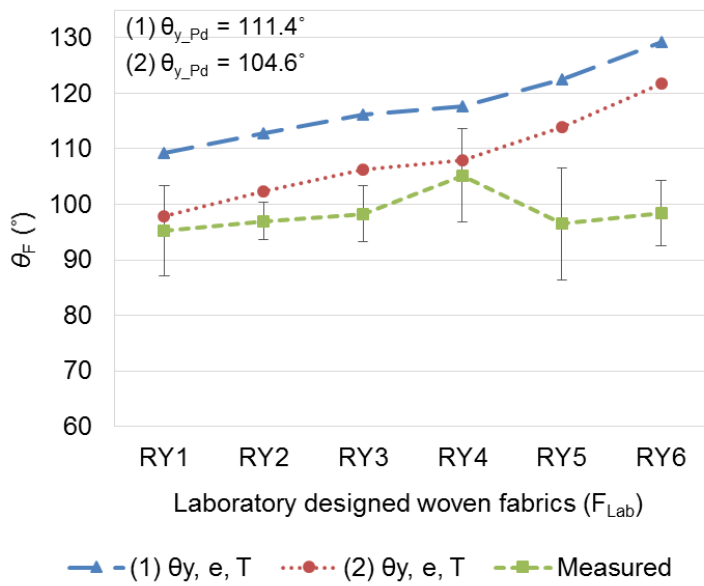

Figure 4. 27 θ_{F_Pd} and θ_{F_Md} in theoretical and actual geometries of F_{Lab_RY}.

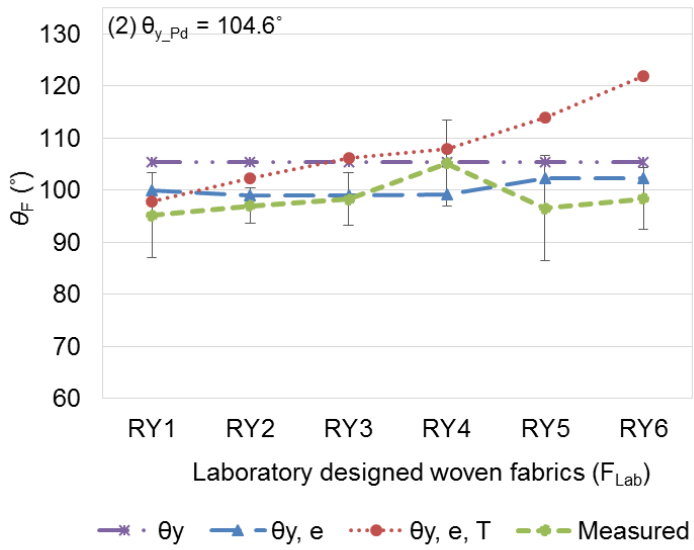

Figure 4. 28 Tendency of θ_{F_Pd} and θ_{F_Md} when θ_{y_Pd}=104.6˚.

However, there are exceptions in the F_{Lab_RY5} and F_{Lab_RY6}: the θ_{F_Md} shows the opposite tendency unlike in the F_{Lab_RY1} through F_{Lab_RY4}. This is because the F_{Lab_RY5} and F_{Lab_RY6} were woven at too low a pick per inch level for the size of the macro-scale void space smaller than the maximum void space (D=0.14 cm) for dodecane. The maximum void space (D=0.14 cm) of dodecane was defined by the definition of the Laplace pressure and the Capillary pressure expressed by the liquid properties: $D \leq 4\ell^2_{cap}$. It indicates that a dodecane droplet will penetrate into a weave structure when the created void space between two yarns deviates from the identified range ($D \leq 0.14$ cm). The F_{Lab_RY5} and F_{Lab_RY6} included the void spaces close to or larger than 0.14 cm. It is expected that the distributed void spaces ($D \approx$ or > 0.14 cm) would cause the liquid droplet state transiting into the Wenzel state or penetrating into the fabric

structure through moving the liquid-vapor interface downward. This explains the reason for the decrease of the fabric contact angles in the F_{Lab_RY5} and F_{Lab_RY6} at the larger void spaces. These exceptional fabric contact angle tendencies in these two fabrics verified modeling the range of the void space ($D \leq 4\ell^2_{cap}$) for a liquid.

Chapter 5 Conclusion

Woven fabrics consist of different scales of structures: nanoscale in fiber, microscale in yarn, and macroscale in fabric. The multiscale structure plays an important role in obtaining an oil repellent surface by creating various sizes of void spaces and increasing the surface roughness. Therefore, this study focused on designing the woven structural geometry, impacting greatly the liquid resistance of fabrics. For that, it is assumed that the fabric surface energy is low enough relative to the liquid surface tension. Priority was given to the two characteristics of roughness and the amount of void space as they contribute to reducing the liquid contact area to the woven fabric surface. It was expected that the air in the void space supports the liquid droplet in floating on the fabric surface.

The roughness and the void space can be affected by the woven structure, the fabric density (picks or ends per inch), and the yarn compression. Three woven structures were selected via the market review of high performance clothing used for protective wear, military uniform, outdoor wear, etc. The structures include plain, 2/1 twill, and 2/2 basket. When developing the Cassie-Baxter model of those woven structures, the formula has been extended using the yarn flattening factor, e, and the void space ratio to the yarn diameter, T. The formula is the Cassie-Baxter equation of the lenticular cross-section yarn model. By utilizing the Cassie-Baxter equation, the liquid wetting behaviors of three weave structures were predicted under different conditions having varied e and T. The newly developed Cassie-Baxter models are taking into account the effect of the yarn compression and the void space. This consideration in the

lenticular cross-section yarn model is comparable with the circular cross-section yarn model. The circular cross-section yarn models have also been developed for three woven structures. However, they only account for the liquid property determining the Young contact angle on a smooth solid surface, without consideration of the yarn compression or the void space in an actual woven structure. Therefore, the lenticular cross-section yarn models were expected to predict the liquid wetting behavior more accurately and agree with the one of the actual fabric. Then, these models would contribute to identifying the best-performing weave structure and its optimum geometry.

The prediction using the circular cross-section model showed that there is a specific value of the Young contact angle to obtain the higher fabric's apparent contact angle than the applied Young contact angle; 109˚ for plain and 2/1 twill, and 105˚ for 2/2 basket structures. It indicates that the Young contact angle (θ_e) should be high enough to obtain the higher fabric's apparent contact angle than 0˚ and θ_e ($\theta_F > 0˚$, $\theta_F > \theta_e$). The Young contact angle does not consider the local structure of a solid surface. Therefore, the low Young contact angle provides the reasonable justification that multiscale structures should be developed by creating nano or micro scale roughness in a fiber or a yarn structure. If the woven fabric is developed by the multiscale structures, the Young contact angle could be substituted into the Cassie-Baxter equation by the fiber's apparent contact angle or the yarn's apparent contact angle for a given liquid. On the other hand, in the region of $\theta_F > \theta_e$, the contact angle's enhancement ratio by the different Young contact angles is higher in the plain structure compared to 2/1 twill and 2/2

basket weave. The higher angle in plain weave is provided by its short float length in a unit area, leading to the lower contact area of a liquid on the plain woven fabric surface.

The first Cassie-Baxter model of the lenticular cross-section yarn has been developed with the yarn flattening factor, e. When e=1 (a=b), the predicted result showed that the minimum Young contact angle (θ_e) is higher in order to obtain $\theta_F > \theta_e$ in the lenticular Cassie-Baxter model than in the circular Cassie-Baxter model. The plain and 2/1 twill structures were approximately 109˚, while 2/2 basket structure was around 105˚. The enhancement ratio of the contact angle has been observed at its highest in the plain structure as shown in the circular Cassie-Baxter model. When $e < 1$ ($a > b$), the flattening factor decreases while the major axis, a, increases. To examine the impact of the yarn flattening on a liquid wetting behavior, the four Young contact angles have been chosen. They were 109˚, 122˚, 150˚, and 170˚. The result showed that the fabric's apparent contact angle increases slightly at first, and then decreases when the flattening ratio reaches a specific point. The fabric's apparent contact angle increased or decreased more greatly when the Young contact angle was low. Also, the tendency of the fabric's apparent contact angle to change was different for the three woven fabric structures. While the 2/1 twill was affected by flattening more greatly, the 2/2 basket was relatively stable to the yarn flattening. The plain structure tended to have the largest apparent contact angle when the Young contact angle was high enough. However, at θ_y=122˚, the highest fabric apparent contact angle showed a transition from plain to 2/2 basket at a yarn flattening of 44%, then

from 2/2 basket to 2/1 twill at 72%. When θ_y=150 and 170, the plain structure showed the highest apparent contact angle until the yarn flattening reached 80% and 88%, relatively.

The second Cassie-Baxter model of the lenticular cross-section yarn has been developed using *e* and *T*. The parameter, *T*, refers to the ratio of the void space to the yarn diameter. The void space ratio, *T*, was 0.75 at the maximum cover factor, having the maximum fabric density (picks or ends per inch). When *e*=1 and *T*=0.75, the prediction showed that the different void space ratio contributes to changing the fabric contact angle. When the Young contact angle was varied from 30˚ to 180˚, each woven structure has the minimum Young contact angle to obtain the fabric's apparent contact angle greater than 0˚ ($\theta_F > 0˚$). The Cassie-Baxter model for the lenticular yarn is also able to depict the circular cross-section yarn when the flattening ratio is equal to 1 (*e*=1). When compared with the circular yarn's Cassie-Baxter model, this lenticular cross-section yarn model required the lower minimum Young contact angle for $\theta_F >$ 0˚ and $\theta_F > \theta_e$. It indicates that the void space enhances the liquid resistance of the woven fabric.

In the second Cassie-Baxter equation using *e* and *T*, *T* has been varied through decreasing the fabric density in the weft direction (*e*=1, *T* > 0.75). As the fabric density decreases, the void space between yarns increases steeply. When the reduction ratio reaches 30%, it obtains twice the void space at the maximum fabric density. When it is 50%, the void space increases over three times. After the 50% reduction of fabric density, the void space begins to increase much more steeply compared to the void space at the maximum density.

When e=1, T > 0.75, the larger the void space ratio becomes, the more steeply the fabric contact angle increases. However, when the Young contact angle is over 150˚, the impact of the void space decreases. Thus, the fabric contact angle steadily changes upon increasing the void space. The minimum Young contact angle also decreases, which is required for $\theta_F > 0^\circ$ and $\theta_F > \theta y$ in the lenticular model. For $\theta_F > 0^\circ$, the minimum Young contact angle for having a finite θ_F decreases by 38% in plain, 37% in 2/1 twill, and 30% in 2/2 basket for fabrics that have 70% of the maximum fabric density. The required minimum Young contact angle reduces by 55% in plain, 52% in 2/1 twill, and 51% in 2/2 basket for 50% of the maximum fabric density. The plain and 2/1 twill structures decrease in the same ratio, however, the 2/2 basket structure shows a much lower reduction in the minimum yarn contact angle.

The lenticular yarn model re-expressed using 'T' identified the impact of the void space in the woven structures. The results confirmed that the void space strongly influences the increased or decreased fabric's liquid resistance. However, it also requires appropriate construction of the void space for a given liquid.

Most of all, the sagging phenomenon should be considered because it distorts the vapor-liquid interfacial line of the liquid droplet into the rough structure. The distortion is the critical reason the liquid droplet penetrates into the nano-, micro-, or macroscale structure of the fabric. When the liquid is distorted downward, it generates the sagging height, h, and the sagging angle, $\delta\theta$. If the sagging height, h_1, becomes equal to the depth of the protuberance, h_2, leading the nano-,

micro-, or macroscale roughness, the liquid will touch down to the bottom and fill the void space. This transformed from the Cassie-Baxter state into the Wenzel state of the liquid.

The distortion depends on the distance between adjacent protuberances in the case of a given liquid. This points out that the maximum void space, D, needs to be defined to prevent the penetration in the designed geometry. The range of void space was identified using the definitions of the Laplace pressure and the Capillary pressure of the liquid. When developing the range, it accounted for the liquid properties of the surface tension, γ, and the liquid density, ρ, and the geometrical parameters of the radius in the curvature of the liquid droplet, R, and the capillary height, h. The result indicated that the distance, D, should be equal or less than $4\ell^2_{cap}$.

To verify the lenticular cross-section yarn model and the maximum distance range of the void space, the actual fabric testing was conducted using the collected commercial woven fabrics, the NCSU manufactured woven fabrics in the facility of the College of Textiles (CoT), and the laboratory designed woven fabrics with the smooth surface yarn (SY) and the rough surface yarn (RY). All fabrics were chemically modified with FS ($C_{13}H_{13}O_3F_{17}Si$) to reduce the fabric surface tension. Through the evaluation of the commercial woven fabrics and the NCSU manufactured woven fabrics, it was determined that a plain weave is the most efficient structure amongst the woven structures such as 2/2 twill, 2/2 basket, weft rib, etc. This result proved that the lenticular cross-section yarn model was appropriately designed to predict the

liquid resistance of the woven fabric surface, defining the effective woven structures. In addition, the performance evaluation in those actual fabrics provided the highest performing geometry for the plain weave by the cover factor, K. In assuming the same fabric density (ends or picks per cm or inch) in the actual and theoretical woven fabric, the cover factors (K_e=14, K_p=16, K_F=22) were obtained in the theoretical geometry using the yarn diameter, 2R, predicted using the yarn density.

Those cover factors in the theoretical geometry determined the theoretical geometry of the laboratory designed woven fabric, F_{Lab}. The cover factors ranged over K_e=16, K_p=14, and K_F=22 for the F_{Lab}. The SY and RY were inserted as a weft or filling yarn for the F_{Lab_SY1} and F_{Lab_RY1}, respectively, to define how the liquid resistance is impacted by the roughness in a yarn structure. The results describe that the micro-scale protuberances on fiber surfaces created void spaces in the yarn structure. This transformed the tightly packed yarn structure to the loosely packed yarn structure. The apparent contact angle of dodecane measured in each fabric geometry verified that the void space importantly contributes to improving the oil resistance of the woven fabric surface.

The varied void spaces in the F_{Lab_RY1} through F_{Lab_RY6} provided the highest performing geometry in regards to the distance between adjacent yarns. The apparent contact angles (θ_{F_Md}) measured in the F_{Lab_RY} increased as the void space became larger from the F_{Lab_RY1} to the F_{Lab_RY4}. However, the contact angle began to decrease in the F_{Lab_RY5} and F_{Lab_RY6}. This

tendency was attributed to the existence of the void space slightly smaller, equal, or larger than the maximum void space, D, of dodecane ($D_y \leq 0.14$ cm). This result justified the predicted range of the maximum void space for dodecane, $D_y \leq 4\ell^2_{cap}$.

Moreover, the measured contact angle, θ_{F_Md}, was compared with the predicted contact angle, θ_{F_Pd}, using the theoretical and actual geometry of the F_{Lab_RY}. The contact angle, θ_{F_Pd}, was much closer to the measured one, θ_{F_Md}, when it was predicted taking into consideration the yarn compression in the Cassie-Baxter model. Between the Cassie-Baxter model developed by θ_y, and e or θ_y, e and T, the latter one predicted the contact angle, θ_F, most accurately: the tendency of θ_{F_Md} was almost the same with θ_{F_Md} from the F_{Lab_RY1} to the F_{Lab_RY4}. This result verified that the change of the void space ratio impacts the liquid resistance as well as the yarn flattening. At the same time, this proved the accuracy of the newly developed Cassie-Baxter model and the equation characterized by θ_y, e and T for predicting θ_F.

This study contributed to identifying the optimum geometries improving the liquid resistance, especially for oil. The modeling for prediction and the actual testing validated the hypotheses that the multi-scale roughness creates the void spaces at a different scale and these spaces will play a critical role in improving the oil resistance of a fabric surface in reaching superoleophobicity. From the results in the theoretical and actual geometry, these geometric conditions are suggested to create the structural geometry for superoleophobicity: plain for a

weave structure, $h_2 > h_1$ in the sagging, $D_y \leq 4\ell^2_{cap}$ for the void space range, and the micro-scale void space in a rough surface yarn structure.

Chapter 6 Future work

This study was conducted to create high performance woven structure impacting superoleophobicity, repelling a liquid with low surface tension such as oil. The result defined the influence of structural geometries of the woven fabrics through developing the theoretical modeling and the actual experiments. However, the fabric surface requires further modification to obtain a superoleophobic surface, which can allow liquid droplet to roll off. The modification could be conducted via generating the nano-scale protuberances on a fiber surface for improving the multi-scale structures in the woven fabric. Another way, using a linen blended yarn can be considered to weave a fabric in a weft or warp direction. In the experiment using the commercial fabrics, the woven fabric constructed with the linen blended yarn performed well for the liquids with low surface tension compared to the fabric woven by nylon or cotton. The reason is assumed to be the effect of the inherent roughness ofthe flax fiber's surface. Therefore, it is expected that the woven fabric will obtain the superoleophobic surface showing the contact angle over 150˚ for oil if the linen blended yarn is used as the warp or weft yarn.

In this study, micro-scale protuberances created on fiber surfaces contributed to improving the roughness and the void space in yarn structure and also the woven fabric structure. However, an effect of yarn twisting remains as a concern because it could greatly decrease the void spaces in the yarn structure. Also, the newly developed model needs to be verified for other liquids with low surface tension.

REFERENCES

1. Lee, H. J.; Michielsen, S. Preparation of superhydrophobic surface using lotus effect. Abstracts of the Fiber Society Symposium. **2006**, *11*, 33-4.

2. Lee, H. J. Design of artificial lotus leaves using nonwoven fabric. *J. Mater. Sci.* **2009**, *44*, 4645-52.

3. Hoefnagels, H.; Wu, D.; de With, G; Ming, W. Biomimetic superhydrophobic and highly oleophobic cotton textiles. *Langmuir.* **2007**, 23, 13158-63.

4. Shirtcliffe, N. J.; McHale, G.; Atherton, S.; Newton, M. I. An introduction to superhydrophobicity. *Adv. Colloid Interface Sci.* **2010**, 16, 124-38.

5. Bhat, N. V.; Netravali, A. N.; Gore, A. V.; Sathianarayanan, M. P.; Arolkar, G. A.; Deshmukh, R. R. Surface modification of cotton fabrics using plasma technology. *Text. Res. J.* **2011**, 81, 1014-26.

6. Bhushan, B. Biomimetics: Lessons from nature–an overview. *Philosophical Transactions of the Royal Society A: Mathematical, Physical and Engineering Sciences* **2009**, 367, 1445-86.

7. Bahners, T.; Textor, T.; Opwis, K.; Schollmeyer, E. Recent approaches to highly hydrophobic textile surfaces. *Journal of Adhesion Science & Technology* **2008**, 22, 285-309.

8. Bhushan, B.; Jung, Y. C.; Koch, K. Self-cleaning efficiency of artificial superhydrophobic surfaces. *Langmuir* **2009**, 25, 3240-8.

9. Quere, D.; Reyssat, M. Non-adhesive lotus and other hydrophobic materials. *Phil. Trans. R. Soc. A.* **2008**, 366, 1539-56.

10. Tuteja, A.; Choi, W.; McKinley, G. H.; Cohen, R. E.; Rubner, M. F. Design parameters for superhydrophobicity and superoleophobicity. *MRS Bull.* **2008**, 33, 752-8.

11. Tuteja, A.; Choi, W.; Ma, M.; Mabry, M. J.; Mazzella, A. S. A. Designing superoleophobic surfaces. *Science* **2007**, 318, 1618-22.

12. Xu, B.; Cai, Z.; Wang, W.; Ge, F. Preparation of superhydrophobic cotton fabrics based on SiO_2 nanoparticles and ZnO nanorod arrays with subsequent hydrophobic modification. *Surf. Coat. Technol*. **2010**, 204, 1556-61.

13. Liu, Y.; Tang, J.; Wang, R.; Lu, H.; Li, L.; Kong, Y.; Qi, K.; Xin, J. H. Artificial lotus leaf structures from assembling carbon nanotubes and their applications in hydrophobic textiles. *J. Mater. Chem.* **2007**, 11, 1071-8.

14. Kesting, W.; Bahners, T.; Schollmeyer, E. Controlled structuring of polymer surfaces by UV-laser irradiation. *Appl. Surf. Sci.* **1990**, 46, 326-9.

15. Zhang, H.; Lamb, R. N. Superhydrophobic treatment for textiles via engineering nanotextured silica/polysiloxane hybrid material onto fibres. *Surface Engineering* **2009**, 25, 21-4.

16. Erasmus, E.; Barkhuysen, F. A. Superhydrophobic cotton by fluorosilane modification. *Indian Journal of Fibre & Textile Research* **2009**, 34,377-9.

17. Hayn, R.; Owens, J.; Boyer, S.; McDonald, R.; Lee, H. Preparation of highly hydrophobic and oleophobic textile surfaces using microwave-promoted silane coupling. *J. Mater. Sci.* **2011**, 46, 2503-9.

18. Lee, H. J.; Owens, J. R. Metastable superoleophobic NyCo using fluorosilane. Abstracts of the Fiber Society Symposium **2009**, 10, 48-.

19. Zhao, H.; Law, K. Y. Directional self-cleaning superoleophobic surface. *Langmuir* **2012**, 28, 11812-11818

20. Bhushan, B.; Jung, Y. C. Natural and biomimetic artificial surfaces for superhydrophobicity, self-cleaning, low adhesion, and drag reduction. *Prog. Mater. Sci.* **2011**, 56, 1-108.

21. Eadie, L., Ghosh, T. K. Biomimicry in textiles: Past, present and potential. An overview. *J. Roy. Soc. Interf.* **2011**, 8, 761-75.

22. Lee, H. J.; Michielsen, S.; Du, J. Self-cleaning textile surfaces. Abstracts of the Fiber Society Symposium **2008**, 10, 56.

23. Koch, K.; Bhushan, B.; Barthlott, W. Multifunctional surface structures of plants: An inspiration for biomimetics. *Prog. Mater. Sci.* **2009**, 54,137-78.

24. Koch, K.; Bhushan, B.; Barthlott, W. Diversity of structure, morphology and wetting of plant surfaces. *Soft. Matter.* **2008**, 4, 1943-63.

25. Kota, A. K.; Li, Y.; Mabry, J. M.; Tuteja, A. Hierarchically structured superoleophobic surfaces with ultralow contact angle hysteresis. *Adv. Mater.* **2012**, 24, 5838-5843.

26. Law, K.; Zhao, H.; Park, K. Design parameters for "Robust" superoleophobicity surfaces. *Nanotech* **2012**, 1, 656-659.

27. Michael, N.; Bhushan, B. Hierarchical roughness makes superhydrophobic states stable. *Microelec. Eng.* **2007**, 84, 382-6.

28. Neinhuis, C.; Barthlott, W. Characterization and distribution of water-repellent, self-cleaning plant surfaces. *Ann. Bot.* **1997**, 79, 667-77.

29. Nosonovsky, M. Multiscale roughness and stability of superhydrophobic biomimetic interfaces. *Langmuir* **2007**, 23, 3157-61.

30. Nosonovsky, M.; Bhushan, B. *Multiscale dissipative mechanisms and hierarchical surfaces: Friction, superhydrophobicity, and biomimetics.* Springer, 2008.

31. Nosonovsky, M, Bhushan B. Roughness-induced superhydrophobicity: A way to design non-adhesive surfaces. Journal of Physics: Condensed Matter 2008;20(22):225009.

32. Nosonovsky, M.; Bhushan, B. Hierarchical roughness optimization for biomimetic superhydrophobic surfaces. *Ultramicroscopy* **2007**, 107, 969-79.

33. Saraf, R. Superhydrophobic and superoleophobic nonwoven fabrics. M. S. Thesis, North Carolina State University, Raleigh, NC, 2011.

34. Burtovyy, O.; Klep, V.; Chen, H. C.; Hu, R. K.; Lin, C. C.; Luzinov, I. Hydrophobic modification of polymer surfaces via "grafting to" approach. *J. Macrom. Sci. Phys.* **2007**, 46, 137-54.

35. Jung, Y. C.; Bhushan, B. Biomimetic structures for fluid drag reduction in laminar and turbulent flows. *J. Phys. Condens. Matter* **2009**, 22, 035104.

36. Kang, S. M.; Kim, S. M.; Kim, H. N.; Kwak, M. K.; Tahk, D. H.; Suh, K. Y. Robust superomniphobic surfaces with mushroom-like micropillar arrays. *Soft. Matter* **2012**, 8, 8563-8568.

37. Tuteja, A.; Choi, W.; Mabry, J. M.; McKinley, G. H.; Cohen, R. E. Engineering robust omniphobic surfaces with fluoro-POSS. Proceedings of AIChE Annual Meeting **2008**

38. Tuteja, A.; Choi, W.; Mabry, J. M.; McKinley, G. H.; Cohen, R. E. Robust omniphobic surfaces. Proceedings of the National Academy of Sciences **2008**, 105,18200.

39. Steele, A.; Bayer, I.; Loth, E. Inherently superoleophobic nanocomposite coatings by spray atomization. *Nano Lett*. **2008**, 9, 501-5.

40. Awal, A.; Ghosh, S. B.; Rana, M.; Hund, R. D.; Rossbach, V. Surface modification of cotton fabric by wet chemical treatments to impart hydrophobicity. *R. J. Tex. App*. **2010**, 14, 65-74.

41. Xu, B.; Cai, Z. Fabrication of a superhydrophobic ZnO nanorod array film on cotton fabrics via a wet chemical route and hydrophobic modification. *Appl. Surf. Sci*. **2008**, 254, 5899-904.

42. Tuteja, A.; Choi, W.; Mabry, J.; McKinley, G.; Cohen, R. Engineering superhydrophobic and superoleophobic surfaces. Abstract of Bio-Nanotechnology Conference and Trade Show, **2008**.

43. Quéré, D. Wetting and roughness. *Annu. Rev. Mater. Res.* **2008**, 38, 71-99.

44. Marmur, A. Wetting on hydrophobic rough surfaces: To be heterogeneous or not to be? *Langmuir* **2003**, 19, 8343-8.

45. Lee, H. J.; Owens, J. R. Motion of liquid droplets on a superhydrophobic oleophobic surface. *J. Mater. Sci.* **2011**, 46, 69-76.

46. Joly, L.; Biben, T. Wetting and friction on superoleophobic surfaces. *Soft. Matter.* **2009**, 5, 2549-57.

47. Saraf, R.; Lee, H. J.; Michielsen, S.; Owens, J.; Willis, C.; Stone, C. Wilusz E. Comparison of three methods for generating superhydrophobic, superoleophobic nylon nonwoven surfaces. *J. Mater. Sci.* **2011**, 46, 5751-5760.

48. Wenzel, R. N. Resistance of solid surfaces to wetting by water. *Indus. Eng. Chem.* **1936**, 28, 988-94.

49. Cassie, A. B. D.; Baxter, S. Wettability of porous surfaces. *Trans. Faraday Soc.* **1944**, 40, 546-551.

50. Lee, H. J.; Owens, J. R. Design of superhydrophobic ultraoleophobic NyCo. *J. Mater. Sci.* **2010**, 45, 3247-53.

51. Hasan, M.; Calvimontes, A.; Synytska, A.; Dutschk, V. Effects of topographic structure on wettability of differently woven fabrics. *Text. Res. J.* **2008**, 78, 996-1003.

52. Michielsen, S.; Lee, H. J. Design of a superhydrophobic surface using woven structures. *Langmuir* **2007**, 23, 6004-10.

53. Peirce, F. T. 5—the geometry of cloth structure. *J. Text. Inst. Trans.* **1937**, 28, 45-96.

54. Kemp, A. An extension of Peirce's cloth geometry to the treatment of non-circular threads. *J. Text. Inst. Trans.***1958**, 44-48.

55. Hearle, J. W. S.; Grosberg, P.; Backer, S. *Structural mechanics of fibers, yarns, and fabrics.* Wiley-interscience; New York, 1969.

56. Hearle, J.; Shanahan, W. 11-An energy method for calculations in fabric mechanics part I: principles of the method. *J. Text. Inst.* **1978**, 69, 81-91.

57. Kawabata, S.; Niwa, M. 38-A finite deformations theory of the 2/2 twill weave under biaxial extension. *J. Text. Inst.* **1979**, 70, 417-26.

58. Kawabata, S.; Niwa, M.; Kawai, H. 5-The finite deformation theory of plain weave fabrics. Part III: The shear deformation theory. *J. Text. Inst.***1973**, 64, 62-85.

59. Petterson, D.; Backer, S. Relationship between the structural geometry of a fabric and its physical properties. *Text. Res. J.* **1963**, 33, 809-16.

60. Taylor, H. 9-Tensile and tearing strength of cotton cloths. *J. Text. Inst. Trans.* **1959**, 50, 161-88.

61. Adanur S. *Handbook of weaving.* Technomic; 2000.

62. Alargirusamy, R. *Technical textile yarns* (series in textiles, N 101). 2010.

63. Behera, B.; Hari, P. *Woven textile structure. Creasing in Woven Fabrics,* Woodhead Publishing ; 2010.

64. Gandhi, K. *Woven textiles: Principles, developments and applications* (series in Textiles, N 125 series). Woodhead; 2012.

65. Grosicki, Z.; Watson, W. *Watson's textile design and color: Elementary weaves and figured fabrics.* Newnes-Butterworths; 1975. .

66. Lyle, D. S. *Performance of textiles.* Wiley New York; 1977.

67. El, M. Y. *Engineering textiles, integrating the design and manufacture of textile products.* Woodhead; 2009.

68. Chen, X. Modelling of textile structure for advanced applications. *J. Inform. Comput. Sci.* 2010, 5, 71-80.

69. Collier, A. M. *A handbook of textiles.* Pergamon Press; 1970.

70. Cook, J. G. *Handbook of textile fibers. volume I. manmade fibres. volume 2. natural fibres.* Merrow; 1984.

71. Smith, B. F.; Block, I. *Textiles in perspective.* Prentice-Hall; 1982.

72. Lord, P. R. *Handbook of yarn production: Technology, science and economics.* Woodhead; 2003.

73. Mukhopadhyay, A.; Kumar, M. V. A review on designing the waterproof breathable fabrics part II: Construction and suitability of breathable fabrics for different uses. J. Indus. Text. 2008, 38, 17-41.

74. Mukhopadhyay, A.; Midha, V. K. A review on designing the waterproof breathable fabrics part I: Fundamental principles and designing aspects of breathable fabrics. *J. Indus. Text.* **2008**, 37, 225-62.

75. Sherburn, M. *Geometric and mechanical modelling of textiles.* Faculty of Engineering: School of Mechanical, Materials and Manufacturing Engineering; 2007.

76. Wilson, J. *Handbook of textile design.* CRC; 2001.

77. Briggs, G. A.; Townsend, K. edited by *Textile design: Principles, advances and applications* (series in textiles). Woodhead; 2011.

78. Lamb, P. Siro and solo spinning. In *Advances in Yarn Spinning Technology*; Wang, X., Ed.; Woodhead; 2011.

79. Gomes, C. A. Fabrics in the military: Material demands. Industrial Fabric Products Review; 2006, 91, 48-53.

80. Lovasic, S. Chemical protective clothing. *Chem. Eng.* **2011**, 118, 51-3.
81. Shishoo, R. *Textiles in sport.* Woodhead; 2005.

82. Wilusz, E. *Military textiles*. Woodhead; 2008.

83. Morton, W. E.; Hearle, J. W. S. *Physical properties of textile fibres.* Textile Institute; 1993.

84. Smith, D. *Smart clothes and wearable technology.* Ai & Society; 2007.

85. Hsieh, Y, L.; Yu, B. Liquid wetting, transport, and retention properties of fibrous assemblies: Part I: Water wetting properties of woven fabrics and their constituent single fibers. *Text. Res. J.* **1992**, 62, 77-85.

86. Scardino, F. *An introduction to textile structures and their behaviour.* Elsevier Science Publishers; 1989.

87. Takajima, T. A*dvanced fiber spinning technology*. Woodhead; 1996.

88. Backer, S.; Tanenhaus, S. J. The relationship between the structural geometry of a textile fabric and its physical properties. *Text. Res. J.* **1951**, 21, 635-54.

89. Luzinov, I.; Brown, P; Chumanov, G.; Minko, S.; Klep, V.; Motornov, M.; Ramaratnam, K.; Iyer, S. K.; Zdyrko, B.; Liu, Y. Ultrahydrophobic fibers: Lotus approach. Annual Report - National Textile Center 2008, 11, 1-10.

90. Chen, X. *Modelling and predicting textile behaviour.* Woodhead; 2010. .

91. McCann, J.; Bryson, D. *Smart clothes and wearable technology.* Textile Institute; 2009.

92. Young, T. *An essay on the cohesion of fluids.* Phil. Trans. Roy. Soc. London 1805, 95, 65-87.

93. Barton, A. F. M. *CRC handbook of solubility parameters and other cohesion parameters.* CRC; 1991.

94. Kovats, E. Wetting of low energy model surfaces. *Pure App. Chem.* **1989**, 61, 1937-44.

95. Watson, M. D.; Price, J. B.; Cui, X.; Robert, K. Q.; Calamari, T. A. Measuring the short fiber content of cotton. *Text. Res. J.* **2003**, 73, 891-5.

96. Adams, D. P.; Schwarz, E. R.; Backer, S. The relationship between the structural geometry of a textile fabric and its physical properties. *Text. Res. J.***1956**, 26, 653-65.

97. Backer, S. The relationship between the structural geometry of a textile fabric and its physical properties. *Text. Res. J.* **1948**, 18, 650-8.

98. Jong, S. D.; Postle, R. 39-An energy analysis of woven fabric mechanics by means of optimal control theory part I: Tensile properties. *J.Text. Inst.* **1977**, 68, 350-61.

99. Love, L. Graphical relationships in cloth geometry for plain, twill, and sateen weaves. *Text. Res. J.* **1954**, 24, 1073-83.

100. Scelzo, W.; Backer, S.; Boyce, M. Mechanistic role of yarn and fabric structure in determining tear resistance of woven cloth part I: Understanding tongue tear. *Text. Res. J.* **1994**, 64, 291-304.

101. Triki, E.; Vu, K. T.; Nguyen, T. P.; Boukehili, H. Mechanics and mechanisms of tear resistance of woven fabrics. *Theor. Appl. Fract. Mech.* **2012**, 61, 33-39.

102. Shanahan, W.; Hearle, J. 12-An energy method for calculations in fabric mechanics part II: Examples of application of the method to woven fabrics. *Text. Res. J.* **1978**, 69, 92-100.

103. Scelzo, W.; Backer, S.; Boyce, M. Mechanistic role of yarn and fabric structure in determining tear resistance of woven cloth. *Text. Res. J.* **1994**, 64, 291-304.

104. Bhushan, B.; Jung, Y. C. Micro-and nanoscale characterization of hydrophobic and hydrophilic leaf surfaces. *Nanotechnology* 2006, 17, 2758.

105. Lin, L.; Wang, C.; Chen, C.; Chen, K. Water-repellency and antibacterial activities of plasma-treated cleavable silicone surfactants on nylon fabrics. *Surf. Coat. Technol.* **2006**, 201, 674-8.

106. Mao, Z.; Shi, Q.; Zhang, L.; Cao, H. The formation and UV-blocking property of needle-shaped ZnO nanorod on cotton fabric. *Thin. Solid Films* **2009**, 517, 2681-6.

107. Pacholski, C.; Kornowski. A.; Weller, H. Self-Assembly of ZnO: From nanodots to nanorods. *Angewandte Chemie Inter. Ed.* 2002, 41,1188-91.

108. Nosonovsky, M.; Bhushan, B. Multiscale friction mechanisms and hierarchical surfaces in nano-and bio-tribology. *Mat. Sci. Eng.: R: Rep.* **2007,** 58, 162-93.

109. Adamson, A. W.; Gast A. P. *Physical chemistry of surfaces.* Wiley NY; 1990.

110. Extrand, C. Model for contact angles and hysteresis on rough and ultraphobic surfaces. *Langmuir* 2002,18, 7991-9.

111. Kijlstra, J.; Reihs, K.; Klamt, A. Roughness and topology of ultra-hydrophobic surfaces. *Colloids Surf. Physicochem Eng.* **2002**, 206, 521-9.

112. Lee, H. J.; Michielsen, S. Lotus effect: Superhydrophobicity. *J. Text. Inst.* **2006**, 97, 455-62.

113. Kamusewitz, H.; Possart, W.; Paul, D. The relation between Young's equilibrium contact angle and the hysteresis on rough paraffin wax surfaces. *Colloids Surf. Physicochem Eng.* **1999**, 156, 271-9.

114. Israelachvili, J. N. *Intermolecular and surface forces: Revised third edition*. Academic press; 2011.

115. Bhushan, B. *Principles and applications of tribology*. Wiley-Interscience; 1999.

116. Fowkes, F. M. Additivity of intermolecular forces at interfaces. I. Determination of the contribution to surface and interfacial tensions of dispersion forces in various liquids1. *J. Phys. Chem.* **1963**, 67, 2538-41.

117. Ralchenko, L.; Ostrovskaya, A.; Podestà, P.; Milani, V. Influence of surface morphology on the wettability of cluster-assembled carbon films. *EPL (Europhysics Letters)* **2003**, 63, 401.

118. Nosonovsky, M.; Bhushan, B. Biomimetic superhydrophobic surfaces: Multiscale approach. *Nano Letters* **2007**, 7, 2633-7.

119. Patankar, N. A. Transition between superhydrophobic states on rough surfaces. *Langmuir* **2004**, 20, 7097-102.

120. Bartolo, D.; Bouamrirene, F.; Verneuil, E.; Buguin, A.; Silberzan, P.; Moulinet, S. Bouncing or sticky droplets: Impalement transitions on superhydrophobic micropatterned surfaces. *EPL (Europhysics Letters)* **2007**, 74, 299.

121. Lafuma, A; Quere, D. Superhydrophobic states. *Nature Mat.* **2003**, 2, 457-60.

122. Nosonovsky, M.; Bhushan, B. Energy transitions in superhydrophobicity: Low adhesion, easy flow and bouncing. *J. Phys. Condensed Matt.* **2008**, 20, 395005.

123. Reyssat, M.; Pépin, A.; Marty, F.; Chen, Y.; Quéré, D. Bouncing transitions on microtextured materials. *EPL (Europhysics Letters)* **2007**, 74, 306.

124. Richard, D.; Clanet, C.; Quéré, D. Contact time of a bouncing drop. *Nature* **2002**, 417, 811.

125. de Gennes, P. G.; Brochard, W. F.; Quere, D. *Capillarity and wetting phenomena.* Springer; 2008.

126. Nosonovsky, M.; Bhushan, B. Roughness optimization for biomimetic superhydrophobic surfaces. *Microsyst. Technol*. **2005**, 11, 535-49.

127. Johnson, R.; Dettre, R. H. Contact angle hysteresis. Contact Angle, Wettability, and Adhesion. *Ad. Chem.* **1964**, 43, 112-35.

128. Li, W.; Amirfazli, A. A thermodynamic approach for determining the contact angle hysteresis for superhydrophobic surfaces. *J. Colloid Interface Sci.* **2005**, 292, 195-201.

129. Carey, V. P. *Liquid-vapor phase-change phenomena.* Taylor and Francis; 2008.

130. Batchelor, G. K. *An introduction to fluid dynamics.* Cambridge univ. press; 2000.

131. Jung, Y. C.; Bhushan, B. Wetting transition of water droplets on superhydrophobic patterned surfaces. *Scr. Mater.* **2007**, 57, 1057-60.

132. Jung, Y. C.; Bhushan, B. Wetting behaviour during evaporation and condensation of water microdroplets on superhydrophobic patterned surfaces. *J. Microsc.* **2007**, 229, 127-40.

133. Jung, Y. C.; Bhushan, B. Dynamic effects of bouncing water droplets on superhydrophobic surfaces. *Langmuir* **2008**, 24, 6262-9.

134. Jung, Y. C.; Bhushan, B. Dynamic effects induced transition of droplets on biomimetic superhydrophobic surfaces. *Langmuir* **2009**, 25, 9208-18.

135. Reyssat, M.; Yeomans, J.; Quéré, D. Impalement of fakir drops. *EPL (Europhysics Letters)* **2007**, 81, 26006.

136. Bhushan, B.; Chae, J. Y. Wetting study of patterned surfaces for superhydrophobicity. *Ultramicroscopy* **2007**, 107, 1033-41.

137. Bhushan, B.; Jung, Y. C. Wetting, adhesion and friction of superhydrophobic and hydrophilic leaves and fabricated micro/nanopatterned surfaces. *J. Phys. Condensed Matt.* **2008**, 20, 225010.

138. Israelachvili, J. N.; Gee, M. L. Contact angles on chemically heterogeneous surfaces. *Langmuir* **1989**, 5, 288-9.

139. Hosono, E.; Fujihara, S.; Honma, I.; Zhou, H. Superhydrophobic perpendicular nanopin film by the bottom-up process. *J. Am. Chem. Soc.* **2005**, 127, 13458-9.

140. Derjaguin, B.; Churaev, N. Structural component of disjoining pressure. J. *Colloid Interface Sci.* **1974**, 49, 249-55.

141. Huang, L.; Lau, S.; Yang, H.; Leong, E.; Yu, S.; Prawer, S. Stable superhydrophobic surface via carbon nanotubes coated with a ZnO thin film. *J. Phys. Chem. B* **2005**, 109, 7746-8.

142. Choi, W.; Tuteja, A.; Mabry, J. M.; Cohen, R. E.; McKinley, G.H. A modified Cassie-Baxter relationship to explain contact angle hysteresis and anisotropy on non-wetting textured surfaces. *J. Colloid Interface Sci.* **2009**, 339, 208-16.

143. Pollitt J. The geometry of cloth structure. Proceedings of Journal of the Textile Institute 1949, 40, 11-22.

144. Houshyar, S.; Shanks, R. A.; Hodzic, A. Influence of different woven geometry in poly (propylene) woven composites. *Macromoles. Mat. Eng.* **2005**, 290, 45-52.

145. Hamilton, J. 7-A general system of woven fabric geometry. *J. Text. Inst. Trans.* **1964**, 55, 66-82.

146. Kawabata, S.; Niwa, M.; Kawai, H. 3-THe finite deformation theory of plain weave fabrics part I: The biaxial deformation theory. *J. Text. Inst.* **1973**, 64, 21-46.

147. Kawabata, S.; Niwa, M.; Kawai, H. 4-The finite deformation theory of plain weave fabrics. Part II: The uniaxial deformation theory. *J. Text. Inst.* **1973**, 64, 47-61.

148. Behera, B.; Militky, J.; Mishra, R.; Kremenakova, D. *Modeling of woven fabrics geometry and properties.* Woven fabrics. Jeon, H. Y., Ed.; InTech; 2012.

149. Lou, L.; Development of biomimetic duck feather fibers. M.S. Thesis, North Carolina State University, NC, 2013.

150. Shoukry, H.; Kotkata, M. F.; Abo-el-Enein, S. A.; Morsy, M. S. Flexural strength and physical properties of fiber reinforced nano metakaolin cementitious surface compound. Constr. Build. Mater. **2013**, 43, 453-460.

APPENDIX

A. 4.1 Change of contact angle at varied *T* in different woven structures when *e*=1.

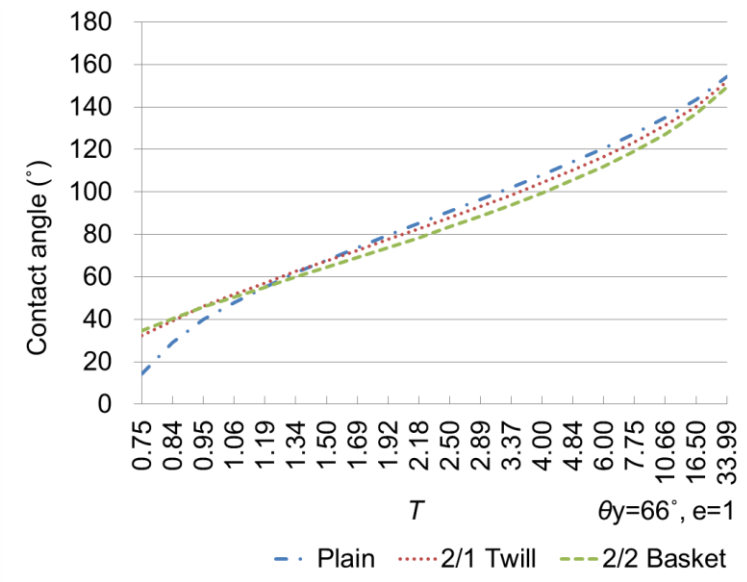
Contact angle (°)
180
160
140
120
100
80
60
40
20
0
0.75
0.84
0.95
1.06
1.19
1.34
1.50
1.69
1.92
2.18
2.50
2.89
3.37
4.00
4.84
6.00
7.75
10.66
16.50
33.99
T
θy=66˚, e=1
Plain
2/1 Twill
2/2 Basket

(a)

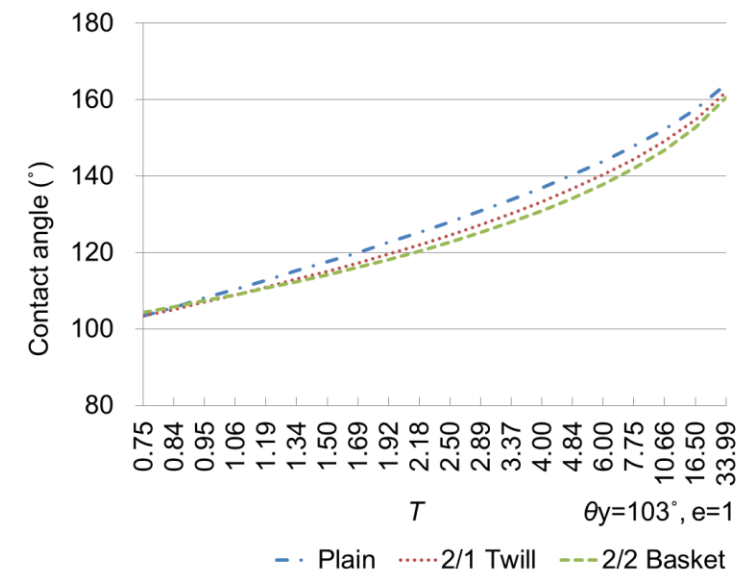
Contact angle (°)
180
160
140
120
100
80
0.75
0.84
0.95
1.06
1.19
1.34
1.50
1.69
1.92
2.18
2.50
2.89
3.37
4.00
4.84
6.00
7.75
10.66
16.50
33.99
T
θy=103˚, e=1
Plain
2/1 Twill
2/2 Basket

(b)

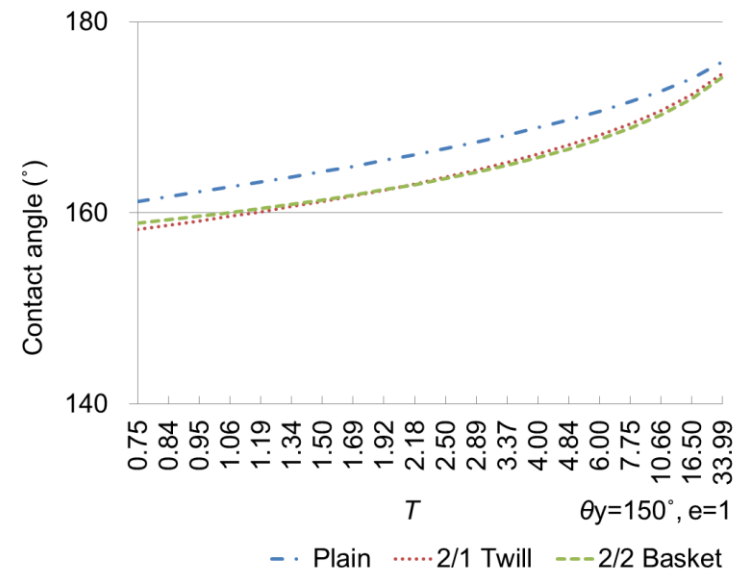
180
160
140
Contact angle (°)
0.75
0.84
0.95
1.06
1.19
1.34
1.50
1.69
1.92
2.18
2.50
2.89
3.37
4.00
4.84
6.00
7.75
10.66
16.50
33.99
T
θy=150˚, e=1
Plain
2/1 Twill
2/2 Basket

(c)

A. 4.2 Change of contact angle at varied *T* in different woven structures when *e*=0.9.

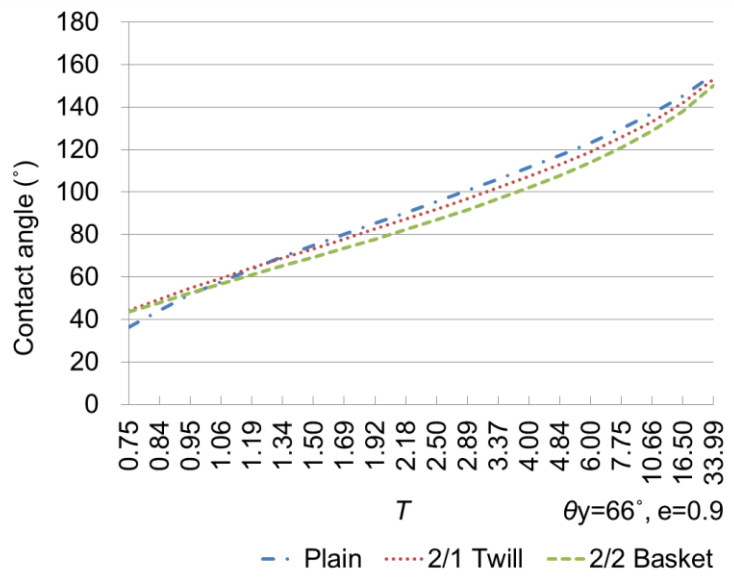
180
160
140
120
100
80
60
40
20
0
Contact angle (°)
0.75
0.84
0.95
1.06
1.19
1.34
1.50
1.69
1.92
2.18
2.50
2.89
3.37
4.00
4.84
6.00
7.75
10.66
16.50
33.99
T
θy=66˚, e=0.9
Plain
2/1 Twill
2/2 Basket

(a)

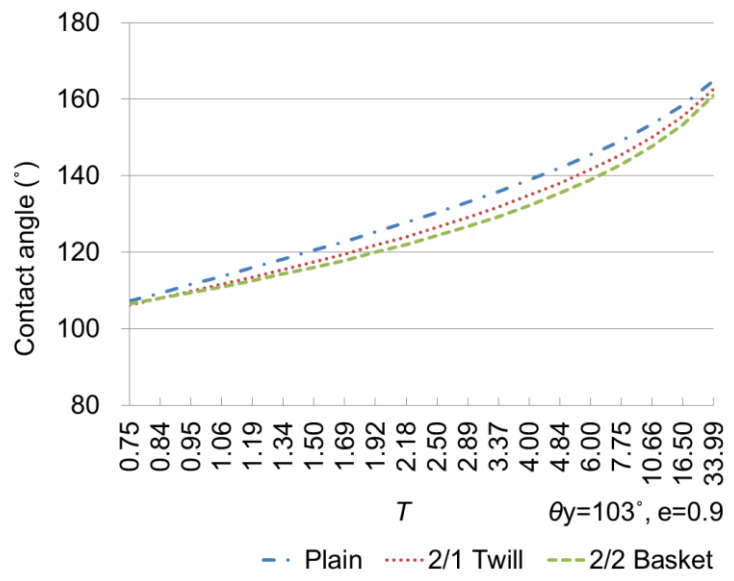
180
160
140
120
100
80
Contact angle (°)
0.75
0.84
0.95
1.06
1.19
1.34
1.50
1.69
1.92
2.18
2.50
2.89
3.37
4.00
4.84
6.00
7.75
10.66
16.50
33.99
T
θy=103˚, e=0.9
Plain
2/1 Twill
2/2 Basket

(b)

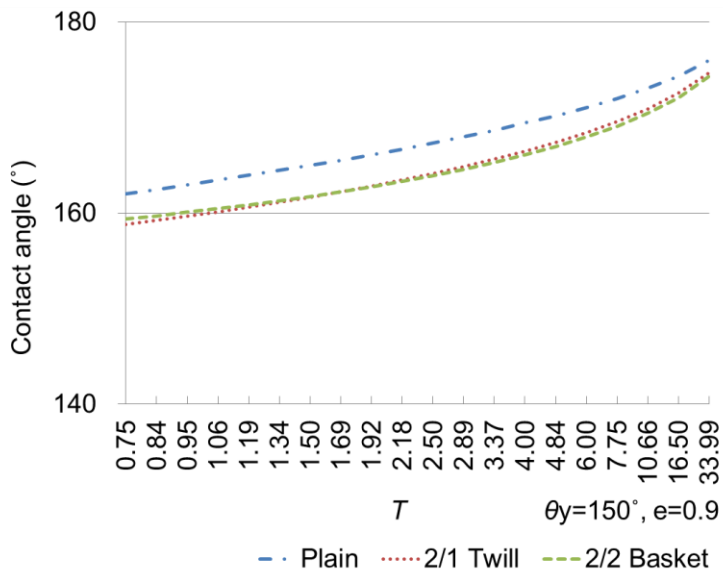
180
160
140
Contact angle (˚)
0.75
0.84
0.95
1.06
1.19
1.34
1.50
1.69
1.92
2.18
2.50
2.89
3.37
4.00
4.84
6.00
7.75
10.66
16.50
33.99
T
θy=150˚, e=0.9
Plain
2/1 Twill
2/2 Basket

(c)

A. 4.3 Change of contact angle at varied *T* in different woven structures when *e*=0.8.

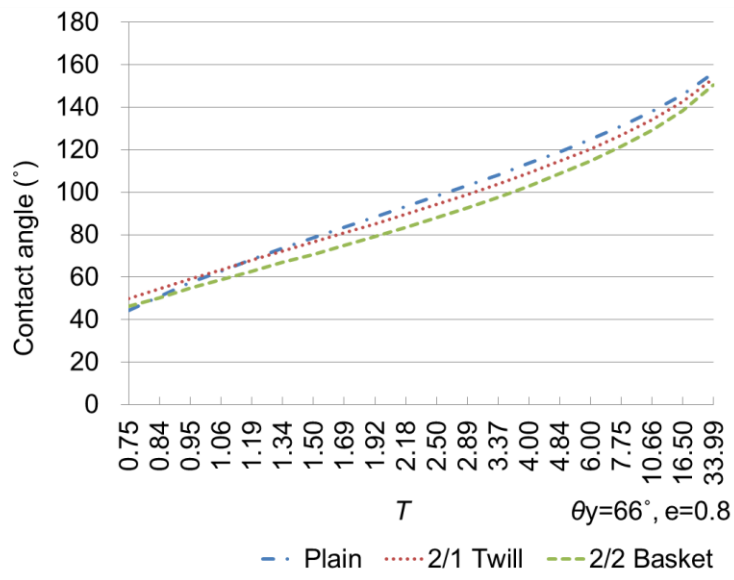
180
160
140
120
100
80
60
40
20
0
Contact angle (°)
0.75
0.84
0.95
1.06
1.19
1.34
1.50
1.69
1.92
2.18
2.50
2.89
3.37
4.00
4.84
6.00
7.75
10.66
16.50
33.99
T
θy=66°, e=0.8
Plain
2/1 Twill
2/2 Basket

(a)

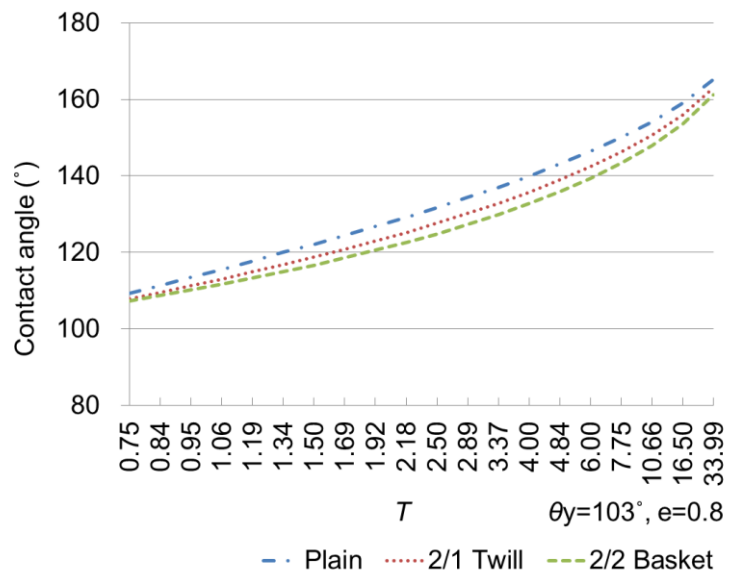
180
160
140
120
100
80
Contact angle (°)
0.75
0.84
0.95
1.06
1.19
1.34
1.50
1.69
1.92
2.18
2.50
2.89
3.37
4.00
4.84
6.00
7.75
10.66
16.50
33.99
T
θy=103°, e=0.8
Plain
2/1 Twill
2/2 Basket

(b)

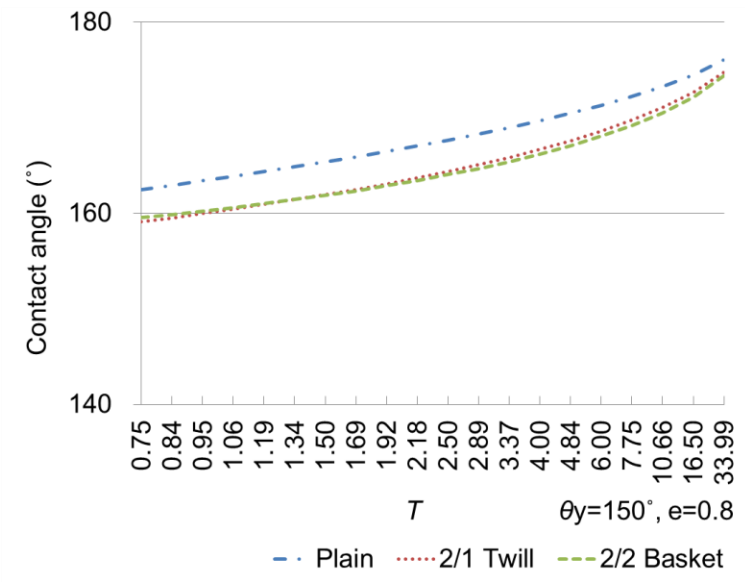
180
160
140
Contact angle (˚)
0.75
0.84
0.95
1.06
1.19
1.34
1.50
1.69
1.92
2.18
2.50
2.89
3.37
4.00
4.84
6.00
7.75
10.66
16.50
33.99
T
θy=150˚, e=0.8
Plain
2/1 Twill
2/2 Basket

(c)

A. 4.4 Change of contact angle at varied *T* in different woven structures when *e*=0.7.

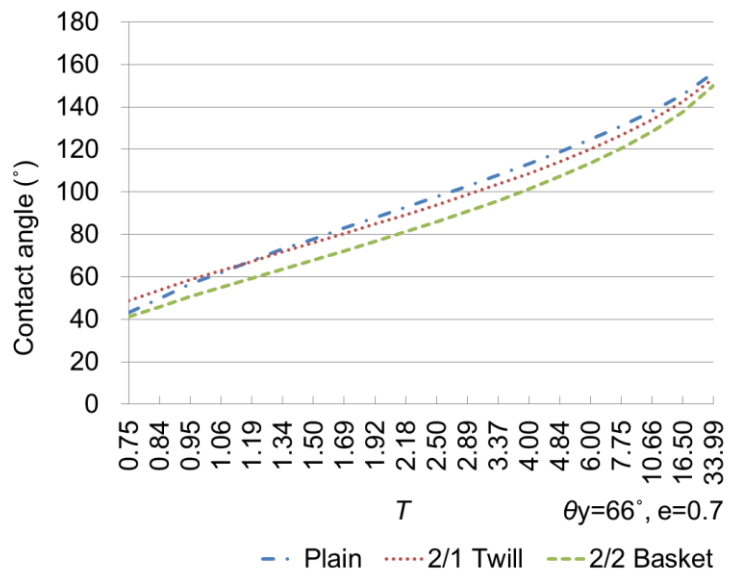
Contact angle (°)
180
160
140
120
100
80
60
40
20
0
0.75
0.84
0.95
1.06
1.19
1.34
1.50
1.69
1.92
2.18
2.50
2.89
3.37
4.00
4.84
6.00
7.75
10.66
16.50
33.99
T
θy=66˚, e=0.7
Plain
2/1 Twill
2/2 Basket

(a)

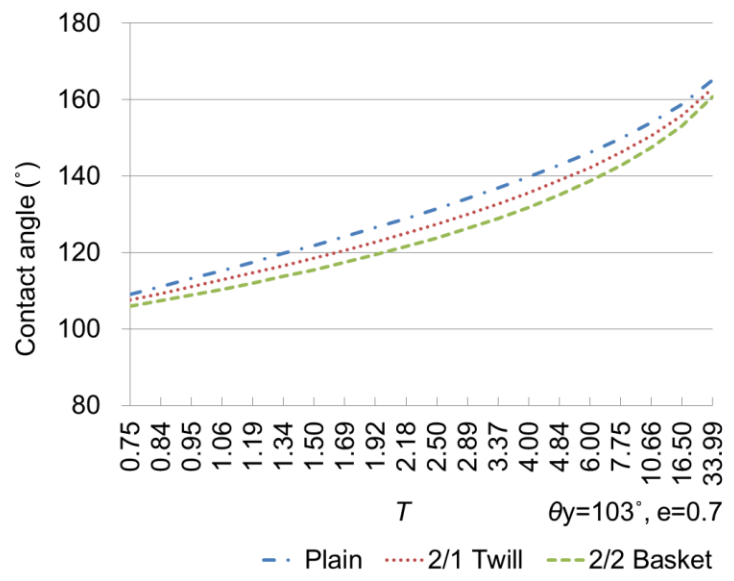
Contact angle (°)
180
160
140
120
100
80
0.75
0.84
0.95
1.06
1.19
1.34
1.50
1.69
1.92
2.18
2.50
2.89
3.37
4.00
4.84
6.00
7.75
10.66
16.50
33.99
T
θy=103˚, e=0.7
Plain
2/1 Twill
2/2 Basket

(b)

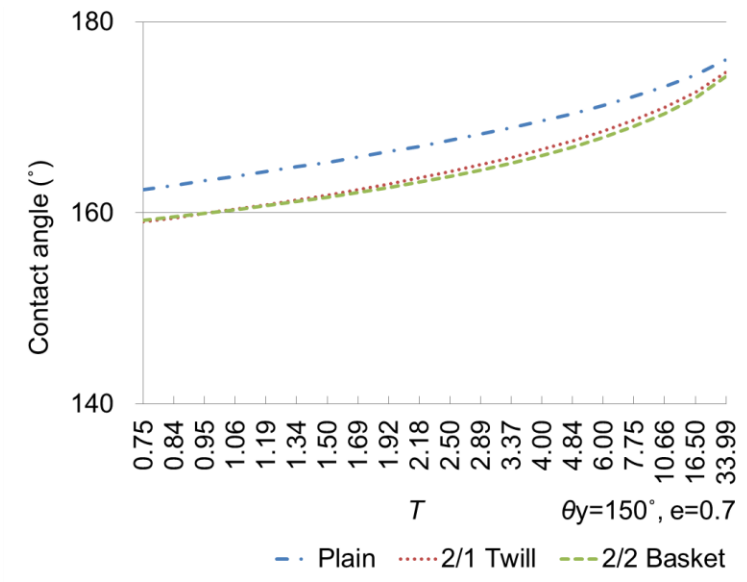
180
160
140
Contact angle (˚)
0.75
0.84
0.95
1.06
1.19
1.34
1.50
1.69
1.92
2.18
2.50
2.89
3.37
4.00
4.84
6.00
7.75
10.66
16.50
33.99
T
θy=150˚, e=0.7
Plain
2/1 Twill
2/2 Basket

(c)

A. 4.5 Change of contact angle at varied *T* in different woven structures when *e*=0.6.

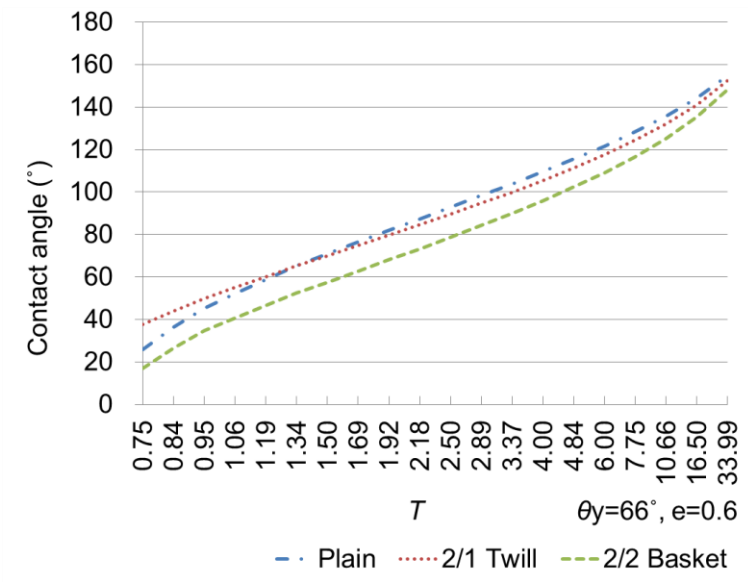
Contact angle (°)
180
160
140
120
100
80
60
40
20
0
0.75
0.84
0.95
1.06
1.19
1.34
1.50
1.69
1.92
2.18
2.50
2.89
3.37
4.00
4.84
6.00
7.75
10.66
16.50
33.99
T
θy=66˚, e=0.6
Plain
2/1 Twill
2/2 Basket

(a)

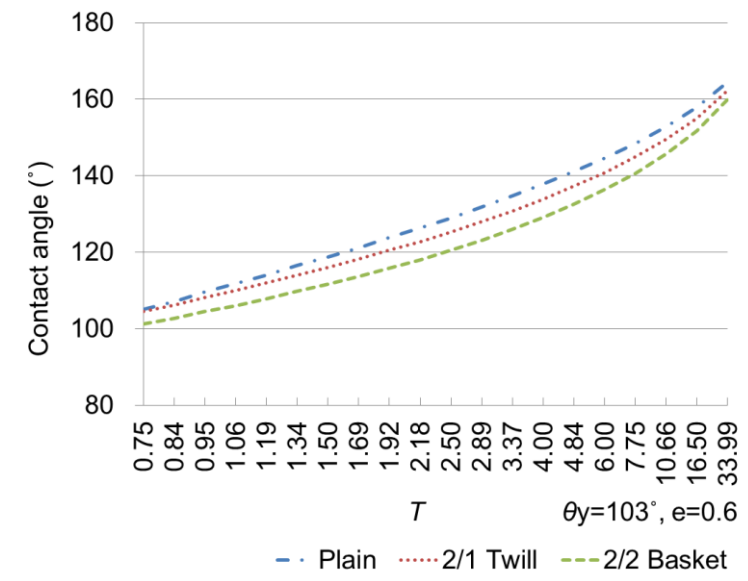
Contact angle (°)
180
160
140
120
100
80
0.75
0.84
0.95
1.06
1.19
1.34
1.50
1.69
1.92
2.18
2.50
2.89
3.37
4.00
4.84
6.00
7.75
10.66
16.50
33.99
T
θy=103˚, e=0.6
Plain
2/1 Twill
2/2 Basket

(b)

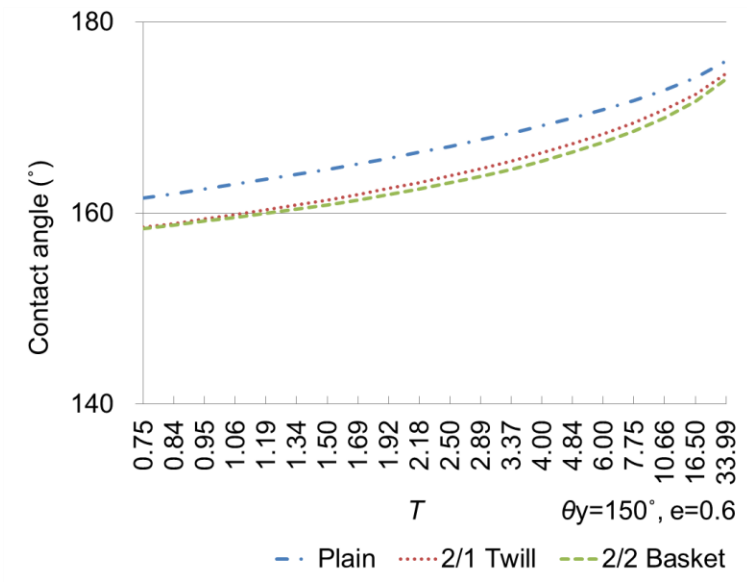
180
160
140
Contact angle (˚)
0.75
0.84
0.95
1.06
1.19
1.34
1.50
1.69
1.92
2.18
2.50
2.89
3.37
4.00
4.84
6.00
7.75
10.66
16.50
33.99
T
θy=150˚, e=0.6
Plain
2/1 Twill
2/2 Basket

(c)

A. 4.6 Change of contact angle at varied *T* in different woven structures when *e*=0.5.

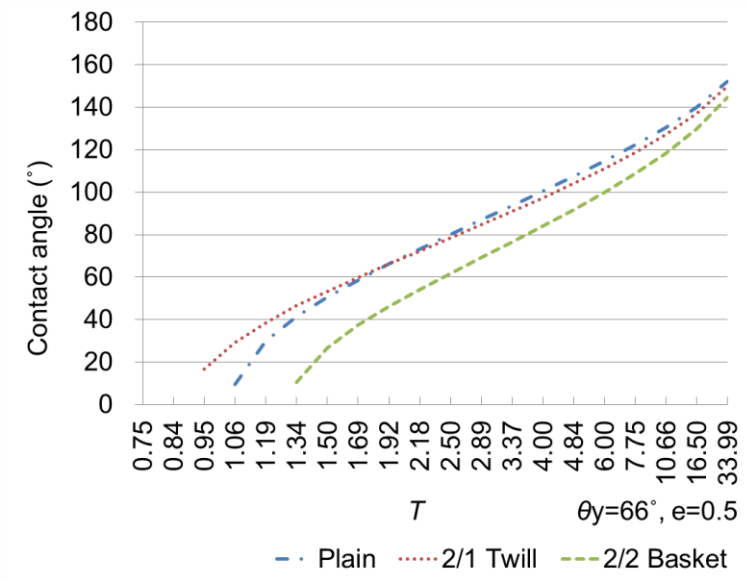
Contact angle (°)
180
160
140
120
100
80
60
40
20
0
0.75
0.84
0.95
1.06
1.19
1.34
1.50
1.69
1.92
2.18
2.50
2.89
3.37
4.00
4.84
6.00
7.75
10.66
16.50
33.99
T
θy=66˚, e=0.5
Plain
2/1 Twill
2/2 Basket

(a)

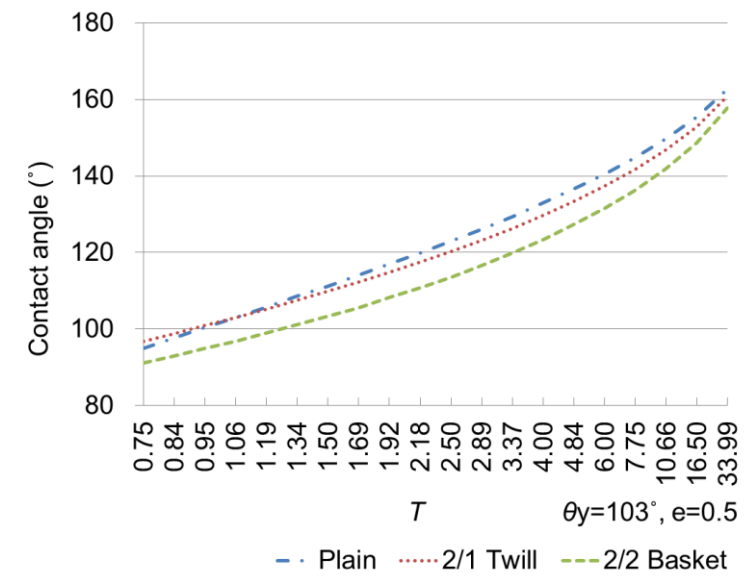
Contact angle (°)
180
160
140
120
100
80
0.75
0.84
0.95
1.06
1.19
1.34
1.50
1.69
1.92
2.18
2.50
2.89
3.37
4.00
4.84
6.00
7.75
10.66
16.50
33.99
T
θy=103˚, e=0.5
Plain
2/1 Twill
2/2 Basket

(b)

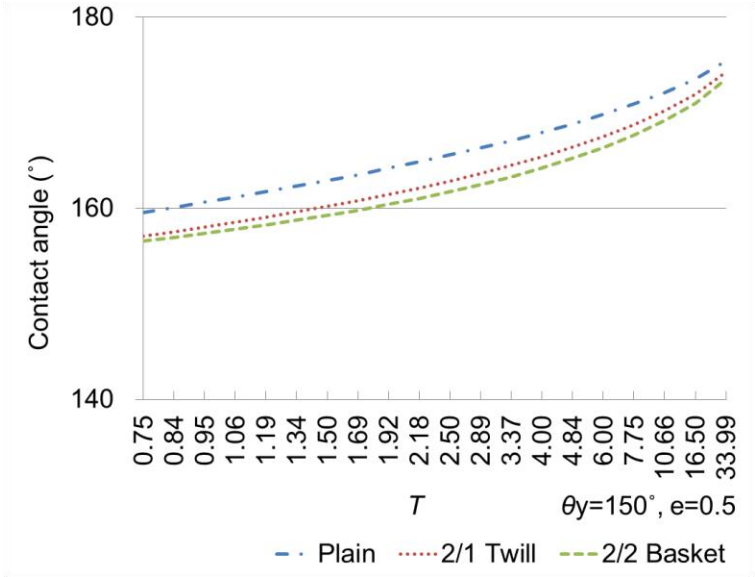
180
160
140
Contact angle (˚)
0.75
0.84
0.95
1.06
1.19
1.34
1.50
1.69
1.92
2.18
2.50
2.89
3.37
4.00
4.84
6.00
7.75
10.66
16.50
33.99
T
θy=150˚, e=0.5
Plain
2/1 Twill
2/2 Basket

(c)

A. 4.7 Change of contact angle at varied *T* in different woven structures when *e*=0.4.

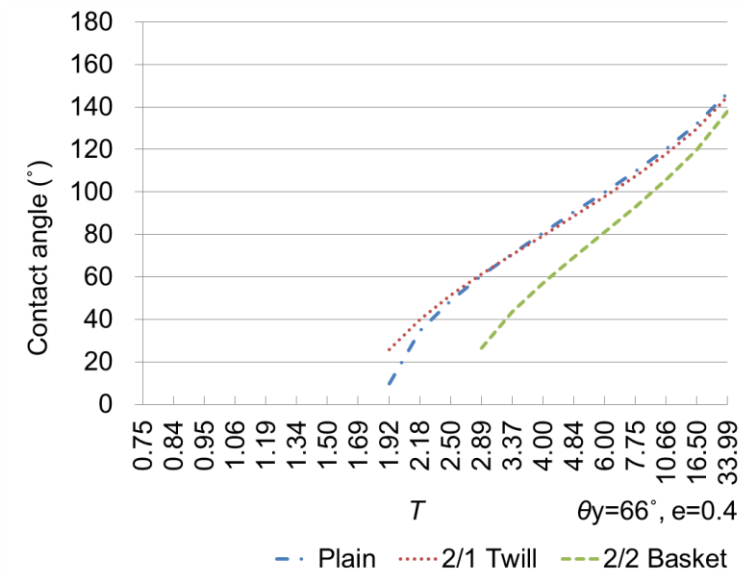
Contact angle (°)
180
160
140
120
100
80
60
40
20
0
0.75
0.84
0.95
1.06
1.19
1.34
1.50
1.69
1.92
2.18
2.50
2.89
3.37
4.00
4.84
6.00
7.75
10.66
16.50
33.99
T
θy=66˚, e=0.4
Plain
2/1 Twill
2/2 Basket

(a)

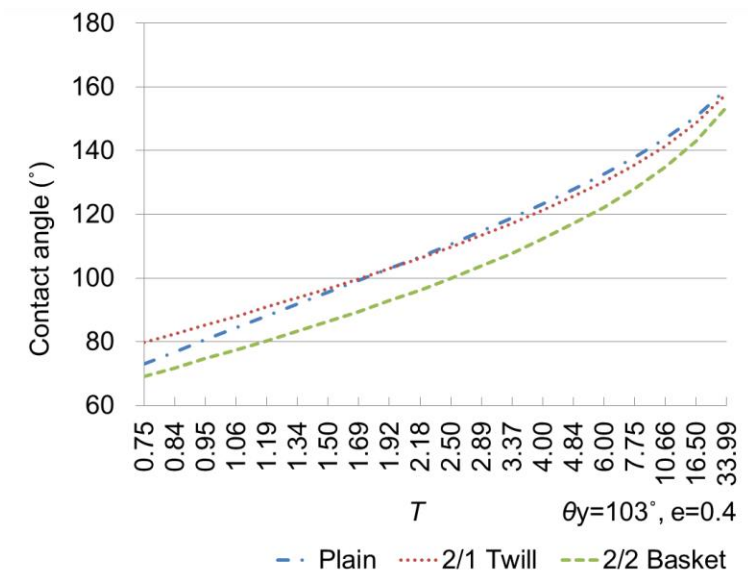
Contact angle (°)
180
160
140
120
100
80
60
0.75
0.84
0.95
1.06
1.19
1.34
1.50
1.69
1.92
2.18
2.50
2.89
3.37
4.00
4.84
6.00
7.75
10.66
16.50
33.99
T
θy=103˚, e=0.4
Plain
2/1 Twill
2/2 Basket

(b)

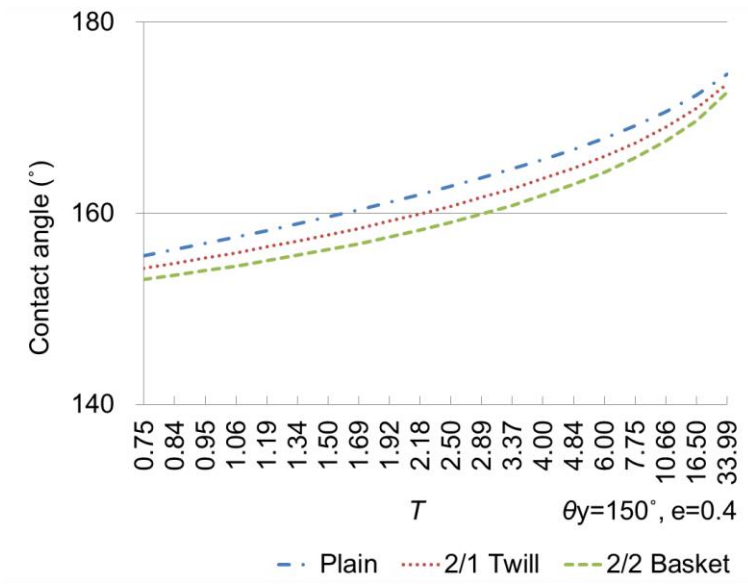
180
160
140
Contact angle (˚)
0.75
0.84
0.95
1.06
1.19
1.34
1.50
1.69
1.92
2.18
2.50
2.89
3.37
4.00
4.84
6.00
7.75
10.66
16.50
33.99
T
θy=150˚, e=0.4
Plain
2/1 Twill
2/2 Basket

(c)

A. 4.8 Change of contact angle at varied *T* in different woven structures when *e*=0.3.

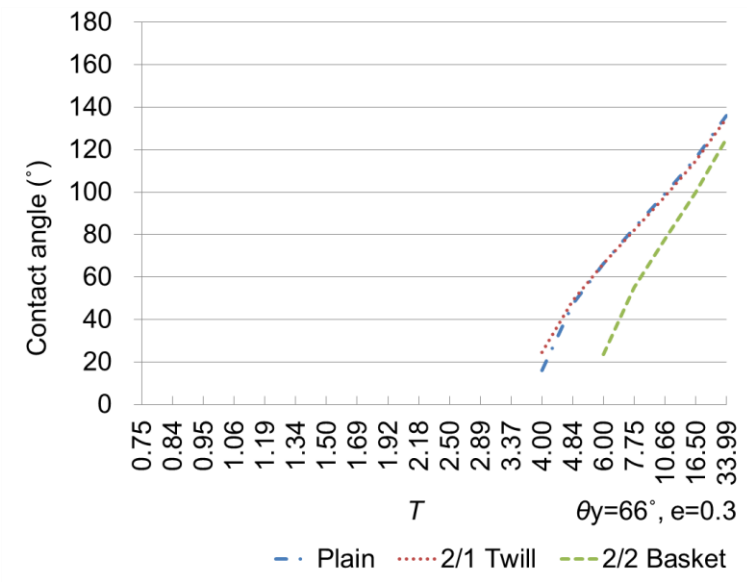
Contact angle (°)
180
160
140
120
100
80
60
40
20
0
0.75
0.84
0.95
1.06
1.19
1.34
1.50
1.69
1.92
2.18
2.50
2.89
3.37
4.00
4.84
6.00
7.75
10.66
16.50
33.99
T
θy=66˚, e=0.3
Plain
2/1 Twill
2/2 Basket

(a)

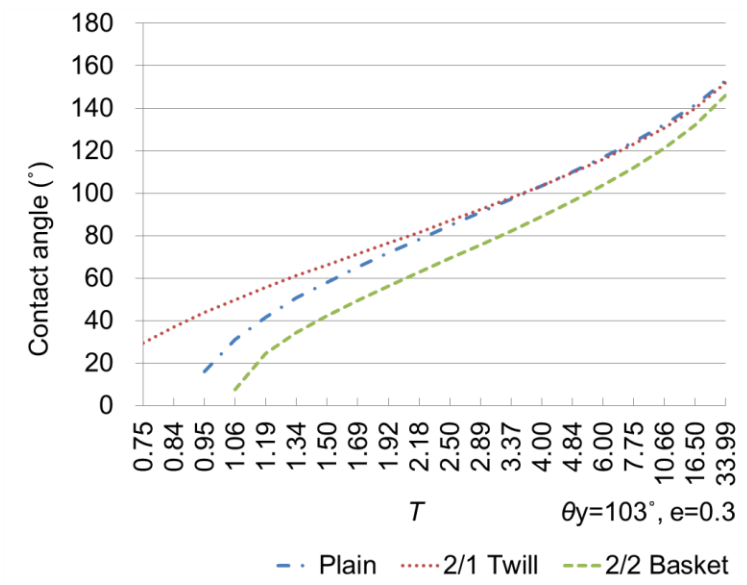
Contact angle (°)
180
160
140
120
100
80
60
40
20
0
0.75
0.84
0.95
1.06
1.19
1.34
1.50
1.69
1.92
2.18
2.50
2.89
3.37
4.00
4.84
6.00
7.75
10.66
16.50
33.99
T
θy=103˚, e=0.3
Plain
2/1 Twill
2/2 Basket

(b)

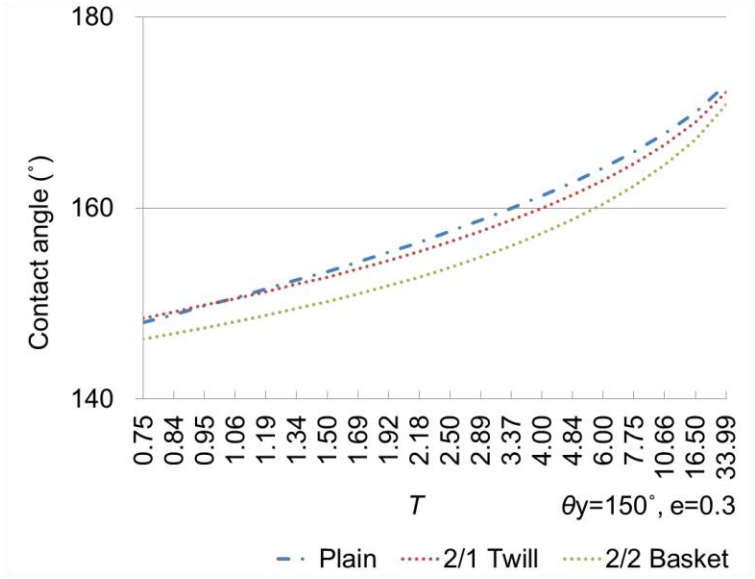
180
160
140
Contact angle (˚)
0.75
0.84
0.95
1.06
1.19
1.34
1.50
1.69
1.92
2.18
2.50
2.89
3.37
4.00
4.84
6.00
7.75
10.66
16.50
33.99
T
θy=150˚, e=0.3
Plain
2/1 Twill
2/2 Basket

(c)

A. 4.9 Change of contact angle at varied *T* in different woven structures when *e*=0.2.

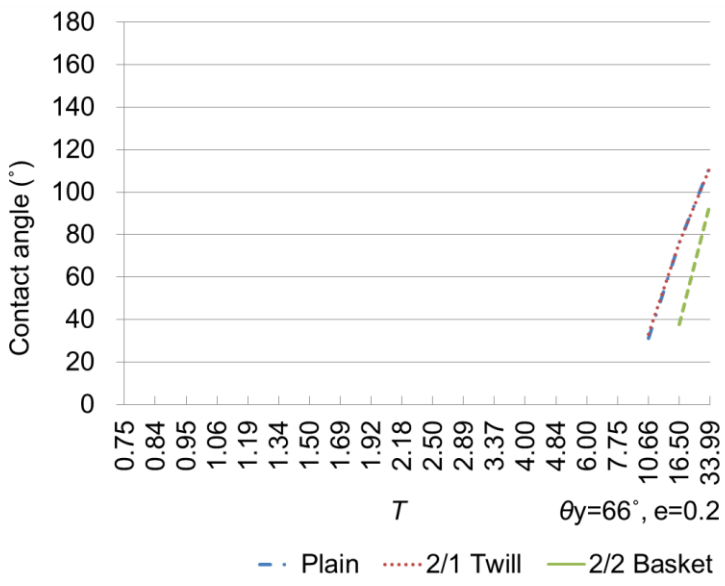
180
160
140
120
100
80
60
40
20
0
Contact angle (°)
0.75
0.84
0.95
1.06
1.19
1.34
1.50
1.69
1.92
2.18
2.50
2.89
3.37
4.00
4.84
6.00
7.75
10.66
16.50
33.99
T
θy=66°, e=0.2
Plain
2/1 Twill
2/2 Basket

(a)

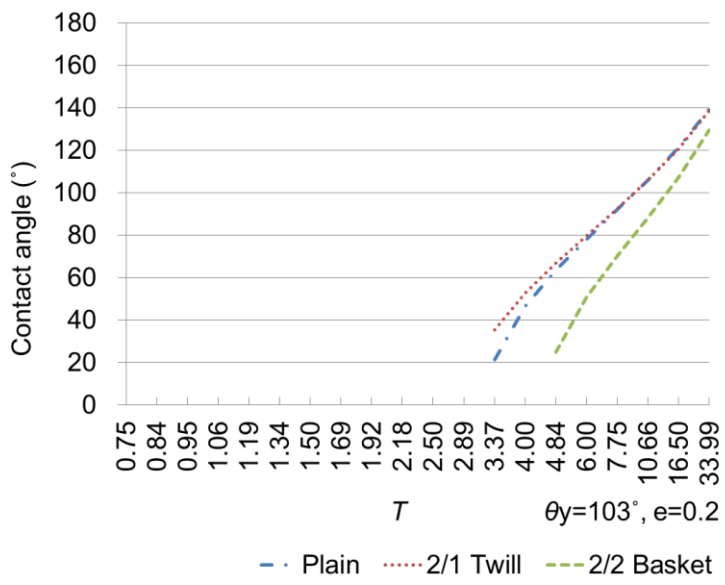
180
160
140
120
100
80
60
40
20
0
Contact angle (°)
0.75
0.84
0.95
1.06
1.19
1.34
1.50
1.69
1.92
2.18
2.50
2.89
3.37
4.00
4.84
6.00
7.75
10.66
16.50
33.99
T
θy=103°, e=0.2
Plain
2/1 Twill
2/2 Basket

(b)

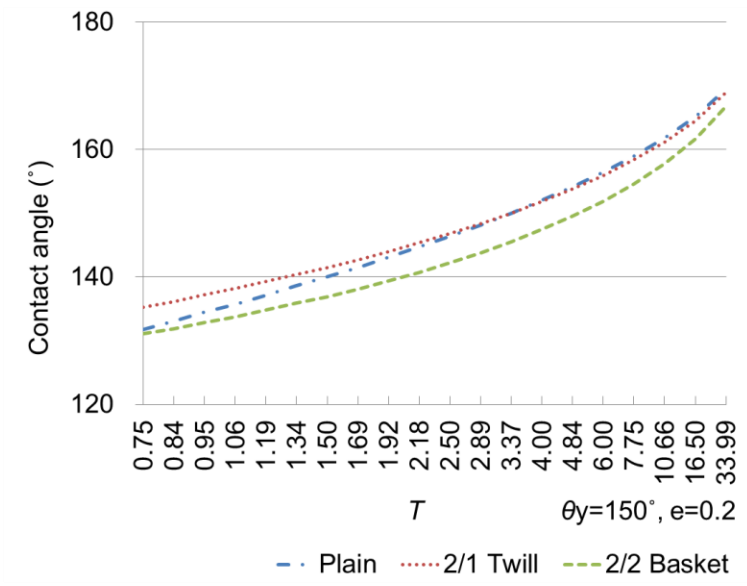
180
160
140
120
Contact angle (˚)
0.75
0.84
0.95
1.06
1.19
1.34
1.50
1.69
1.92
2.18
2.50
2.89
3.37
4.00
4.84
6.00
7.75
10.66
16.50
33.99
T
θy=150˚, e=0.2
Plain
2/1 Twill
2/2 Basket

(c)

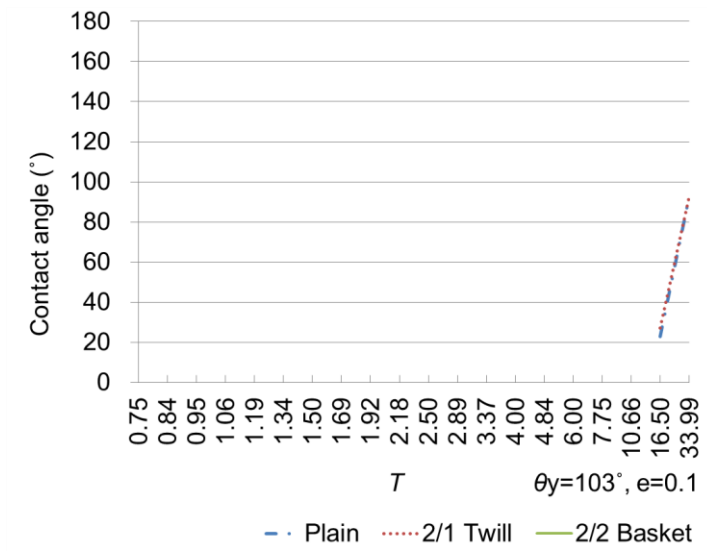

(a)

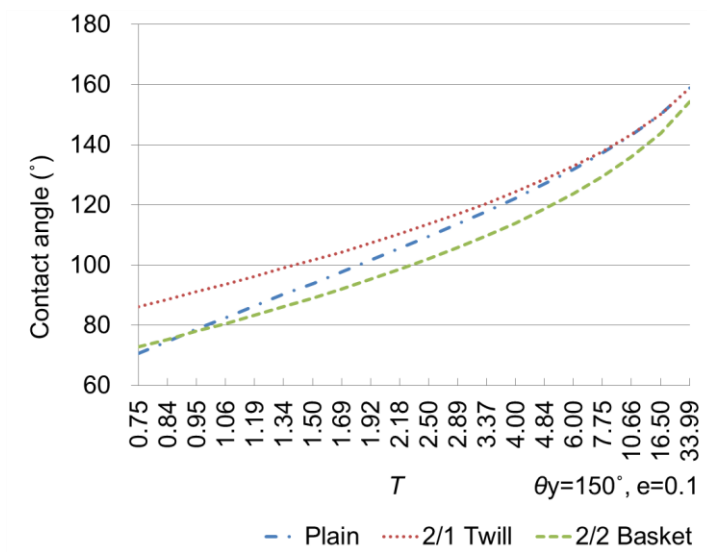

(b)

A. 4.10 Change of contact angle at varied T in different woven structures when e=0.1 (Any contact angle has not been shown when θ_y=66, e=0.1).

A. 4.11 Difference of contact angle at varied T in plain structure when $e \leq 1$.

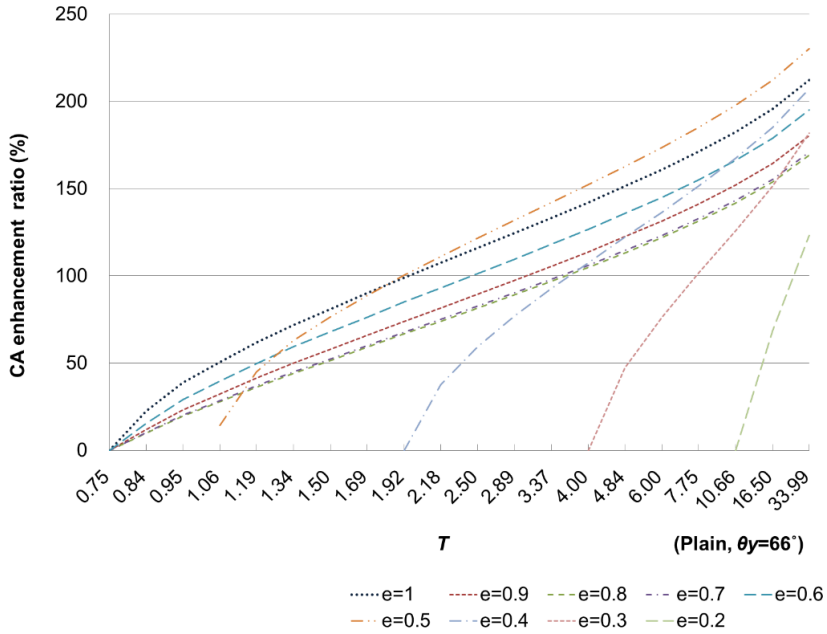
250
200
150
100
50
0
CA enhancement ratio (%)
0.75
0.84
0.95
1.06
1.19
1.34
1.50
1.69
1.92
2.18
2.50
2.89
3.37
4.00
4.84
6.00
7.75
10.66
16.50
33.99
T
(Plain, θy=66˚)
e=1
e=0.9
e=0.8
e=0.7
e=0.6
e=0.5
e=0.4
e=0.3
e=0.2

(a)

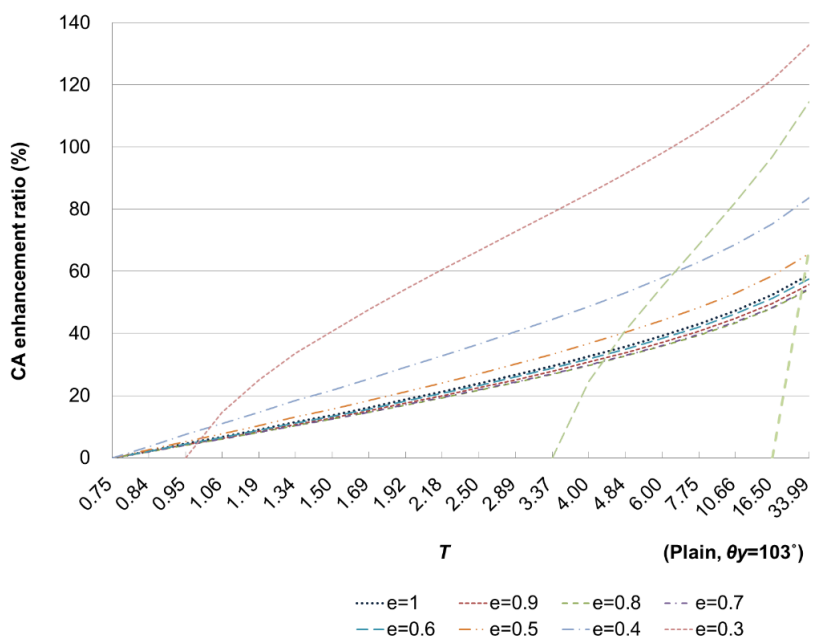
140
120
100
80
60
40
20
0
CA enhancement ratio (%)
0.75
0.84
0.95
1.06
1.19
1.34
1.50
1.69
1.92
2.18
2.50
2.89
3.37
4.00
4.84
6.00
7.75
10.66
16.50
33.99
T
(Plain, θy=103˚)
e=1
e=0.9
e=0.8
e=0.7
e=0.6
e=0.5
e=0.4
e=0.3

(b)

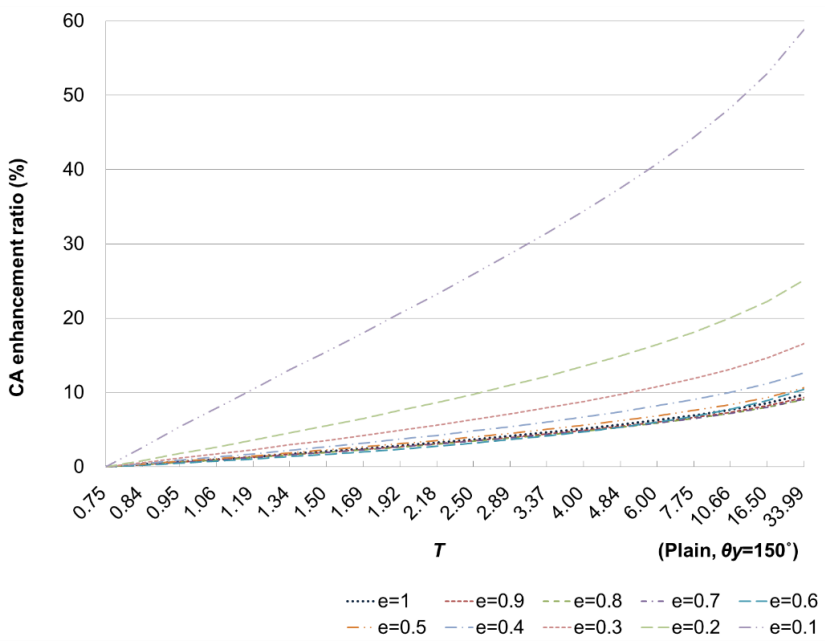
CA enhancement ratio (%)
60
50
40
30
20
10
0
0.75
0.84
0.95
1.06
1.19
1.34
1.50
1.69
1.92
2.18
2.50
2.89
3.37
4.00
4.84
6.00
7.75
10.66
16.50
33.99
T
(Plain, θy=150˚)
e=1
e=0.9
e=0.8
e=0.7
e=0.6
e=0.5
e=0.4
e=0.3
e=0.2
e=0.1

(c)

A. 4.12 Difference of contact angle at varied T in 2/1 twill structure when $e \leq 1$.

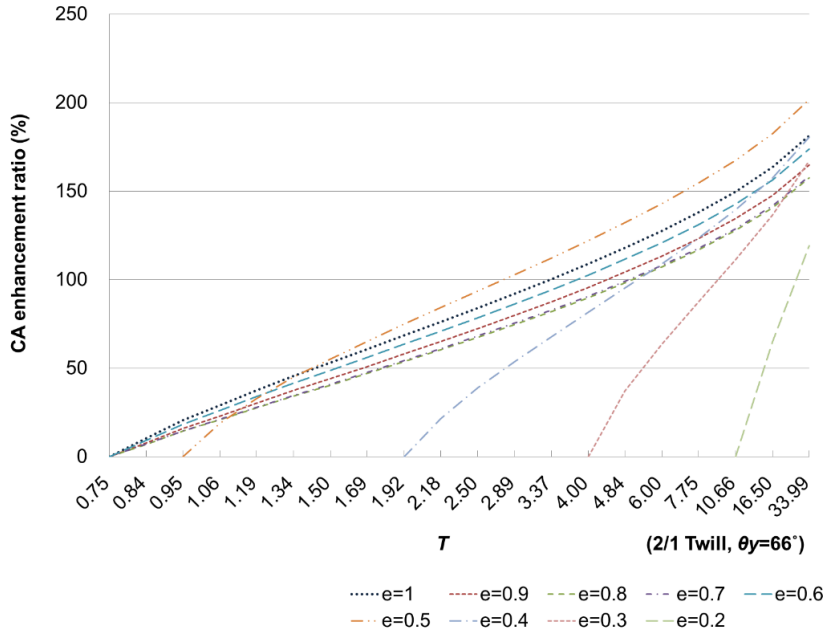
250
200
150
100
50
0
CA enhancement ratio (%)
0.75
0.84
0.95
1.06
1.19
1.34
1.50
1.69
1.92
2.18
2.50
2.89
3.37
4.00
4.84
6.00
7.75
10.66
16.50
33.99
T
(2/1 Twill, θy=66˚)
e=1
e=0.9
e=0.8
e=0.7
e=0.6
e=0.5
e=0.4
e=0.3
e=0.2

(a)

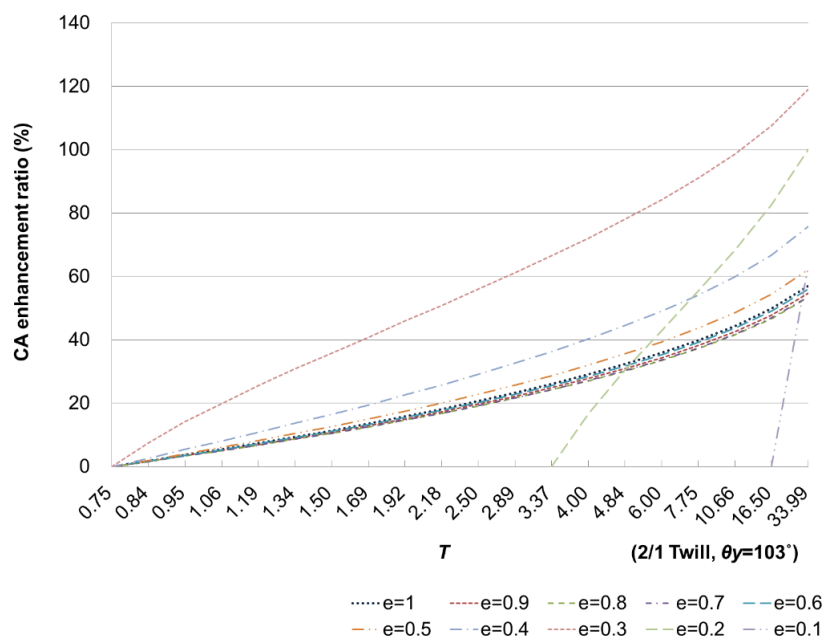
140
120
100
80
60
40
20
0
CA enhancement ratio (%)
0.75
0.84
0.95
1.06
1.19
1.34
1.50
1.69
1.92
2.18
2.50
2.89
3.37
4.00
4.84
6.00
7.75
10.66
16.50
33.99
T
(2/1 Twill, θy=103˚)
e=1
e=0.9
e=0.8
e=0.7
e=0.6
e=0.5
e=0.4
e=0.3
e=0.2
e=0.1

(b)

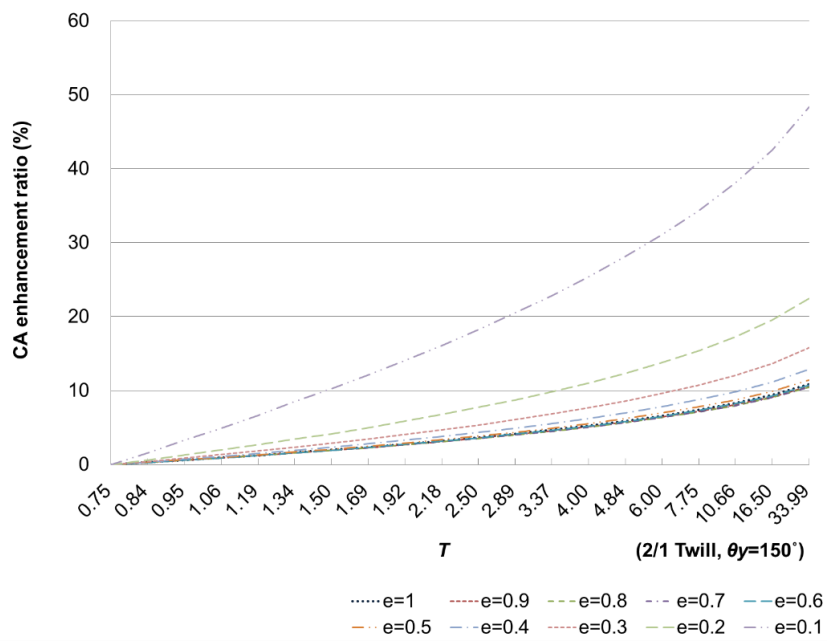
60
50
40
30
20
10
0
CA enhancement ratio (%)
0.75
0.84
0.95
1.06
1.19
1.34
1.50
1.69
1.92
2.18
2.50
2.89
3.37
4.00
4.84
6.00
7.75
10.66
16.50
33.99
T
(2/1 Twill, θy=150˚)
e=1
e=0.9
e=0.8
e=0.7
e=0.6
e=0.5
e=0.4
e=0.3
e=0.2
e=0.1

(c)

A. 4.13 Difference of contact angle at varied T in 2/2 basket structure when $e \leq 1$.

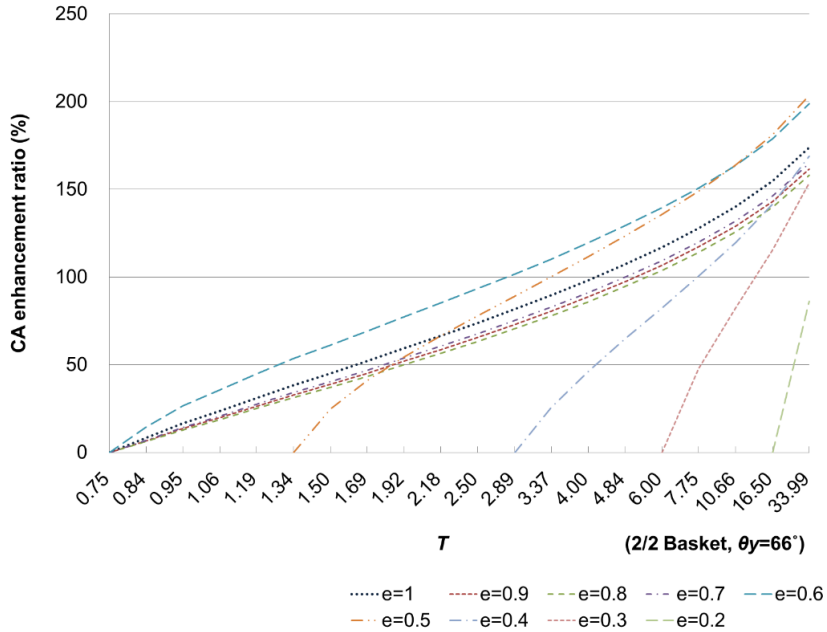
250
200
150
100
50
0
CA enhancement ratio (%)
0.75
0.84
0.95
1.06
1.19
1.34
1.50
1.69
1.92
2.18
2.50
2.89
3.37
4.00
4.84
6.00
7.75
10.66
16.50
33.99
T
(2/2 Basket, θy=66˚)
e=1
e=0.9
e=0.8
e=0.7
e=0.6
e=0.5
e=0.4
e=0.3
e=0.2

(a)

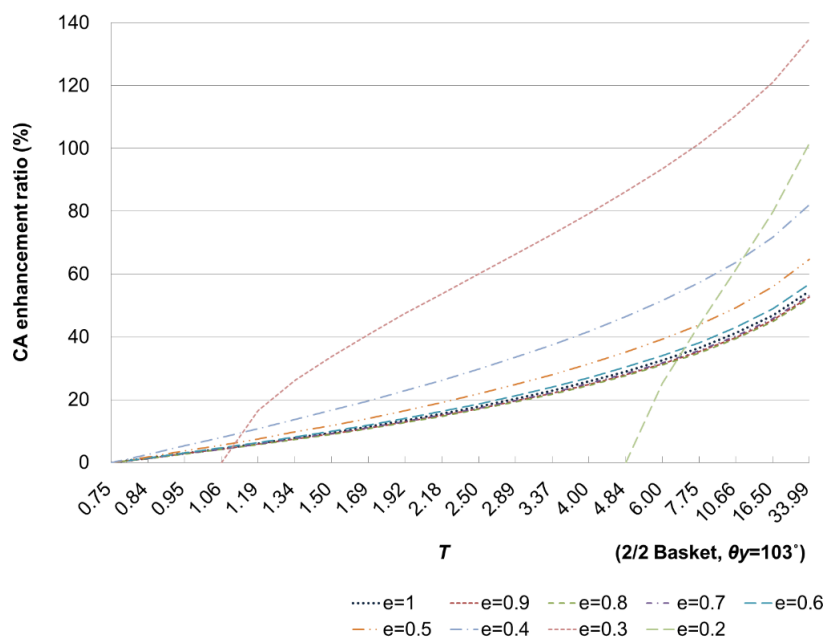
140
120
100
80
60
40
20
0
CA enhancement ratio (%)
0.75
0.84
0.95
1.06
1.19
1.34
1.50
1.69
1.92
2.18
2.50
2.89
3.37
4.00
4.84
6.00
7.75
10.66
16.50
33.99
T
(2/2 Basket, θy=103˚)
e=1
e=0.9
e=0.8
e=0.7
e=0.6
e=0.5
e=0.4
e=0.3
e=0.2

(b)

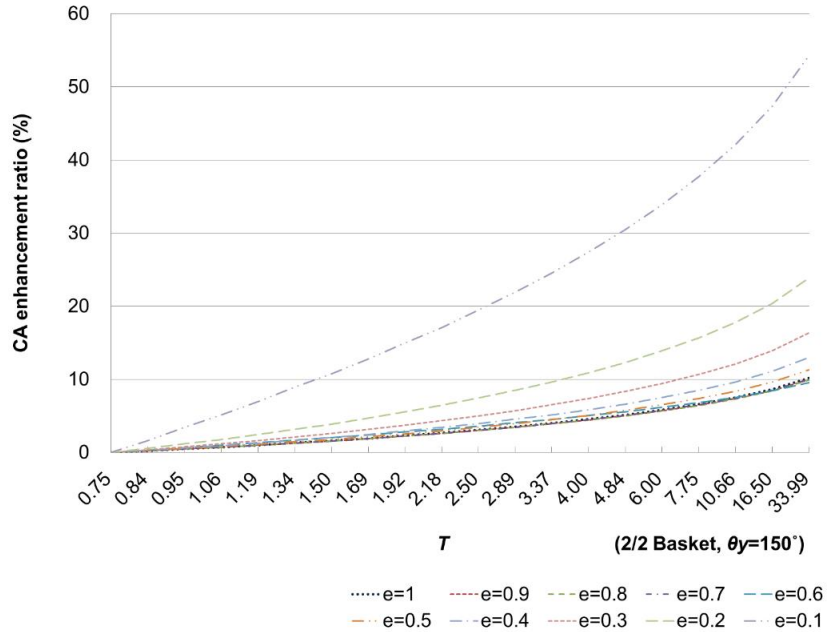
60
50
40
30
20
10
0
CA enhancement ratio (%)
0.75
0.84
0.95
1.06
1.19
1.34
1.50
1.69
1.92
2.18
2.50
2.89
3.37
4.00
4.84
6.00
7.75
10.66
16.50
33.99
T
(2/2 Basket, θy=150˚)
e=1
e=0.9
e=0.8
e=0.7
e=0.6
e=0.5
e=0.4
e=0.3
e=0.2
e=0.1

(c)

A. 4.14. Effect of d_f over R_f on change of contact angle at varied Young's contact angles.

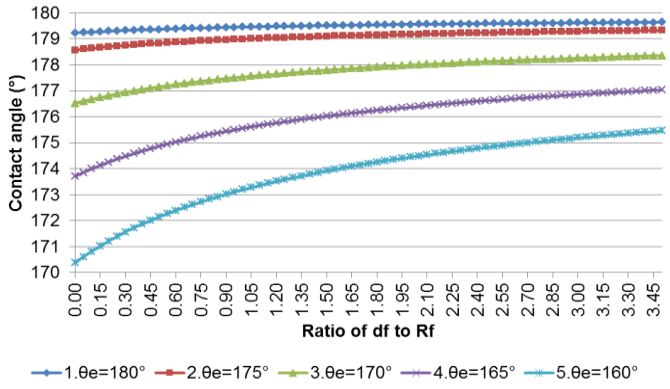
Contact angle (°)
Ratio of df to Rf
1.θe=180°
2.θe=175°
3.θe=170°
4.θe=165°
5.θe=160°

(a)

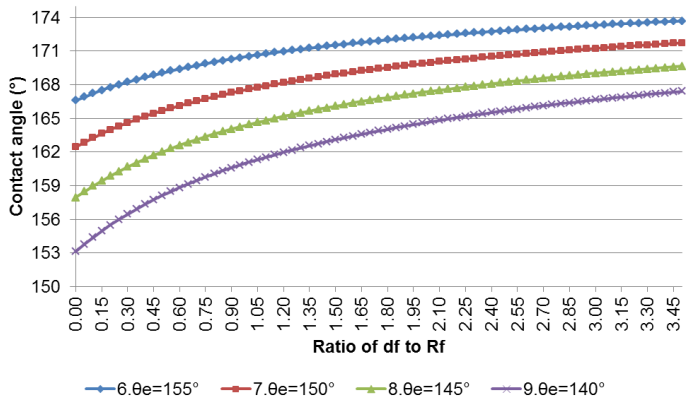
Contact angle (°)
Ratio of df to Rf
6.θe=155°
7.θe=150°
8.θe=145°
9.θe=140°

(b)

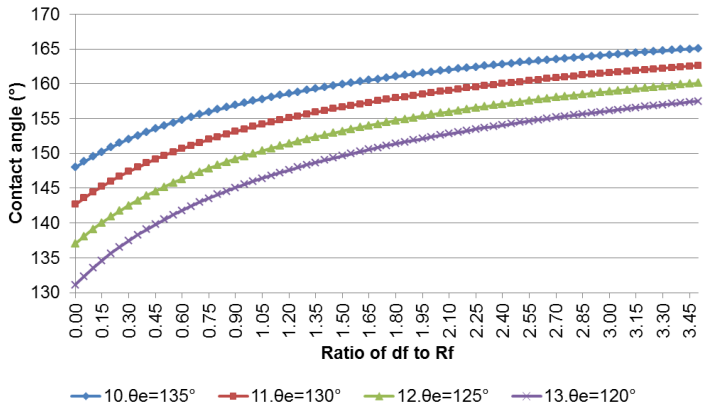
Contact angle (°)
Ratio of df to Rf
10.θe=135°
11.θe=130°
12.θe=125°
13.θe=120°

(c)

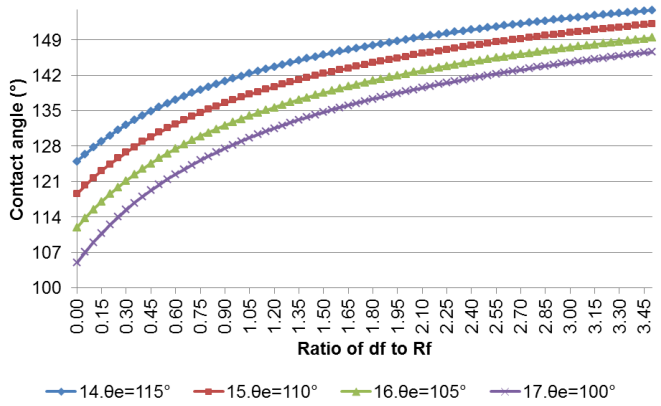
Contact angle (°)
149
142
135
128
121
114
107
100
0.00 0.15 0.30 0.45 0.60 0.75 0.90 1.05 1.20 1.35 1.50 1.65 1.80 1.95 2.10 2.25 2.40 2.55 2.70 2.85 3.00 3.15 3.30 3.45
Ratio of df to Rf
14.θe=115°
15.θe=110°
16.θe=105°
17.θe=100°

(d)

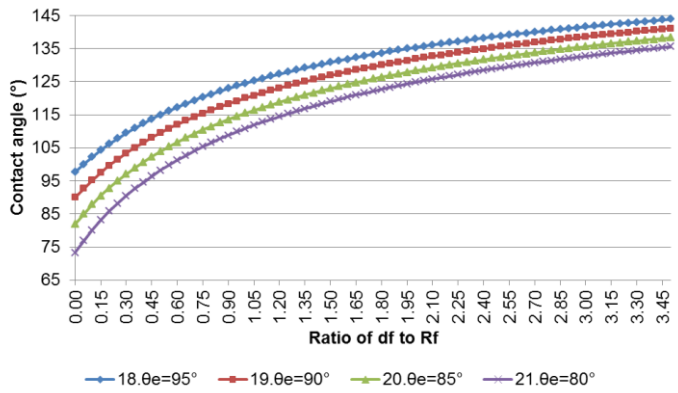
Contact angle (°)
145
135
125
115
105
95
85
75
65
0.00 0.15 0.30 0.45 0.60 0.75 0.90 1.05 1.20 1.35 1.50 1.65 1.80 1.95 2.10 2.25 2.40 2.55 2.70 2.85 3.00 3.15 3.30 3.45
Ratio of df to Rf
18.θe=95°
19.θe=90°
20.θe=85°
21.θe=80°

(e)

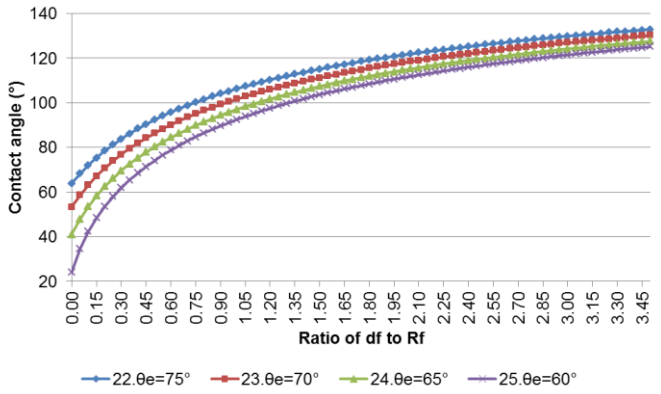
Contact angle (°)
140
120
100
80
60
40
20
0.00 0.15 0.30 0.45 0.60 0.75 0.90 1.05 1.20 1.35 1.50 1.65 1.80 1.95 2.10 2.25 2.40 2.55 2.70 2.85 3.00 3.15 3.30 3.45
Ratio of df to Rf
22.θe=75°
23.θe=70°
24.θe=65°
25.θe=60°

(f)

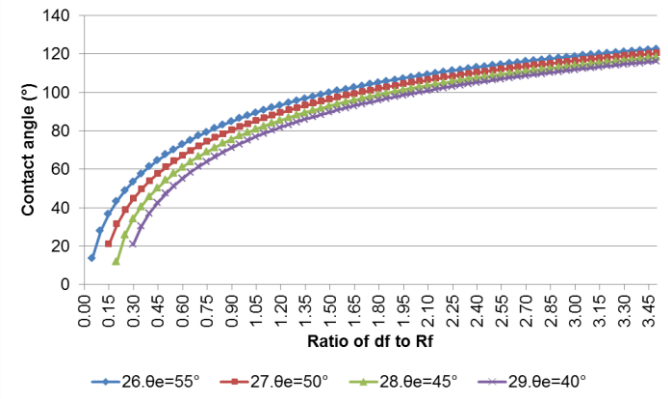
Contact angle (°)
Ratio of df to Rf
26.θe=55°
27.θe=50°
28.θe=45°
29.θe=40°

(g)

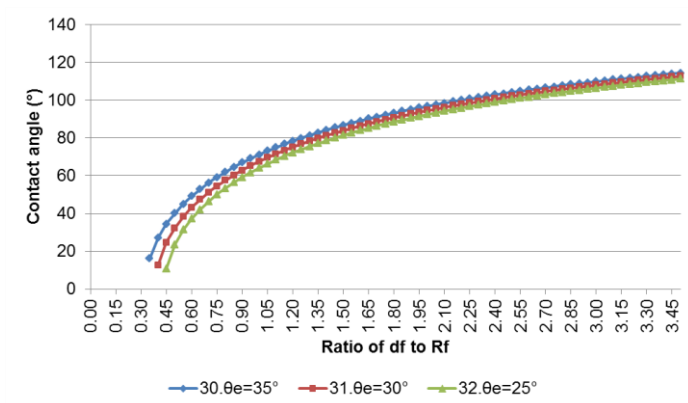
Contact angle (°)
Ratio of df to Rf
30.θe=35°
31.θe=30°
32.θe=25°

(h)

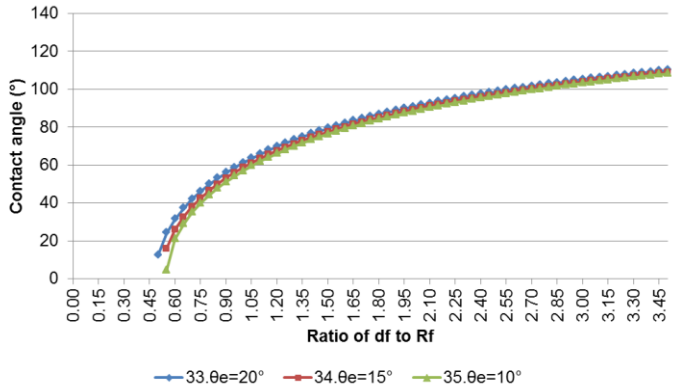
Contact angle (°)
Ratio of df to Rf
33.θe=20°
34.θe=15°
35.θe=10°

(i)

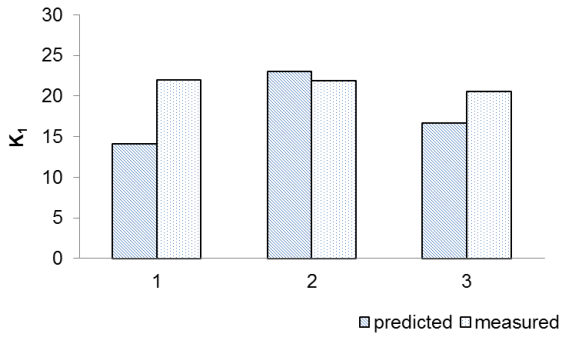

(a)

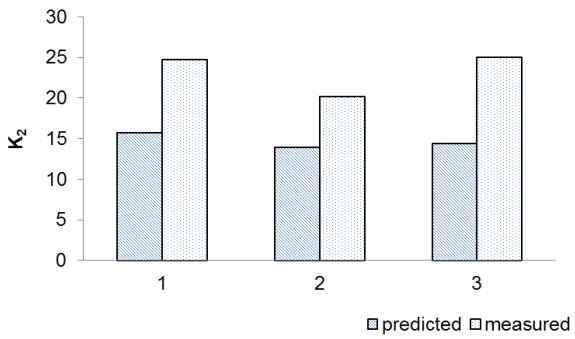

(b)

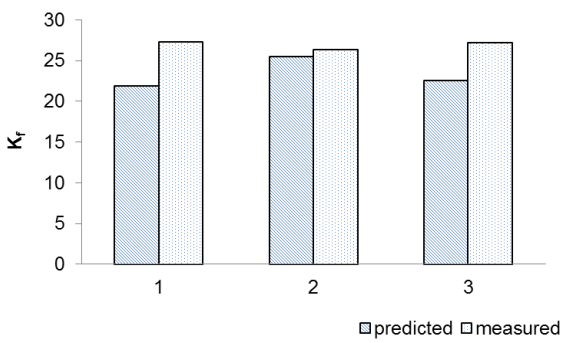

(c)

A. 4.15 Change of cover factor: (a) warp yarn, K_1 (b) weft yarn, K_2, and (c) fabric, K_f.

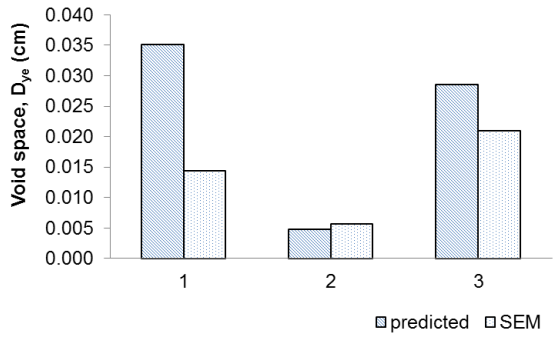

(a)

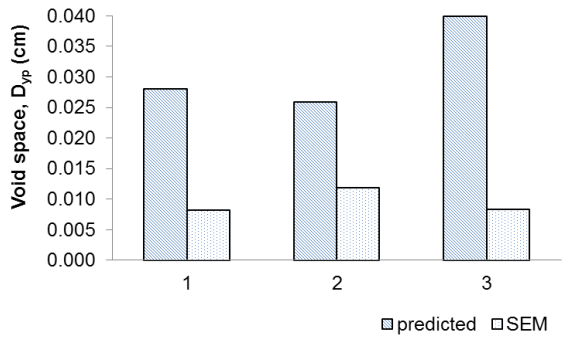

(b)

A. 4.16 Change of void spaces: (a) warp yarn, D_{ye} and (b) weft yarn, D_{yp}.

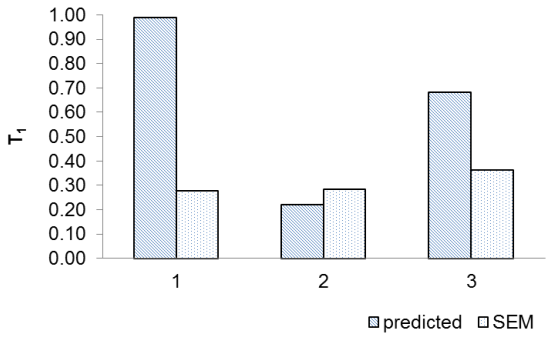

(a)

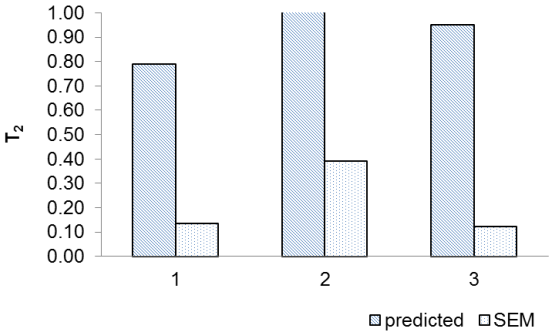

(b)

A. 4.17 Change of void space ratio to yarn diameter: (a) warp yarn, T_1 and (b) weft yarn, T_2.